Missouri S&T Library and Learning Resources

Scholars' Mine

Doctoral Dissertations

Student Theses and Dissertations

Summer 2018

Electrodeposited semiconductor nanostructures & epitaxial thin films for flexible electronics

Naveen Kumar Mahenderkar

Follow this and additional works at: https://scholarsmine.mst.edu/doctoral_dissertations

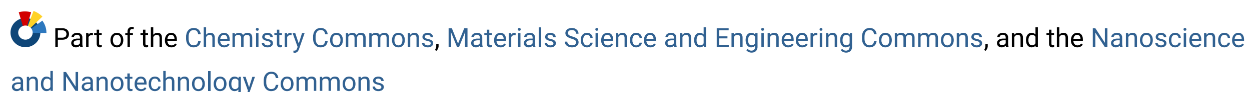
Part of the Chemistry Commons, Materials Science and Engineering Commons, and the Nanoscience and Nanotechnology Commons

Department: Materials Science and Engineering

Recommended Citation

Mahenderkar, Naveen Kumar, "Electrodeposited semiconductor nanostructures & epitaxial thin films for flexible electronics" (2018). *Doctoral Dissertations*. 2706.
https://scholarsmine.mst.edu/doctoral_dissertations/2706

This thesis is brought to you by Scholars' Mine, a service of the Missouri S&T Library and Learning Resources. This work is protected by U. S. Copyright Law. Unauthorized use including reproduction for redistribution requires the permission of the copyright holder. For more information, please contact scholarsmine@mst.edu.

ELECTRODEPOSITED SEMICONDUCTOR NANOSTRUCTURES & EPITAXIAL THIN FILMS FOR FLEXIBLE ELECTRONICS

by

NAVEEN KUMAR MAHENDERKAR

A DISSERTATION

Presented to the Graduate Faculty of the

MISSOURI UNIVERSITY OF SCIENCE AND TECHNOLOGY

In Partial Fulfillment of the Requirements for the Degree

DOCTOR OF PHILOSOPHY

in

MATERIALS SCIENCE AND ENGINEERING

2018

Approved by

Jay A. Switzer, Advisor
Matthew J. O'Keefe
F. Scott Miller
Michael S. Moats
Jeffrey G. Winiarz

© 2018

NAVEEN KUMAR MAHENDERKAR

All Rights Reserved

PUBLICATION DISSERTATION OPTION

This dissertation consists of the following articles that are published in peer-reviewed journals: Paper I: Electrodeposited germanium nanowires, found on pages 27 - 47, is published in *ACS Nano* **2014**, 8 (9), pp. 9524-9530. Paper II: Nanometer-thick gold on silicon as a proxy for single-crystal gold for the electrodeposition of epitaxial cuprous oxide thin films, found on pages 48 - 84, is published in *ACS Applied Materials & Interfaces*, **2016**, 8 (24), pp. 15828-15837. Paper III: Epitaxial lift-off of electrodeposited single-crystal gold foils for flexible electronics, found on pages 85 - 109, is published in *Science*, **2017**, 355 (6330), pp. 1203-1206.

ABSTRACT

Single-crystal Si is the bedrock of semiconductor devices due to the high crystalline perfection which minimizes electron-hole recombination, and the dense native silicon oxide which minimizes surface states. To expand the palette of electronic materials beyond planar Si, an inexpensive source of highly ordered material is needed that can serve as an inert substrate for the epitaxial growth of grain boundary-free semiconductors, photonic materials, and superconductors. There is also a need for a simple, inexpensive, and scalable fabrication technique for the growth of semiconductor nanostructures and thin films. This dissertation focuses on the fabrication of semiconducting nanowires (polycrystalline Ge & epitaxial ZnO) and epitaxial thin films (Au & Cu_2O) using electrodeposition from an aqueous solution at ambient conditions as a simple benchtop process. Paper I describes a simple one-step electrodeposition of Ge nanowires on an indium-tin oxide substrate decorated with In nanoparticles. An In metal acts both as a catalyst for electrodeposition and as a solvent for recrystallization of the nanowires at ambient conditions. Ge nanowires are an attractive anode material for Li-ion batteries, due to their larger theoretical capacity compared to graphite. Paper II presents a scheme for epitaxial electrodeposition of ultrathin Au films on Si as an inexpensive proxy for single crystal Au for the electrodeposition of epitaxial Cu_2O thin films. A detailed study of the epitaxial growth, morphology, junction characteristics, and crystallinity is performed for both the Au and Cu_2O thin films. Paper III describes a technique for epitaxial lift-off of wafer-scale Au foils as transparent, single-crystal and flexible substrates for flexible electronics. The Au foils offer the order of traditional single-crystal semiconductors without the constraint of a rigid substrate. An organic light emitting diode is presented to evaluate the flexibility and transparency of Au foils. To study the single crystal nature of Au foil an epitaxial Cu_2O thin film inorganic diode with an improved diode quality factor is demonstrated.

ACKNOWLEDGMENTS

I would like to express my sincere gratitude to my advisor and mentor Prof. Jay A. Switzer for believing in me and for giving me the opportunities and his continuous support to work on exciting projects throughout my research. His office door was always open whenever I wanted to run through some new ideas or had a question about ongoing research. Our daily informal meetings at the end of the day, catching up on the new results and brainstorming new techniques has always motivated me to work harder. His immense knowledge and guidance has always inspired me to think out of the box and I could not have imagined having a better advisor and mentor for my PhD research. Besides my advisor, I would also like to thank my dissertation committee members: Dr. Matthew J. O'Keefe, Dr. F. Scott Miller, Dr. Michael S. Moats, and Dr. Jeffrey G. Winiarz, for their insightful comments and encouragement.

My sincere thanks also go to Dr. Eric W. Bohannan for his exceptional assistance with X-ray diffraction measurements and analysis, Dr. Clarissa A. Wisner and Dr. Jessica R. TerBush for proving expertise in electron microscopy, and all the technical and administrative staff at the Materials Research Center.

I would also like to thank all my friends and lab mates, especially Dr. Jakub A. Koza, Dr. Ying-Chau (Allen) Liu, Dr. James C. Hill, Meagan Kelso, Qingzhi Chen, Caleb Hull, John Tubbesing, Joel Borcherding, Alex Duchild, and Seth Hofheins for their help and support. I would also like to thank my parents for their constant support and motivation to pursue difficult challenges and to never give up. I owe a large part of my success to them and could not have done it without their love and support.

Finally, I would like to acknowledge Department of Energy, Office of Basic Science (Grant no. DE-FG0208ER46518) for funding my work.

TABLE OF CONTENTS

Page

PUBLICATION DISSERTATION OPTION iii

ABSTRACT iv

ACKNOWLEDGMENTS v

LIST OF ILLUSTRATIONS x

LIST OF TABLES xii

SECTION

1. INTRODUCTION 1

1.1. MATERIALS FOR FLEXIBLE ELECTRONICS 2

1.1.1. Conductive Metal Oxides 2

1.1.2. Conductive Polymers 3

1.1.3. Nanowire Mesh Substrates 3

1.1.4. Ultrathin Metal Foil Substrates 4

1.1.5. Polymer Substrates 4

1.1.6. Paper and Fabric Substrates 5

1.2. AN OVERVIEW OF FABRICATION TECHNIQUES FOR FLEXIBLE ELECTRONICS 6

1.3. ELECTRODEPOSITION OF THIN FILMS & NANOSTRUCTURES 7

1.3.1. Electrodeposition of Epitaxial Thin Films 8

1.3.1.1. Epitaxial Au(111) on n-Si(111) 9

1.3.1.2. Epitaxial Cu_2O(111) on Au/Si(111) 12

1.3.2. Electrodeposition of Nanowires 13

1.3.2.1. Electrodeposition of Ge nanowires 14

1.3.2.2. Electrodeposition of ZnO nanowires 22

1.4. RESEARCH OBJECTIVES 24

1.4.1. Epitaxial Electrodeposition of Au on Si as a Proxy for Single-Crystal Au 24

1.4.2. Epitaxial Lift-off of Electrodeposited Single-Crystal Au Foils 25

1.4.3. Fabrication of $Ru^{II}(bpy)_3$ Based Organic Light Emitting Diode and Epitaxial Cu_2O Inorganic Diode on Au Foil 25

1.4.4. Electrodeposition of Epitaxial ZnO and Polycrystalline Ge Nanowires 25

PAPER

I. ELECTRODEPOSITED GERMANIUM NANOWIRES 27

ABSTRACT 27

1. INTRODUCTION 28

2. RESULTS AND DISCUSSION 29

3. CONCLUSIONS 39

4. MATERIALS AND METHODS 39

SUPPORTING INFORMATION 40

ACKNOWLEDGMENTS 44

REFERENCES 45

II. NANOMETER-THICK GOLD ON SILICON AS A PROXY FOR SINGLE-CRYSTAL GOLD FOR THE ELECTRODEPOSITION OF EPITAXIAL CUPROUS OXIDE THIN FILMS 48

ABSTRACT 48

1. INTRODUCTION 49

2. RESULTS AND DISCUSSION 51

3. CONCLUSIONS 68

4. MATERIALS AND METHODS 69

4.1. Si Wafers and Etching Procedures 69

4.2. Electrodeposition of Au and Cu_2O Films 70

4.3. X-ray Diffraction Measurements and Interface Models 70

4.4. SEM Measurements 71

4.5. TEM Measurements 71

4.6. Measurement of Interfacial Energetics 72

SUPPORTING INFORMATION 72

AUTHOR INFORMATION 80

ACKNOWLEDGEMENTS 80

REFERENCES 81

III. EPITAXIAL LIFT-OFF OF ELECTRODEPOSITED SINGLE-CRYSTAL GOLD FOILS FOR FLEXIBLE ELECTRONICS 85

ABSTRACT 85

1. INTRODUCTION 86

2. RESULTS AND DISCUSSION 87

3. CONCLUSIONS 95

SUPPLEMENTARY MATERIALS 96

ACKNOWLEDGEMENTS 106

REFERENCES 107

SECTION

2. CONCLUSIONS & FUTURE WORK 110

2.1. CONCLUSIONS 110

2.2. FUTURE WORK 112

2.2.1. Spin Coated Epitaxial Perovskite Thin Films on Au Foil 112

2.2.2. Electrodeposition of Epitaxial Ge Nanowires 112

BIBLIOGRAPHY 114

VITA 128

LIST OF ILLUSTRATIONS

Figure Page

SECTION

1.1. Interface model of Au(111) on Si(111) with Moirè pattern resulting from 4 unit meshes of Au coinciding with 3 unit meshes of Si with a coincidence site lattice mismatch of +0.13%. 11

1.2. Interface model of Cu atoms of $Cu_2O(111)$ overlay on Au atoms of Au(111)/ Si(111). 12

1.3. E-pH diagram of (a) Ge-H_2O system at room temperature and 1 atm pressure with most stable domains labeled and (b) Ge-H_2O system at 1 atm pressure for four different temperatures. 17

1.4. Phase diagram of Ge-In system with indication of the composition of liquid alloy catalyst in the course of growth of nanowires. 21

PAPER I

1. Schematic of electrodeposition of Ge nanowires. 30

2. Electrochemical data for Ge nanowire electrodeposition. 31

3. Crystallinity of Ge nanowires. 32

4. Morphology of In nanoparticles and Ge nanowires. 33

5. (a) TEM of a single Ge nanowire deposited at 95 °C with an In nanoparticle at the tip of the wire. 34

6. Optical bandgap measurements of Ge nanowires. 36

7. Raman spectrum of Ge nanowires deposited at 95 °C (red solid line); the blue dashed line corresponds to the first-order Stokes peak for crystalline bulk Ge. 37

PAPER II

1. X-ray diffraction patterns of Au on Si. 52

2. Thickness measurement of Au(111) on Si(111) by X-ray reflectivity, Laue oscillations, and TEM. 53

3. Surface morphology of the epitaxial Au films on Si. 56

4. Junction characteristics of Au on Si(111). 57

5. X-ray diffraction patterns of Cu_2O on Au on Si. 58

6. X-ray rocking curves of Au and Cu_2O on Si measure out-of-plane mosaic spread. 60

7. High-resolution cross-sectional TEM of $Cu_2O(111)$ and Au(111) on Si(111). 61

8. In-plane orientation of Au and Cu_2O on Si from X-ray pole figures. 62

9. Interface models of Au on Si. 65

10. Evidence for out-of-plane tensile strain in ultrathin Au(111) films on Si(111). 67

PAPER III

1. Schematic for epitaxial lift-off of single-crystal Au foil. 87

2. Electron microscopy of the single-crystal Au, epitaxial Cu_2O, and epitaxial ZnO. 89

3. X-ray diffraction and pole figures to study the in-plane and out-of-plane orientation. 92

4. Transmittance, sheet resistance, and flexibility of Au foils with diode and OLED fabrication. 94

LIST OF TABLES

Table Page

SECTION

1.1. Species of Ge in equilibrium at various temperatures and their corresponding calculated E-pH equations 19

1.2. Various solid and ionic species of Ge which were not considered in the construction of the Pourbaix diagrams. 20

SECTION

1. INTRODUCTION

The development of flexible electronic devices is evident from the evolution of conventional rigid architectures to foldable, bendable and stretchable devices.[1,2] These devices cater to a wide range of applications including continuous health monitoring, curved displays, sensors, solar cells, batteries, and biomedical implants.[3–5] Flexible electronic devices need to be capable of undergoing deformation while maintaining the functional and electronic properties. The high strain due to bending, twisting and stretching cannot be achieved using traditional brittle materials such as Si and glass. Thus, innovation in flexible electronics requires new fabrication techniques, materials and design choices. Conventional inorganic materials may be implemented in flexible electronics with changes in the morphology (nanowire or nanoparticle) or thickness to withstand the high strain during operation. Along with conventional inorganic materials, organic semiconductors are a fast-growing field of research for flexible electronics due to their inherent high strain tolerance and low-temperature processing.[6] Organic semiconductors for displays[7] and energy generation[8] show improved efficiencies compared to inorganic semiconductors while maintaining simple and environmentally friendly processing techniques.[9] Some of the critical parameters for a robust and durable flexible device are material choice for substrate and active component, material design, type of fabrication process and field of application.

Current research on flexible electronic devices use vapor depositions of indium tin-oxide,[10] ultrathin metal films,[11] spin-coated nanowire mesh[12] or conductive polymers[13] on flexible plastic substrates, which tend to be polycrystalline or textured. Thus, the semiconductors grown on top of the substrate also have a random orientation. Polycrystalline

electronic materials suffer from electron hole-recombination at the grain boundaries, which act as defect sites yielding lower efficiencies.[14] Therefore, there is a need for an inexpensive, simple and large-scale fabrication technique, while maintaining the critical parameters to control the morphology and crystallinity. The aim of this research is to fabricate semiconductor nanostructures (polycrystalline Ge & epitaxial ZnO nanowires) and epitaxial thin films (Au & Cu_2O) using a simple benchtop aqueous electrodeposition process at ambient conditions. This study focuses on both the polycrystalline and the epitaxial growth of semiconductors. For instance, Ge nanowires electrodeposited on an indium-tin oxide substrate tend to grow polycrystalline and highly doped.[15] However, the high conductivity of the nanowires makes them ideal for Li-ion battery applications. This research also focuses on the epitaxial growth of Au on n-Si substrate that forms a Schottky junction[16] and exhibits metal-semiconductor characteristics useful for photoelectrochemical applications.[17] The ultrathin epitaxial films of Au on n-Si are also used for the epitaxial lift-off of free-standing and single-crystal foil substrates for flexible electronics.[18]

1.1. MATERIALS FOR FLEXIBLE ELECTRONICS

The materials for flexible electronic devices include conductive thin films for contacts,[19] semiconductors,[20] and high-κ dielectric insulators.[19–20] Some of the frequently used conducive materials for contacts include transparent conducting oxides,[20] conductive polymers,[13] polymers with conductive filler,[21] nanowire[12,22] or carbon nanotube[23] mesh electrodes, and ultrathin metal foils.[24–25] The contacts are usually deposited on a non-conductive and flexible support materials such as plastics, paper and fabrics.

1.1.1. Conductive Metal Oxides. Transparent conductive metal oxides are usually used as contacts for devices such as solar cells and light emitting diodes which require light transmission.[10,26–27] Indium-tin oxide, antimony doped tin oxide, and aluminum doped zinc

oxide are some of the typically used transparent conducting oxides. They offer relatively high optical transmission (>95%) in the spectral range of visible and near infrared light, intended for applications in displays and solar cells. However, these metal oxides are typically polycrystalline and brittle for high strain applications.

1.1.2. Conductive Polymers. Conjugated polymers and elastomers with conductive filler are also used in flexible electronic applications.[28–30] Polyaniline, polypyrrole, polythiophene, and poly(3,4-ethylenedioxythiophene):poly(styrenesulfonate) (PEDOT:PSS) are some of the most studied conductive polymers.[26,31–32] They are typically spin coated from aqueous or non-aqueous solvents and heat treated at a relatively low temperature (ca. 100 °C). Due to the simple solution processing, large scale manufacturing using this method can be considered. Some of the drawbacks of conductive polymers are low electrical conductivity compared to metal foils or transparent conducting oxides, and poor crystallinity. Another type of conductive polymer uses a non-conducting elastomer matrix with a conductive filler material.[21,31,33–34] The filler material is usually metal nanoparticles, nanowires, or carbon nanotubes dispersed in the matrix forming an interconnected network allowing for electrical conductivity. The conductivity is largely dependent on the dispersion, volume fraction, shape, size, and alignment of the filler material. Like conjugated conductive polymers, elastomers with filler also show low conductivities and poor crystallinity for epitaxial growth.

1.1.3. Nanowire Mesh Substrates. Conductive nanowire mesh is another widely used alternative to transparent conductive oxides as they provide comparable transmission in the visible and near infrared spectrum, while enabling high strain-tolerance.[35–36] These percolated networks typically consist of high-aspect-ratio metal or metal oxide nanowires spin coated to form an aligned or random distribution.[22] The intersection of metal nanowires in the network enables charge transport along the surface of the thin film. The large pore

volume fraction in the nanowire mesh allows high optical transmission and improves mechanical displacement during flexing. Gold nanowires,[36] silver nanowires,[22,37] carbon nanotubes,[38] and copper nanowires[39] are some of the commonly used conductive materials for the mesh films. The nanowire mesh also does not offer a highly ordered substrate for the epitaxial growth of semiconductors.

1.1.4. Ultrathin Metal Foil Substrates. Metal foils offer high electrical conductivity, crystallinity, and can also withstand relatively high processing temperatures.[11,24–25,40] They also offer an improved barrier against diffusion of air or moisture. In addition to mechanical and electronic properties, ultrathin metal foils (7-30 nm) also offer high optical transparency, which can be considered as an alternative to transparent conductive oxides. However, metal films are typically evaporated or sputtered on glass or plastic substrates which results in a polycrystalline structure.

1.1.5. Polymer Substrates. Choice of material for a substrate largely depends on the application of the device. However, some of the common properties desired for any type of device are flexibility, low cost, light weight and suitability for high volume manufacturing. Currently, the most common flexible substrate that has all the features mentioned above are plastics.[24,26,31,41] Some of the key types of plastics used include polyethylene terephthalate, polycarbonate, polyimide, polyethersulfone, and polyacrylate. For applications that demand stretchability, elastomers such as polydimethylsiloxane and polyurethane are preferred.[26,31] Polymers also offer high optical clarity and surface smoothness that are especially beneficial for applications that include solar cells, optical sensors and displays. Although polymers offer a lot of material properties suitable for flexible applications, they lack thermal stability, solvent resistance and, more importantly, crystallinity. Due to the amorphous polymer substrates, the semiconductors tend to be amorphous or polycrystalline. This can result in

low overall efficiency for the device mainly due to the electron hole recombination at the grain boundaries.

1.1.6. Paper and Fabric Substrates. The next class of materials for flexible substrates are paper and fabrics. Paper electronics are on the rise due to their high flexibility, low cost, high recyclability, and the ability to fabricate printed electronics.[32,42–43] However, they lack mechanical stability during solvent processing due to absorption, and high surface roughness due to the fibrous morphology. Nevertheless, there has been promising research using cellulose paper as an active substrate material for sensors and actuators referred to as smart paper.[42] Printing of conductive inks based on metal precursors, nanoparticles, or nanowires has enabled fast, room temperature circuit designs on paper. This fabrication process also opened a whole new field of printed electronics on flexible substrates. Similarly, using organic semiconductor precursor inks, printed photovoltaic devices and field-effect transistors are also being actively researched.[42] One of the ambitious futuristic visions of flexible electronics is the integration of smart devices with clothing, also referred to as smart textiles.[43–46] Smart fabrics can be used as a flexible antenna for data communication,[45] light harvesting for energy generation or for continuous health monitoring devices.[46] However, the challenges of having a flexible woven fabric of active material which can withstand moisture, dust, and high strain conditions are still difficult to overcome.[47] Even with the advances in research to incorporate papers and fabrics into electronics, they all lack crystalline order which could lower the overall efficiency of the device.

1.2. AN OVERVIEW OF FABRICATION TECHNIQUES FOR FLEXIBLE ELECTRONICS

Materials for flexible or stretchable electronic devices can be fabricated using a wide array of techniques. However, the methods used for deposition of the active materials are largely dependant on the processing conditions compatible with plastic, paper or fabric substrates. Some of the most commonly used techniques for deposition of metals, metal oxides and inorganic materials include physical vapor deposition (sputtering and evaporation),[48] chemical vapor deposition,[48–49] atomic layer deposition,[50–51] electrodeposition,[52] and roll-to-roll deposition.[53–56] Sputtering or evaporation can be used in conjunction with lithography or shadow masks to produce metal patterns for the contact electrodes on devices.[48] Chemical vapor and atomic layer depositions are typically used for growing semiconductor or insulator nanostructures/thin films.[48,50] Although, roll-to-roll deposition with physical and chemical vapor deposition compatibility is especially attractive for large scale manufacturing,[57–61] the high temperatures associated with the chemical reactions make it challenging on plastic substrates.

Some of the methods used for the processing of organic and hybrid flexible electronic materials are spin coating,[62] dip coating,[63] screen printing,[56] spray coating,[64–65] and transfer printing.[66–68] These techniques are also suitable for high volume manufacturing. However, they are highly dependant on the suitable solvent used for the dissolution/dispersion of each material. Semiconductors that are deposited using the sol-gel[69] technique require additional thermal annealing steps which could also limit the use of plastic substrates. The printing techniques for large scale rapid manufacturing can be divided into two types: transfer printing and digital printing. The transfer printing process consists of a pre-patterned mold, typically made of a flexible polydimethylsiloxane stamp.[70] The pattern with protruding features is used to transfer semiconducting or metallic inks onto a desired flexible substrate. This process is also referred to as contact printing or contact lithography. The stamped

patterns are then annealed at a relatively low temperature (ca. 100°C) to cure the ink.[70] Digital printing on the other hand does not require any patterned stamps, as it is similar to conventional paper printing.[71–72] A computerized digital design is used to direct a nozzle with the ink to print directly on the substrate. This process is also referred to as inkjet printing,[71–72] laser printing[73–74] or direct ink[75–76] writing. In laser printing, the substrate is selectively heated using a laser to enable fast curing of the ink. Due to the precise control of the ink flow, this technique tends to be highly adaptive and reproducible.

The methods described above for the fabrication of organic and inorganic materials for flexible electronics enable a wide range of possibilities. However, all the materials are typically deposited directly onto an amorphous plastic substrate, which yields an amorphous or polycrystalline semiconductor. The presence of grain boundaries acts as a defect site for electron-hole recombination, lowering the overall efficiency of the device.[14] To facilitate the growth of epitaxial nanowires and thin films, electrodeposition can be used as an inexpensive and scalable process for the fabrication of highly ordered metallic foil substrates.[18]

1.3. ELECTRODEPOSITION OF THIN FILMS & NANOSTRUCTURES

Electrodeposition offers an inexpensive and simple alternative for the growth of thin films and nanostructures at ambient temperature and pressure. Traditionally used methods for thin film deposition, such as, chemical or physical vapor deposition,[48–49] hydrothermal synthesis,[77] molecular beam epitaxy,[78] and pulsed laser deposition[79] are energy intensive processes. In electrodepositon, precise control of the potential or the current on a conductive substrate in a solution allows for electrochemical oxidation or reduction of chemical species. The electrochemical reactions consist of reduction occurring at the cathode surface, where the metal ions receive electrons and are reduced to form the desired metallic film. The opposite reactions occur at the anode, where the ions lose an electron and are oxidized. By

adjusting the composition,[80–81] pH,[82–84] temperature,[85] potential,[82] current density,[86] and concentration,[87] the final film characteristics such as morphology,[82,88] and crystallography[83] can be controlled. Some of the common substrates used for electrodeposition include metals (Au, Ag, Cu, Ni, Pt, and stainless steel), metal oxides (ITO, FTO, $SrTiO_3$, Cu_2O, and ZnO), semiconductors (Si, InP, GaAs, GaSb, and InAs), and glassy carbon. Unlike metal electrodeposition, where the cation receives electrons corresponding to its oxidation state to directly deposit as a metal film, metal oxides follow an electrochemical-chemical mechanism.[89–90] Here, the first electrochemical step involves oxidation or reduction of an electrochemically active species which can then be chemically reacted to form a desired oxide film on the substrate.[89–90]

1.3.1. Electrodeposition of Epitaxial Thin Films. Epitaxy refers to the growth of a crystalline overlayer on a crystalline substrate, where the substrate controls the orientation of the deposited material. The word *epitaxy* comes from greek roots *epi* meaning "above" and *taxis* meaning "an ordered manner." Typically, single-crystal substrates are used for epitaxial deposition of films. A properly cleaned and treated surface of a single-crystal material presents a highly ordered atomic arrangement and well defined crystallographic orientation. The epitaxial growth of films on the substrate is mainly controlled by the lattice mismatch and the binding energy between the substrate and the film. Epitaxy can further be classified into two categories: homoepitaxy and heteroepitaxy. Homoepitaxy refers to the epitaxial growth of a material on a single-crystal substrate of the same material, for example, growth of Au films on a single-crystal Au substrate. In principle, the same lattice parameter of the material offers no mismatch (assuming no surface reconstruction) and the epitaxy is achieved more easily. Heteroepitaxy on the other hand refers to the epitaxial growth of a material on a substrate of a different material, for example, the epitaxial growth of Au(111) on a Si(111) substrate. Due to the difference in lattice parameter, the lattice mismatch and surface interaction play a crucial role. In this overview of epitaxial thin films,

two examples that include the epitaxial Au(111) on Si(111) and epitaxial Cu_2O(111) on Au/Si(111) will be discussed in detail.

1.3.1.1. Epitaxial Au(111) on n-Si(111). Heteroepitaxial Au(111) on n-Si(111) can be electrodeposited directly from an aqueous solution using a procedure developed by Allongue and co-workers.[91–92] Silicon has the tendency to form a thin, dense, and passivating native oxide on the surface upon exposure to air or aqueous solutions. Therefore, the Si surface is hydrogen-terminated prior to the deposition. In this research, the Si wafers are prepared using the following procedure.[16,18] The wafers prior to use are etched in 5% hydrofluoric acid solution for 30 s to dissolve the native oxide, then they are soaked in hot deionized water (ca. 80-90 °C) for 15 min to passivate the surface with an SiO_x layer. The wafers are then etched again with 5% hydrofluoric acid for 30 s and buffered hydrofluoric acid for 30 s to produce a hydrogen-terminated surface. Ethanol is used to clean any organic residue, and the sample is then rinsed with deionized water prior to deposition. The depositions are performed immediately after the etching process to avoid any surface passivation. n-Si wafers with low doping densities require an ohmic contact to allow electrons to flow through the metal-semiconductor junction. This is achieved by applying a low work-function metal contact such as an indium-gallium eutectic or a sputtered Al thin film. The indium-gallium film is applied using a diamond scribe and heating with a soldering iron to facilitate diffusion of the eutectic into the Si surface. Electrical contact is made by attaching an Ag wire to the back of the Si substrate using a Ag paste and the back of the substrate is insulated by painted nail polish, silicone or Apiezon W wax.

Au is electrodeposited from a solution containing 0.1 mM $HAuCl_4$, 1 mM KCl, 1 mM H_2SO_4, and 100 mM K_2SO_4 in deionized water to produce a final solution with a pH of 3. A -1.9 V vs. Ag/AgCl prepolarized potential is applied to the Si substrate at ambient conditions before the immersion of the electrode. The deposition is performed in a

three-electrode setup with a Ag/AgCl reference electrode, an Au coil as a counter electrode and the etched Si substrate as the working electrode. The requisite step during deposition is the prepolarization of the Si electrode to avoid native oxide formation and to prevent deposition of Au on Si by galvanic displacement.[16,93]

Materials deposited on a polycrystalline substrate exhibit random orientation of grains, which would show an x-ray 2θ pattern that resembles a power sample. In the case of a textured substrate (e.g., sputtered Au on glass), the deposited material might exhibit an out-of-plane oriented 2θ pattern and would show a ring pattern in x-ray pole figures. An epitaxial film shows a single out-of-plane (2θ) and in-plane (pole figures) orientation. The experimental characterization of epitaxy using x-rays is explained in detail in Paper II. One of the most critical parameters for epitaxial growth is the lattice mismatch between the substrate and the film. The true lattice mismatch can be calculated from the unit cell lattice parameters of Au and Si using equation 1.1.

$$\frac{(a_{film} - a_{substrate})}{a_{substrate}} \times 100\% \tag{1.1}$$

where, a_{film} is the lattice spacing of the epitaxial Au film and $a_{substrate}$ is the lattice spacing of Si substrate. Au with a lattice parameter of 0.40786 nm and fcc space group $Fm\bar{3}m$ is deposited onto Si with a lattice parameter of 0.54309 nm and diamond cubic space group $Fd\bar{3}m$. The true lattice mismatch between Au and Si is -24.9%.

$$\frac{(0.40786 - 0.54309)}{0.54309} \times 100\% = -24.9\%$$

The -24.9% mismatch in the Au/Si system is too large to produce epitaxial growth in a simple 1x1 system.[16] The epitaxy can be explained by the formation of coincidence site lattice (CSL) system, where 4 unit meshes of Au coincide with 3 unit meshes of Si.[16] Figure 1.1 shows an interface model of Au(111) atoms on Si(111) atoms. From the top view

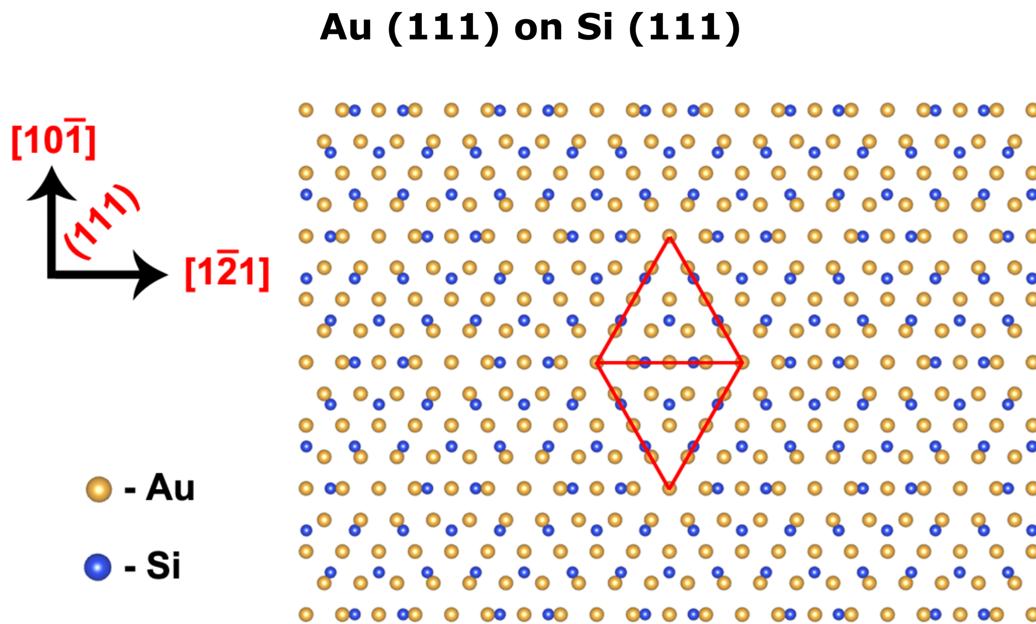

Figure 1.1. Interface model of Au(111) on Si(111) with Moirè pattern resulting from 4 unit meshes of Au coinciding with 3 unit meshes of Si with a coincidence site lattice mismatch of +0.13%.

looking down on the Au atoms (gold colored) sitting on top of Si atoms (blue colored), a repeating pattern (Moirè pattern) can be observed. The lattice mismatch for the CSL can be calculated using the equation 1.1 and replacing the lattice parameters (a) with the d-spacings of Au (0.2884 nm) and Si (0.3840 nm) atoms that coincide in the interface model. The lattice mismatch for the CSL is reduced from -24.9% for the 1d$_{Au(hkl)}$ x 1d$_{Si(hkl)}$ lattice to +0.13% for the 4d$_{Au(hkl)}$ x 3d$_{Si(hkl)}$ CSL. Due to the lattice mismatch, the Au CSL film shows a small compressive in-plane and tensile out-of-plane strain.

$$\frac{(4 \times 0.2884 - 3 \times 0.3840)}{3 \times 0.3840} \times 100\% = +0.13\%$$

Because both Au and Si have cubic structures and Au grows with the same out-of-plane orientation as Si (see Paper II), the lattice mismatch is independent of the orientation of the substrate.

1.3.1.2. Epitaxial Cu_2O(111) on Au/Si(111). Epitaxial Au films on a Si substrate can be electrodeposited to serve as a proxy for single crystal Au substrate.[16] In this work, epitaxial Cu_2O is electrochemically grown on the Au/Si system to study the orientation of epitaxial growth and the effect of grain boundaries on the diode characteristics (see Paper III). Cu_2O is electrodeposited from a solution containing 0.2 M $CuSO_4$, 0.2 M $C_4H_6O_6$ (tartaric acid), and 3.0 M NaOH. The deposition is performed by applying a cathodic current density of 1.0 mA cm^{-2} for 100 s at a temperature of 30 °C.

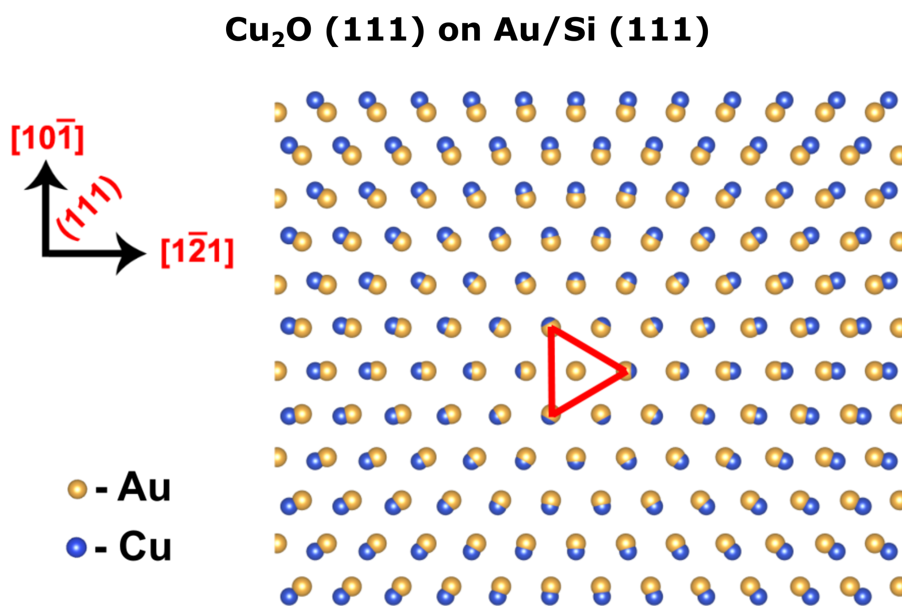

Figure 1.2. Interface model of Cu atoms of Cu_2O(111) overlay on Au atoms of Au(111)/Si(111). A lattice mismatch of +4.7% is observed for 1x1 unit mesh of Cu_2O on Au.

In this epitaxial system, Cu_2O with a lattice parameter of 0.42696 nm and primitive space group $Pn\bar{3}m$ is electrodeposited onto Au/Si substrate. Using the equation 1.1, the true lattice mismatch can be calculated from the unit cell lattice parameters.

$$\frac{(a_{Cu_2O} - a_{Au})}{a_{Au}} \times 100\%$$

$$\frac{(0.42696 - 0.40786)}{0.40786} \times 100\% = +4.7\%$$

where, a_{Cu_2O} is the lattice parameter of Cu_2O film and a_{Au} is the lattice parameter of Au substrate. Figure 1.2 shows the interface models of Cu atoms of Cu_2O (blue colored) overlay on Au atoms (gold colored) for $Cu_2O(111)$/Au(111) orientation. The +4.7% lattice mismatch is reasonably low and is expected to produce a Cu_2O layer with moderate compressive in-plane strain and tensile out-of-plane strain.

1.3.2. Electrodeposition of Nanowires. Nanowires are one-dimensional nanostructures that offer opportunities to control the electronic and optical properties of materials due to their unique morphology.[94–96] They are considered as the building block for next generation electronics,[94] sensors,[97] photonics,[98–99] and energy materials.[37,100] Typically, nanowires exhibit high surface area and high aspect ratios of 1000 or more and demonstrate quantum confinement effects in the lateral direction and thus showing electrical and optical properties different from their traditional bulk counterparts.[101] There is extensive ongoing research on the fabrication of metallic (Au, Cu, Ni, etc.),[102] semiconducting (Si, GaAs, InAs, InP, etc.)[103] and insulating (SiO_2, TiO_2, etc.)[104–106] nanowires.

In a broad sense, there are two basic approaches for the fabrication of nanowires: bottom-up and top-down.[107] The top-down approach uses a bulk material that is etched (lithography or electropolishing) or mechanically polished to modify the size and mor-

phology. The bottom-up technique on the other hand consists of deposition of materials in a nanoporous membrane (polycarbonate[108] or anodized aluminum[109]) or nanoparticle catalytic growth (Si nanowires with a Au catalyst)[110] on a substrate. Several common lab techniques include electrochemical deposition,[108] chemical vapor deposition,[111] and catalytic growth (vapor-liquid-solid process).[110–111] Among these methods, electrodeposition offers an inexpensive, scalable and simple benchtop process for the growth of the nanowires. The following subsections introduce electrodeposition of Ge nanowires using an In catalyst and electrodeposition of ZnO nanowires.

1.3.2.1. Electrodeposition of Ge nanowires. Length scale and dimensionality affect the properties of materials in ways that are often unforeseen based on bulk properties.[112] One-dimensional Ge nanowires have attracted great interest due to their remarkable electrical and optical properties.[113–115] Ge is an important semiconductor with a direct bandgap of 0.8 eV and an indirect bandgap of 0.66 eV.[116] Nanostructures of Ge are an attractive anode material in Li-ion batteries due to higher charge-discharge capacity (600 - 1140 $mAh.g^{-1}$) compared to the currently used graphite (370 $mAh.g^{-1}$) and higher room temperature diffusivity of Li in Ge enables its use in high-power-rate applications.[15] Ge is also being considered as a replacement for Si as an active channel material for CMOS transistors.[117–119] Traditionally, Ge nanowires are deposited using energy intensive processes such as laser ablation,[120] chemical vapor deposition,[121] thermal evaporation,[122] and supercritical fluid-liquid-solid synthesis.[123] Electrodeposition of Ge in an aqueous system is thermodynamically hindered due to the competing hydrogen evolution reaction and the growth usually is restricted to a few monolayers.[124–127] Therefore, most of the studies on electrodeposition of Ge have been done using non-aqueous solutions.[128]

Recently, pioneering work on electrodeposition of Ge and Si nanowires from an aqueous solution at ambient conditions has been shown by Maldonado and co-workers.[129–136] The process utilizes various metallic liquids such as Hg, Ga, Bi-In, and In-Ga eutectic, which acts both as an electrode for electrodeposition and as a solvent for recrystallization using an electrochemical liquid-liquid-solid (ec-LLS) process. Direct electrodeposition of Si nanowires,[136] nanostructured Ge filaments on liquid Hg,[132] and epitaxial Ge nanowires on Ga nanodroplets[134] have been demonstrated. Although, electrodeposition of Ge nanowires on liquid metallic catalyst nanoparticles is shown, the process typically consists of individual steps for deposition of catalyst nanoparticles on the substrate followed by electrodeposition of Ge nanowires from a different solution. In this work, a simple one-step method using the ec-LLS process to grow dense Ge nanowire array from one solution directly on an indium-tin oxide substrate is shown.[15] The Ge nanowires tend to grow with a random orientation due to the polycrystalline nature of the indium-tin oxide substrate. The nanowires are also highly doped due the presence on In impurities during the growth process. Although, the polycrystalline nature and high electrical conductivity of the nanowires are not suitable for CMOS transistors, they should be ideal for Li-ion battery applications.[130]

Ge electrodeposition is performed on an indium-tin oxide substrate from a solution containing 50 mM GeO_2, 0.5 M Na_2SO_4 as supporting electrolyte and 0.1 M succinic acid, $C_4H_6O_4$ as a complexing agent, with the pH adjusted to about 6.5 using NaOH.[15] It is observed that upon the application of a constant current density at the cathode, the indium-tin oxide substrate is electrochemically reduced to In metal nanoparticles. The bulk melting temperature of In is 156 °C, however, a melting point depression causes the In nanoparticles to behave similar to nanodroplets of In metal. The In nanoparticles act both as a reduction site for dissolved Ge(IV) species and as a solvent for crystallization of the

nanowires.[15,134–135] A scheme explaining the electrochemical reduction of indium-tin oxide and growth of Ge nanowires is explained in detail in Paper I.

At this point, it is instructive to review the thermodynamics of Ge nanowire growth on an In nanoparticle using Pourbaix diagrams. Potential-pH diagrams, called Pourbaix diagrams, represent thermodynamic and electrochemical equilibria in aqueous solutions.[137] A Pourbaix diagram plots the equilibrium potential (E_e) between a metal/semimetal and its various oxidized species as a function of pH. Pourbaix diagrams are useful in electrodeposition applications and other fields such as corrosion electrochemistry, geology, and energy conversion.[138] Most of the diagrams are constructed at room temperature and thus the utility is limited in terms of application for high temperature. To construct Pourbaix diagrams at elevated temperatures, thermodynamic data are needed at high temperatures.

The Pourbaix diagrams are constructed using the potential-pH equations for various stable domains of Ge-H_2O system at 298 K, 325 K, 350 K and 375 K. The species participating in the various electrochemical equilibria are the solids H_2GeO_3, and Ge, the ion $HGeO_3^-$ and the gas GeH_4. The pertinent standard room temperature Gibbs free energy of the formation data are taken from Pourbaix.[139] To determine the relationship between thermodynamic potential and pH, the Nernst equation is used to calculate the reduction potential of the oxidized species with respect to the standard hydrogen potential. The equilibrium formulae are calculated for the domains using the equations (1.2) and (1.3). FactSage module is used to calculate the Gibbs free energies of formation (ΔG^*) at higher temperatures and the corresponding E-pH equations are derived. All the reactions pertaining to equilibrium between different species in solution at different temperatures are calculated and tabulated (Table 1.1).

$$E(T) = E^{\circ}(T) - \frac{RT}{zF} lnQ \quad (1.2)$$

$$E(T) = -\frac{\Delta G(T)}{zF} \quad (1.3)$$

where, *E(T)* is the reduction potential at a temperature *T*, *E°(T)* is the standard reduction potential, *R* is the universal gas constant, *T* is the temperature in K, *z* is the number of moles of electrons transferred during reaction, *F* is the Faraday's constant and *Q* is the reaction quotient.

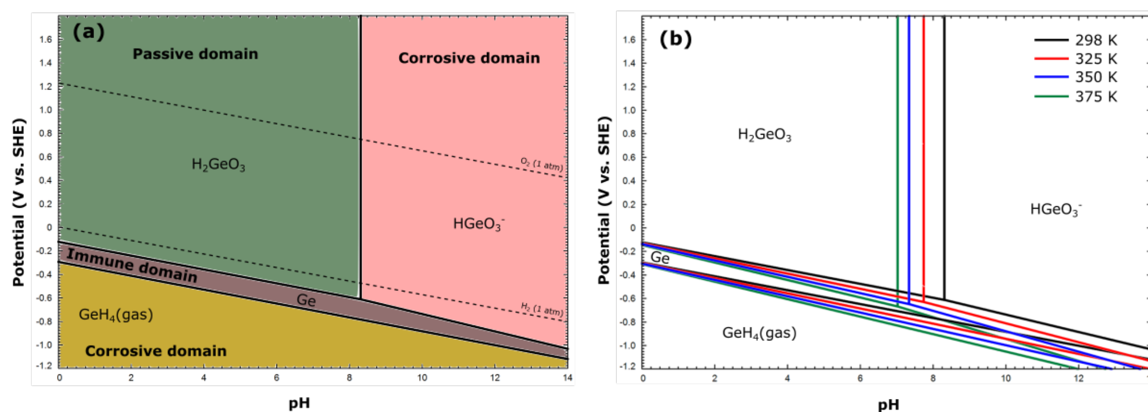

Figure 1.3. E-pH diagram of (a) Ge-H_2O system at room temperature and 1 atm pressure with most stable domains labeled and (b) Ge-H_2O system at 1 atm pressure for four different temperatures.

Using the reactions tabulated in Table 1.1, an equilibrium diagram for Ge-H_2O system at 298 K is constructed (Figure 1.3a). Each domain is labeled with the most stable species at that potential and pH. According to the diagram, Ge is a base metal, as its domain of thermodynamic stability lies entirely below that of water for the entire pH and potential ranges. It is not, therefore, thermodynamically stable in the presence of water. Ge tends to dissolve in aqueous solutions with high pH (alkaline) as $HGeO_3^-$ ions, and in neutral

and acidic solutions as H_2GeO_3 or GeO_2 precipitate. It can also be observed from the GeH_4 domain that a powerful reducing action can lead to the volatilization of Ge as its hydride. However, the conditions of formation of this hydride are not known with precision. It is evident from the Pourbaix diagram (Figure 1.3a) that electrodeposition of Ge from aqueous solution is thermodynamically not feasible due to the competing reduction of water to hydrogen gas and also in practice the growth is restricted to a few monolayers.[124–127]

Due to the lack of thermodynamic data, the species listed in Table 1.2 are not considered in the construction of the diagrams. The domain with elemental Ge is the only immune zone, below and above which there is corrosion into hydride or passivation into germanates, respectively. It can also be observed that a cathode immersed in a Ge solution can be a site of two following reactions: (i) Deposition of Ge and (ii) Evolution of H_2. The relative importance of these reactions depends mainly on the potential of the cathode, the pH of the solution, as well as on the overpotential of the reactions. Overpotential is the additional potential applied to the thermodynamic potential to overcome polarization, which is affected by change in parameters like temperature, pressure and concentration. A major component of the overpotential comes from the kinetics of the reaction. If a reaction is sluggish, a high overpotential must be applied. The stability of the Ge decreases with increasing temperature as shown in Figure 1.3b. The reduction potential at high pH is shifted towards more negative potentials with increasing temperature. The dashed lines across the entire pH range correspond to the redox potentials resultant from water oxidation or reduction. The changes in the pressure of the system will also influence the electrochemical stability of Ge species but the changes in the pressure of the system are not considered in this study.

Table 1.1. Species of Ge in equilibrium at various temperatures and their corresponding calculated E-pH equations[139]

Ge species	Equilibrium reaction	T (K)	Equilibrium/E-pH equation
Equilibrium between H_2GeO_3 and $HGeO_3^-$	$H_2GeO_3 = HGeO_3^- + H^+$	298	$\log [(HGeO_3^-) / (H_2GeO_3)] = -8.31 + pH$
		325	$\log [(HGeO_3^-) / (H_2GeO_3)] = -7.74 + pH$
		350	$\log [(HGeO_3^-) / (H_2GeO_3)] = -7.34 + pH$
		375	$\log [(HGeO_3^-) / (H_2GeO_3)] = -7.03 + pH$
Equilibrium between H_2GeO_3 and Ge	$Ge + 3H_2O = H_2GeO_3 + 4H^+ + 4e^-$	298	$E = -0.122 - 0.0591\ pH + 0.0148 \log (H_2GeO_3)$
		325	$E = -0.131 - 0.0644\ pH + 0.0161 \log (H_2GeO_3)$
		350	$E = -0.139 - 0.0694\ pH + 0.0174 \log (H_2GeO_3)$
		375	$E = -0.146 - 0.0744\ pH + 0.0186 \log (H_2GeO_3)$
Equilibrium between $HGeO_3^-$ and Ge	$3HGeO_3^- + 5H^+ + 4e^- = Ge + 3H_2O$	298	$E = -0.001 - 0.0738\ pH + 0.0148 \log (HGeO_3^-)$
		325	$E = -0.004 - 0.0806\ pH + 0.0161 \log (HGeO_3^-)$
		350	$E = -0.005 - 0.0868\ pH + 0.0174 \log (HGeO_3^-)$
		375	$E = -0.006 - 0.0930\ pH + 0.0186 \log (HGeO_3^-)$
Equilibrium between Ge and GeH_4	$GeH_4 = Ge + 4H^+ + 4e^-$	298	$E = -0.293 - 0.0591\ pH + 0.0148 \log (p_{GeH_4})$
		325	$E = -0.298 - 0.0644\ pH + 0.0161 \log (p_{GeH_4})$
		350	$E = -0.303 - 0.0694\ pH + 0.0174 \log (p_{GeH_4})$
		375	$E = -0.308 - 0.0744\ pH + 0.0186 \log (p_{GeH_4})$

Table 1.2. Various solid and ionic species of Ge which were not considered in the construction of the Pourbaix diagrams.

Solid species	GeO, $Ge(OH)_2$, $(GeH)_x$, $(GeH_2)_x$, Ge_2H_6, Ge_3H_8, Ge_4H_{10}
Dissolved species	$HGeO_2^-$, GeO_2^{2-}, $H_2Ge_5O_{11}$, $HGe_5O_{11}^-$, $Ge_5O_{11}^{2-}$

In conclusion, higher temperatures enable increased dissolved Ge species at lower pH. For the nanowire growth study on In metal, the Pourbaix diagram at 375K and 1 atm pressure is considered.

A phase diagram is useful to predict how a solvent or flux works because the adsorption, dissolving, mixing, diffusion, and precipitation of solids in the liquid phase are thermodynamic processes that work toward equilibrium. Figure 1.4 shows the phase diagram of Ge-In system,[140] which is referred to regarding the growth of Ge nanowires.[15]

For a metal catalyst to be used for the growth of nanowire, it must meet the following requirements. (1) It must form a liquid solution with a component of the solid phase. Ge-In form a eutectic at ca. 99.92% In. (2) The solubility limit of the solvent component in the liquid phase must be much higher than that in the solid phase (i.e., $K = C_s/C_l < 1$, where C_s is the solubility limit in the solid phase and C_l is the solubility limit in the liquid phase). Under this condition, the solvent easily leads to the formulation of the liquid alloy with little contamination in the solid phase. The solubility of Ge in In is 10^{-2} to 10^{-3} atom % In at about 800 °C. The solubility of In in Ge below the eutectic temperature is about $9\text{x}10^{-3}$ atom %. (3) It must be inert to chemical reactions. Otherwise, a reaction could deprive it of its catalytic function. It is evident from the phase diagram that Ge and In does not react to form a compound or solid solution. (4) It must not make an intermediate solid. Otherwise, the intermediate solid will also deprive it of its catalytic function. Indium satisfies all the requirements with Ge and thus allows the growth of Ge nanowires.

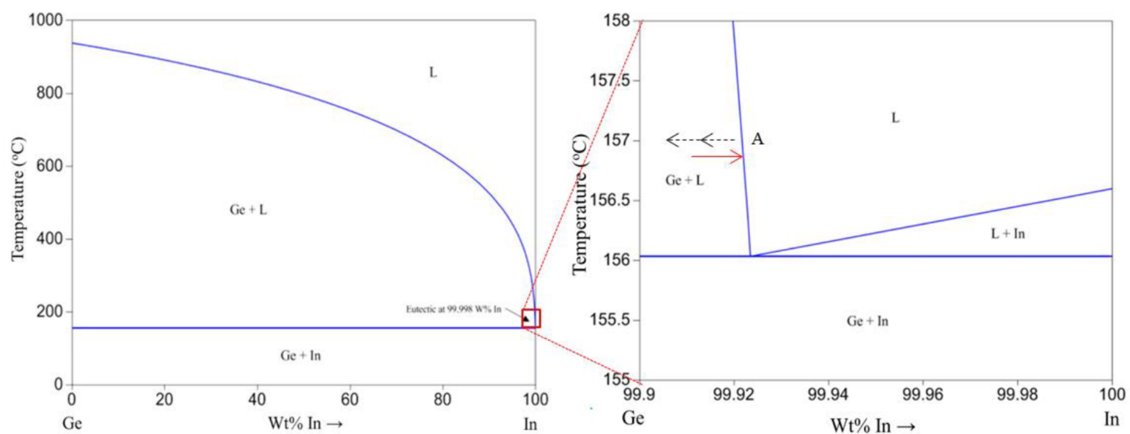

Figure 1.4. Phase diagram of Ge-In system with indication of the composition of liquid alloy catalyst in the course of growth of nanowires.

Thermodynamically, the minimum growth temperature for Ge must be higher than the eutectic point of the Ge-In system (156 °C). It is important to note that, the phase diagram shown in Figure 1.4 and the temperatures and compositions are for a bulk Ge-In system. A significant depression in the melting and eutectic temperature can be observed for nanosystems depending on the size of the nanomaterial. In this study, Ge is being electrodeposited onto nanoparticles of In in an aqueous solution at room temperature. The dissolved Ge species are initially reduced to Ge(s) followed by dissolution into the In nanoparticles. Continuous reduction and dissolution leads to saturation of Ge in In, leading to the precipitation of crystalline Ge nanowires. The composition of the Ge-In alloy above the eutectic point will follow the liquidus line (blue line with point A in Figure 1.4) that denotes equilibrium between the solid and liquid phases. Therefore, the composition of the liquid alloy can be found at the liquidus line at any temperature above the eutectic. However, due to the applied potential over the alloy during the nanowire electrodeposition, reduction of Ge from the solutions continues to occur and renders the alloy supersaturated with Ge. As a result, the composition of the alloy goes beyond the equilibrium composition, moving to the left side of the liquidus line (dotted black arrow). This supersaturated state is thermodynamically unstable and thus drives the precipitation of the solid phase from the supersaturated liquid

alloy until equilibrium is reached. The composition will then move back to the right and reach the liquidus line (solid red arrow). The composition of the precipitated solid phase corresponds to that of the phase boundary and thus should be pure Ge. Meanwhile, the composition of the alloy goes beyond the equilibrium composition again as Ge is reduced from the solution at the solvent electrode saturating the alloy and thus again drives the additional growth of nanowire with the precipitation at the interfaces. Transmission electron microscopy performed on a single Ge nanowire show the In content of 0.14 ± 0.04 atom % in Ge.[15] This value is much larger than the phase diagram predicted limit of 0.01 atom %. It is important to note that this large difference in solubility may arise from the fact that the phase diagram is constructed at equilibrium whereas the electrodeposition of Ge nanowires at room temperature is not.

The currently available experimentally constructed phase diagrams are from bulk systems and the thermodynamic properties of a nanosystem are different from those of a bulk system. The phase diagram of the type of nanometal catalyst that is occurring in this case differs from that of the bulk system and these phenomena may be due to the critical role of the surface energy in the nanosystem.[141–144] Regardless of the cause of the deviation, it should be considered that the different thermodynamic equilibrium of the nanosystem causes discrepancies between the actual growth behavior of nanowires through a nanometal catalyst and predictions on the basis of a diagram of the bulk system.

1.3.2.2. Electrodeposition of ZnO nanowires. ZnO is a semiconductor with a direct wide band gap of 3.36 eV and relatively high exciton binding energy (60 meV) at room temperature. ZnO nanowires have been widely studied for applications such as UV lasers,[145–146] light emitting diodes,[147–149] solar cells,[150–153] transparent conductive contacts,[154] sensors,[155–157] and photocatalysts[158–160] due to their unique electrical, optical and photonic properties. ZnO crystallizes in two main forms, cubic zinc blende

structure and hexagonal wurtzite structure. Over the past decade, many techniques have been proposed for the synthesis of ZnO with different size and morphologies including electrodeposition,[161–164] sol-gel,[165–168] hydrothermal,[77,169–170] and chemical vapor deposition.[171–173] Electrodeposition provides an inexpensive and large scale deposition with the possibility to control the morphology ranging from thin films to ordered nanowire arrays. One of the first reported electrochemical synthesis of ZnO consisted of an aqueous solution of Zn^{2+} ions, where electroreduction of oxygen precursor to hydroxide enables the precipitation of $Zn(OH)_2$, which at high temperatures (60 - 70 °C) dehydrates to ZnO.[161] Aqueous solutions mostly produce a nanowire or nanorod morphology. Therefore in an effort to produce thin films, studies using non-aqueous solution such as dimethylsulfoxide[174] and propylene carbonate[175] have also been performed. A simple chemical reaction for deposition of ZnO from an aqueous solution is shown in equations 1.4 and 1.5.

$$Zn^{2+} + 2OH^- \leftrightarrow Zn(OH)_2 \tag{1.4}$$

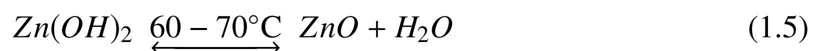

$$Zn(OH)_2 \underset{\longleftrightarrow}{60 - 70°C} ZnO + H_2O \tag{1.5}$$

The generation of hydroxide at the interface is usually achieved by either electrochemical reduction of molecular oxygen (O_2)[162,164,176] or nitrate ions (NO_3^-).[177–178] Molecular oxygen can be introduced into the solution by bubbling pure O_2 or O_2/Ar mixture to control the oxygen concentration. A purged saturated solution consists of about 10^{-3} M of oxygen at room temperature and about 8×10^{-4} M at 80 °C.[179] The electrochemical reduction of oxygen to hydroxide ion is a four-electron transfer reaction as shown in equation 1.6.

$$O_2 + 2H_2O + 4e^- \rightarrow 4OH^- \tag{1.6}$$

The standard reduction potential for this reaction is +0.40 V vs. standard hydrogen electrode,[179] however, due the sluggish kinetics and added overpotential, the reaction on an indium-tin oxide substrate occurs at -0.41 V vs. standard hydrogen electrode in a 0.1M KCl solution.[176]

Nitrate ions can also be used as a precursor for generation of hydroxide at the interface. Typically, $Zn(NO_3)_2$ is used as a source which acts as a precursor for both Zn^{2+} ions and OH^- ions. The mechanism of ZnO electrodeposition from a solution of $Zn(NO_3)_2$ is shown in equations 1.7 and 1.8.

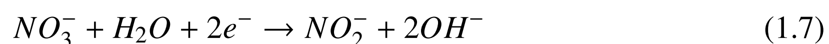

$$NO_3^- + H_2O + 2e^- \rightarrow NO_2^- + 2OH^- \tag{1.7}$$

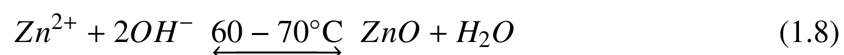

$$Zn^{2+} + 2OH^- \xleftrightarrow{60-70°C} ZnO + H_2O \tag{1.8}$$

In this research, ZnO nanowires are electrodeposited on a single-crystal Au foil using a solution consisting of 0.1 mM $Zn(NO_3)_2$ and 0.1 M KCl at an applied potential of -1.1 V versus Ag/AgCl at 70 °C and 200 rpm stirring. A detailed analysis on the epitaxially grown ZnO nanowires is discussed in Paper III.

1.4. RESEARCH OBJECTIVES

1.4.1. Epitaxial Electrodeposition of Au on Si as a Proxy for Single-Crystal Au.

Single-crystal Au is an excellent substrate for electrochemical epitaxial growth of metals, metal oxides and semiconductors due to its chemical inertness, but the high cost of bulk single crystal Au inhibits its use in practical application. The first objective of this research is to electrochemically grow epitaxial Au on wafer-size Si substrates as an inexpensive proxy for a single crystal substrate. Here, ultrathin epitaxial films of Au on Si(111), Si(100)

and Si(110) orientations are electrodeposited. The work on epitaxial electrodeposition of Au on Si is shown in Paper II.

1.4.2. Epitaxial Lift-off of Electrodeposited Single-Crystal Au Foils. Single-crystal silicon is the industry standard for electronic devices. However, the brittle nature of conventional Si wafers precludes their application in flexible electronic devices. There is interest in moving beyond conventional Si-based chips to produce flexible solar cells, flexible displays, and smart wearables. The second objective of this research is to use the epitaxial Au on Si substrate and selectively oxidize the Si to enable lift-off of a free-standing Au foil. The Au foil can then be used as a single-crystal, flexible and transparent substrate for flexible electronics.The successful lift-off of the single-crystal Au foils from Si is shown in Paper III.

1.4.3. Fabrication of $Ru^{II}(bpy)_3$ Based Organic Light Emitting Diode and Epitaxial Cu_2O Inorganic Diode on Au Foil. To evaluate the flexibility and transmittance of the Au foil, we spin-coated an organic light emitting diode based on tris(bipyridyl)ruthenium(II). The complex showed a strong electroluminescence around 600 nm with a bright red-orange emission. To study the single-crystal nature of Au foils, we electrodeposited epitaxial Cu_2O with an indium-gallium eutectic contact to form an inorganic Schottky diode. An improved diode quality factor was observed for epitaxial Cu_2O when compared to a polycrystalline deposit. The work on fabrication of an OLED and inorganic diode is shown in Paper III.

1.4.4. Electrodeposition of Epitaxial ZnO and Polycrystalline Ge Nanowires. The applicability of Au foils as a flexible substrate was shown by depositing epitaxial ZnO nanowires and subjecting them up to 500 bending cycles. The ZnO nanowires remained intact after the bending cycles, attributed to the nanowire morphology and flexibility of Au foils. A new one-step technique is introduced to electrodeposit Ge nanowires on In nanoparticles from an aqueous solution at ambient conditions. The Ge nanowire growth

is demonstrated on a polycrystalline indium-tin oxide substrate and future experiments are proposed to grow epitaxial Ge nanowires on Au foils. The data for electrochemical deposition of Ge nanowires is shown in Paper I and the growth of ZnO nanowires on flexible substrate is demonstrated in Paper III.

PAPER

I. ELECTRODEPOSITED GERMANIUM NANOWIRES

Naveen K. Mahenderkar[1], Ying-Chau Liu[2], Jakub A. Koza[2], and Jay A. Switzer[2,*]

[1]Department of Materials Science and Engineering and Graduate Center for Materials Research, Missouri University Science and Technology Rolla, Missouri, 65409.

[2]Department of Chemistry and Graduate Center for Materials Research, Missouri University Science and Technology Rolla, Missouri, 65409.

*Email: jswitzer@mst.edu

ABSTRACT

Germanium (Ge) is a group IV semiconductor with superior electronic properties compared with silicon, such as larger carrier mobilities and smaller effective masses. It is also a candidate anode material for lithium-ion batteries. Here, a simple, one-step method is introduced to electrodeposit dense arrays of Ge nanowires onto indium tin oxide (ITO) substrates from aqueous solution. The electrochemical reduction of ITO produces In nanoparticles that act as a reduction site for aqueous Ge(IV) species, and as a solvent for the crystallization of Ge nanowires. Nanowires deposited at 95 °C have an average diameter of 100 nm, whereas those deposited at room temperature have an average diameter of 35 nm. Both optical absorption and Raman spectroscopy suggest that the electrodeposited Ge is degenerate. The material has an indirect bandgap of 0.90 - 0.92 eV, compared with a value of 0.67 eV for bulk, intrinsic Ge. The blue shift is attributed to the Moss-Burstein effect, because the material is a p-type degenerate semiconductor. On the basis of the magnitude of the blue shift, the hole concentration is estimated to be 8x10^{19} cm^{-3}. This corresponds to an In impurity concentration of about 0.2 atom %. The resistivity of the wires is estimated to

be 4x10^{-5} Ω.cm. The high conductivity of the wires should make them ideal for lithium-ion battery applications.

Keywords: degenerate semiconductor; electrodeposition; germanium nanowires; indium nanoparticles; Moss-Burstein shift

1. INTRODUCTION

Germanium (Ge) is a group IV semiconductor material that was used in the first transistor prior to silicon (Si).[1] It has twice the electron mobility (3900 $cm^2/(V.s)$), four times the hole mobility (1900 $cm^2/(V.s)$), a larger exciton Bohr radius (24 nm), and a lower hole effective mass ($0.28m_o$) compared with Si.[2,3] Because of its high carrier mobility, Ge is being considered as a replacement for Si as the active channel material for CMOS transistors.[4–6] Ge is also an attractive anode material for Li-ion batteries, because it has a larger theoretical charge - discharge capacity than graphite.[7,8] However, it undergoes a 370 % change in volume, leading to fragmentation and loss of electrical contact in bulk electrodes.[9] Nanostructures of Ge have been shown to accommodate the large volumetric changes during Li intercalation.[7,10–12] The room temperature (RT) diffusivity of Li in Ge is 400 times higher than that in Si, indicating that Ge may be an attractive electrode material for high-power-rate anodes.[13] Nanowires of Ge grown using various methods showed a discharge capacity in the range of 600 - 1140 mAh/g.[14,15] Despite its superior properties, the lack of inexpensive and simple methods to produce nanostructured Ge has limited its use. Electrodeposition of Ge from aqueous solution is thermodynamically not feasible, and in practice the growth is restricted to a few monolayers due to the competing reduction of water to hydrogen gas.[16–19] Recently, Maldonado and co-workers electrodeposited nanostructures of Ge from aqueous solutions on various metallic liquids (Hg, Ga and In) using a new route that they call the electrochemical liquid-liquid-solid (ec-LLS) process.[14,20–22] This process utilizes a metallic liquid electrode that acts both as an electrode for electrodeposition and as a solvent

for recrystallization. Nanostructured filaments of Ge on liquid Hg,[20] Ge nanowires on In nanoparticles,[14] and epitaxial Ge nanowires on Ga nanodroplets[21,22] were electrodeposited. Here, we show a simple one-step method to grow dense arrays of Ge nanowires utilizing the ec-LLS process directly on indium-tin oxide (ITO) substrates from aqueous solution. The electrochemical reduction of ITO decorates the substrate with In nanoparticles, which act both as a reduction site for dissolved Ge species and as a solvent for crystallization of the Ge nanowires.

2. RESULTS AND DISCUSSION

The reaction scheme we use to produce the Ge nanowires on ITO substrates is shown in Figure 1. The electrochemical reduction of ITO decorates the substrate with In nanoparticles, which act both as a reduction site for dissolved Ge(IV) species and as a solvent for crystallization of the nanowires. The dissolved Ge(IV) species are initially reduced to Ge(s) followed by dissolution into the In nanoparticles. Continuous reduction and dissolution leads to saturation of Ge in In, leading to the crystallization of Ge nanowires. Electrochemical reduction of ITO forms an In nanoparticle on the surface (Figure 1b). The In nanoparticle in contact with the ITO acts as the electrode for the reduction of Ge(IV) and also dissolves the reduced Ge into the particle. Upon reaching saturation, the Ge starts to crystallize out of the nanoparticle allowing the growth of the nanowire (Figure 1c). A key to the reaction scheme is that ITO electrochemically reduces to In at a potential very similar to the potential at which Ge(IV) is reduced to Ge at the In nanoparticles.

The electrochemical reduction of ITO and formation of In nanoparticles was studied using linear sweep voltammetry. Figure 2 shows the current-potential responses of ITO in the solution, both without (dashed line) and with (solid line) aqueous Ge(IV). All of the potentials in the article are *versus* Ag/AgCl/(sat. KCl). A significant increase in current density occurs at -1.15 V during the first scan of ITO in the solution without Ge(IV) (open

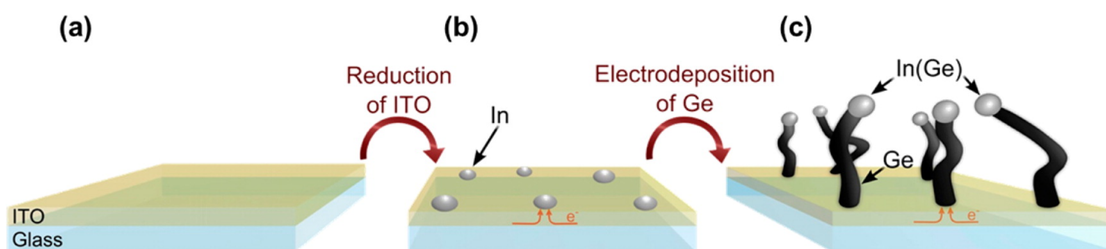

Figure 1. Schematic of electrodeposition of Ge nanowires. (a) The as-received ITO in an aqueous electrolyte of Ge(IV). (b) Electrochemical reduction of ITO to In nanoparticles dispersed evenly over the entire surface of ITO. (c) Ge nanowires grow on ITO with In nanoparticles at the tip of the nanowires.

circle dashed line). This increase in current density is due to the reduction of ITO to In nanoparticles. The electrochemical reduction of ITO to In nanoparticles was also reported by Huang *et al.*[23] During the second scan (solid circle dashed line), the current density increase is very minimal, indicating an almost complete reduction of ITO and surface coverage with In nanoparticles.

The first cathodic scan with Ge(IV) (open circle, solid line) in the solution shows an increase in the current density nearly at the same potential of -1.15 V. This indicates that the presence of Ge(IV) in the solution did not affect the potential at which ITO reduces. However, during the second scan (solid circle, solid line), the current density increase occurs at a more positive potential of -0.7 V, indicating the reduction of Ge(IV) due to the presence of In on the surface of ITO. The ITO in a Ge(IV) solution shows no evidence of Ge deposition at potentials positive of -1.15 V. On the contrary, a reduced ITO (with In nanoparticles) shows an increase in current density at potentials between -0.7 and -1.15 V, indicating that reduction of Ge(IV) occurs exclusively at the In nanoparticles. An In(s) foil used as a working electrode also showed a reduction current at nearly the same potential (-0.79 V) as that for the In nanoparticles, confirming that Ge(IV) reduction occurs on In (Supporting Information, Figure S1). The single-step growth of Ge nanowires occurs mainly due to the reduction potential of ITO being very similar to that of reduction of Ge(IV) on In (see

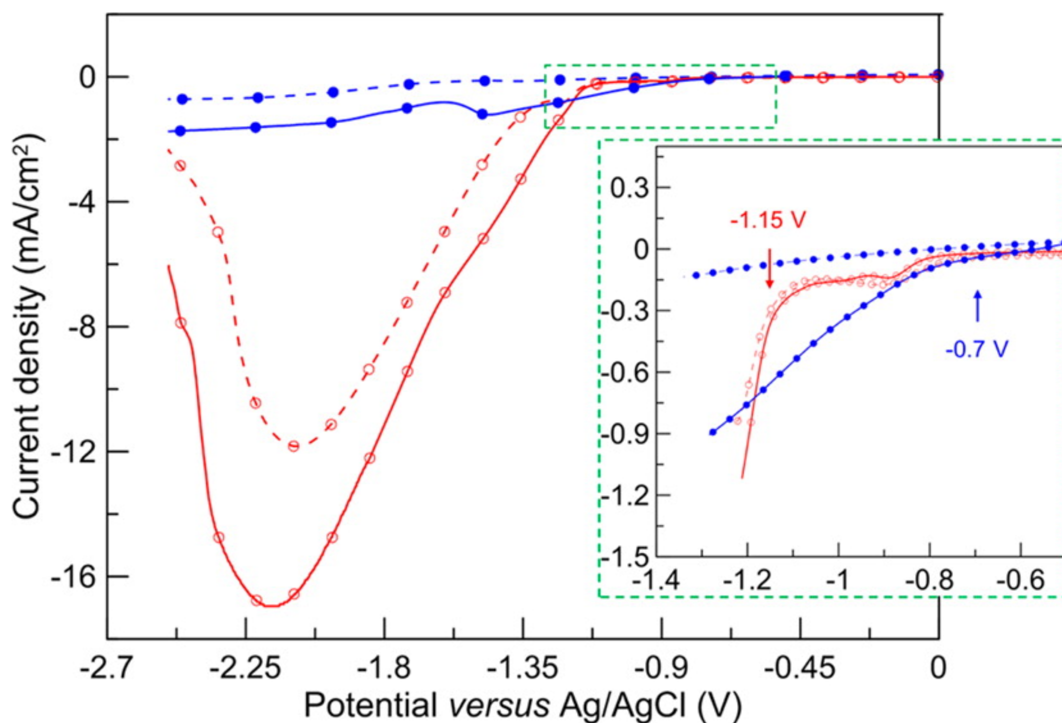

Figure 2. Electrochemical data for Ge nanowire electrodeposition. Linear sweep voltammograms for the reduction of ITO and Ge nanowire deposition. Solid lines are the linear scans of ITO in a solution with 50 mM Ge(IV) and the dashed lines are without Ge(IV). Lines with hollow circles are the first scans, and lines with solid circles are the second scans. The scans were performed from 0 to -2.5 V *versus* Ag/AgCl at 100 mV/s. Inset shows the magnified view of the onset reduction potentials.

Figure 2 inset). The poor electrocatalytic activity of In for H^+ reduction enables continuous reduction of Ge(IV) over the nanoparticle surface.[24] As a result, the potential in a single solution can be controlled to reduce the ITO prior to the deposition of Ge nanowires. All of the nanowire samples for further investigations are prepared by applying -1.3 V for 10 min. The deposits are thoroughly rinsed with deionized water and dried in air prior to analysis. The as-prepared samples appear dark black in color and eventually become light gray after a prolonged (1-2 months) exposure to a lab atmosphere.

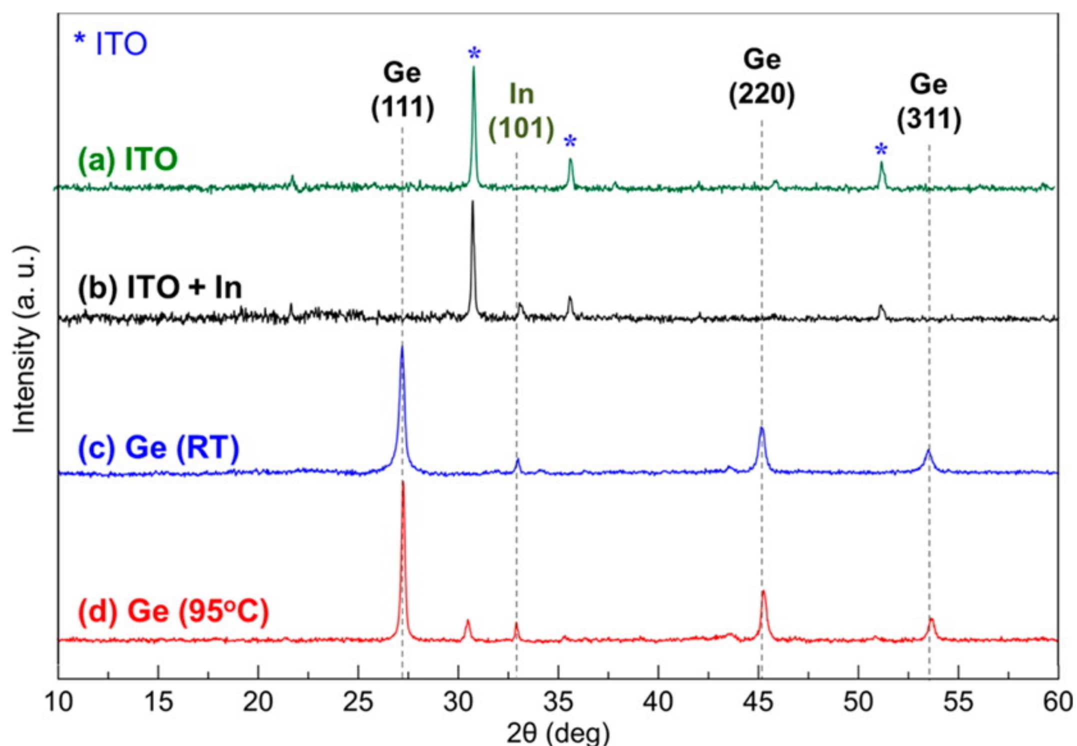

Figure 3. Crystallinity of Ge nanowires. X-ray diffraction patterns of ITO (a), reduced ITO (b), and Ge nanowires deposited at room temperature (c) and 95 °C (d). Ge reflections are indicated as black dashed vertical lines (JCPDS card no. 4-0545); asterisks stand for the ITO substrate.

The Ge deposition was also probed by X-ray diffraction (XRD). The XRD pattern of the ITO shows strong reflections of In_2O_3, with no evidence of In (Figure 3a). The reduced ITO, however, shows reflections of both ITO and In (Figure 3b). This shows that the spherical particles formed on the surface of ITO are In. Using the Scherrer equation,[25] we estimate an average X-ray coherence length of 60 nm for the In nanoparticles. To study the effect of deposition temperature, the nanowires were deposited at 95 °C and RT. Ge nanowires at both of the deposition temperatures show strong XRD peaks for crystalline Ge (Figures 3c and 3d). The line broadening in XRD of the Ge deposits gives an average crystallite size of 50 nm for Ge deposited at 95 °C and 30 nm for the Ge deposited at room temperature. Precision lattice parameters determined using the Nelson-Riley extrapolation[26] applied to the pattern of reflections (Supporting Information, Figure S2) are 5.6582 Å (for 95 °C) and

5.6707 Å (for RT). These are both in good agreement with the expected lattice parameter of 5.6579 Å for bulk Ge.[27,28]

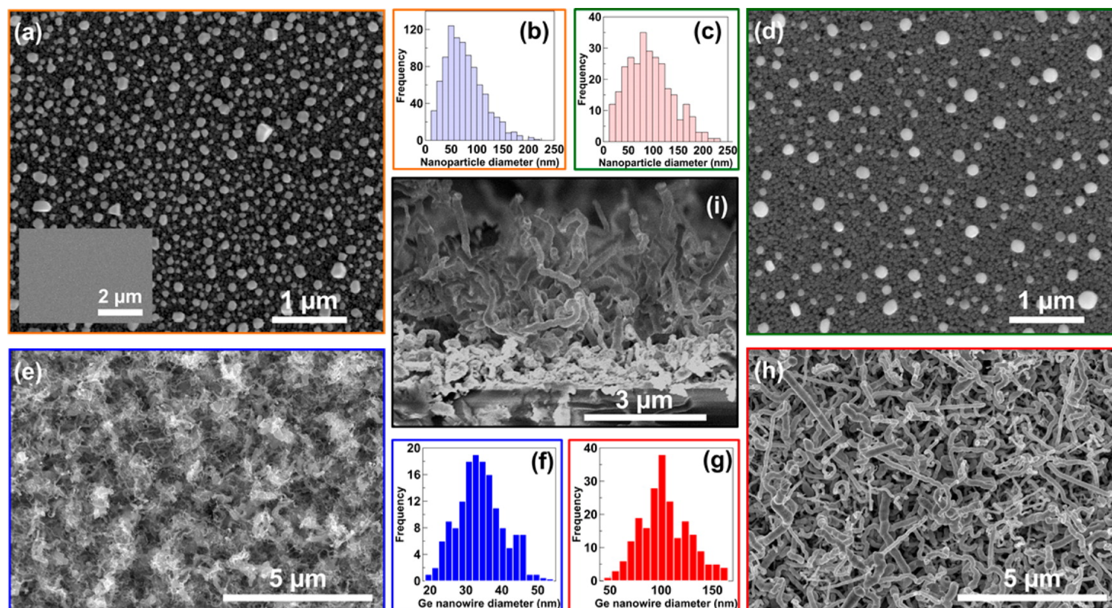

Figure 4. Morphology of In nanoparticles and Ge nanowires. SEM of ITO reduced at room temperature (a) with an average particle size of 50 nm (b) and the ITO reduced at 95 °C (d) with an average particle size of 100 nm (c). The inset in (a) shows the as-received ITO prior to reduction. Ge nanowires deposited at room temperature (e) with an average nanowire diameter of 35 nm (f) and deposited at 95 °C (h) with an average diameter of 100 nm (g). Cross section of nanowires deposited at 95 °C (i).

The morphology of as-received ITO (inset of Figure 4a) is smooth and does not show any evidence of elemental In on the surface. The reduced ITO shows numerous, uniformly dispersed, relatively spherical In nanoparticles (Figure 4a,d). An average In particle size of 50 nm for RT (Figure 4b) and 100 nm for 95 °C reduction (Figure 4c) is observed. The presence of both ITO and the In nanoparticles suggests that incomplete reduction occurred. This enables electrical contact to the In nanoparticles for the reduction of Ge(IV). It is also evident from the size distribution that with increase in temperature of reduction, the nanoparticle size increases. Figure 4e shows the Ge nanowires deposited at room temperature and Figure 4h shows the Ge nanowires produced at 95 °C. An average nanowire diameter of 35 nm (Figure 4f) for the room temperature deposit and 100 nm

(Figure 4g) for the 95 °C deposit is observed. The size of the In nanoparticles and the Ge nanowire diameters are comparable. That is, large nanoparticles yield large-diameter nanowires. A spaghetti-like morphology is evident for both the deposition temperatures. A dense array of Ge nanowires can be deposited directly onto an ITO substrate at ambient conditions. Figure 4i shows the cross section of the nanowires deposited at 95 °C.

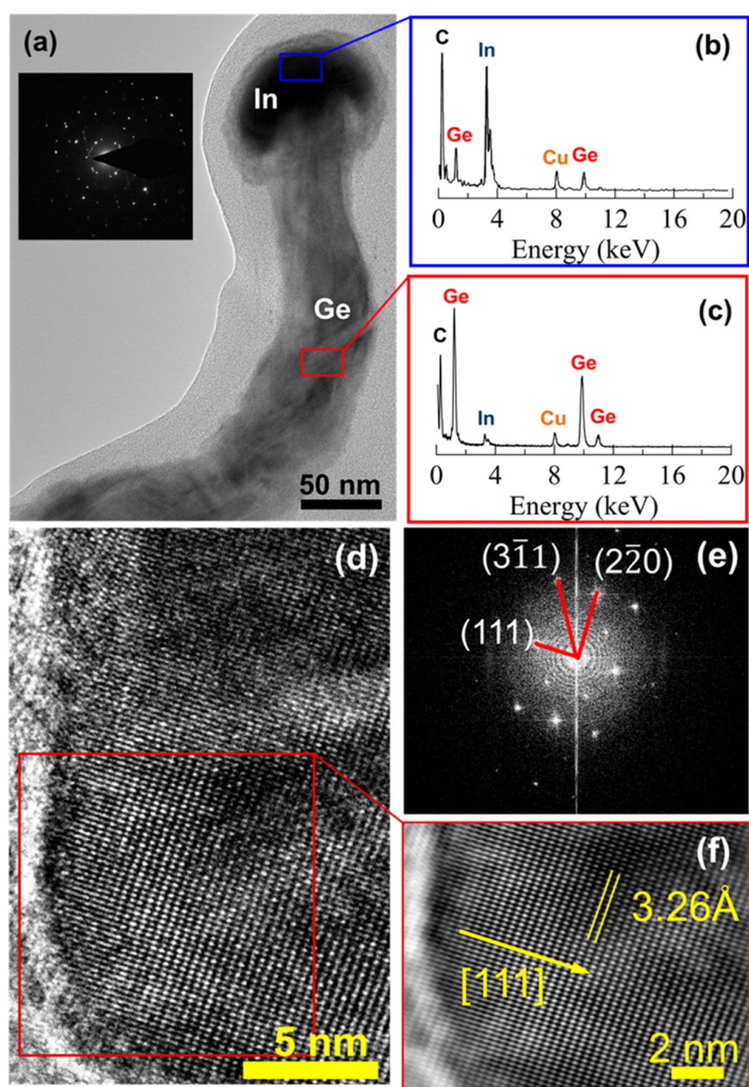

Figure 5. (a) TEM of a single Ge nanowire deposited at 95 °C with an In nanoparticle at the tip of the wire. Inset shows the selected area electron diffraction pattern of the nanowire. EDS spectrum with the compositions of In nanoparticle (b) and Ge nanowire (c). (d) High-resolution TEM of Ge nanowire, (e) diffractogram corresponding to the high-resolution TEM image in (d), and (f) reconstructed high-resolution image with the (111) d-spacing and the [111] direction indicated.

Figure 5a shows a transmission electron microscope (TEM) image of a Ge nanowire with an In nanoparticle at the tip of the wire that was deposited at 95 °C. Energy dispersive X-ray spectroscopy (EDS) performed on both the In tip (Figure 5b) and the Ge nanowire (Figure 5c) verify the compositions of the Ge wire and the In tip. The EDS of the In nanoparticle tip shows a composition of approx. 20 atom percent Ge and 80 atom percent In. The presence of Ge in In implies the dissolution of Ge in In during the reduction of Ge(IV). EDS of the nanowire shows that it is predominately Ge with a small amount (0.14 ± 0.04 atom %) of In. The inset in Figure 5a is the electron diffraction of the nanowire with a polycrystalline spot pattern. The variations in contrast along the nanowire also suggest that the nanowire is polycrystalline, in agreement with the XRD patterns. It is also evident that the In nanoparticle stays on top of the nanowire while the ITO provides the electrical contact. Figure 5d shows a high-resolution TEM image of the nanowire deposited at 95 °C. Figure 5e shows the diffractogram of the high-resolution image shown in Figure 5d. The spots in the diffractogram reveal the direction of growth and the d-spacing value. Figure 5f is a reconstructed high-resolution TEM image of the same nanowire from the diffractogram. The spacing between the lattice planes is measured to be 3.26 Å, in agreement with the spacing of (111) planes for diamond cubic Ge.

The bandgap of an electrodeposited Ge was estimated from a plot of square root of absorbance versus photon energy (Figure 6a). As described in the Supporting Information (Supporting Information, Figure S3), the absorbance was corrected for scattering of the light by the Ge nanowires. The linear plots in Figure 6a are consistent with an indirect bandgap.[2] The transition in Ge is indirect due to the position of the conduction band minimum at the L symmetry point of the Brillouin zone edge and the valence band maximum at the Γ symmetry point of the Brillouin zone center. The indirect transition process involves a photon and also a phonon that is either emitted or absorbed in the excitation event. The phonon energy in an indirect transition is normally on the order of 0.01 eV, so the intercept

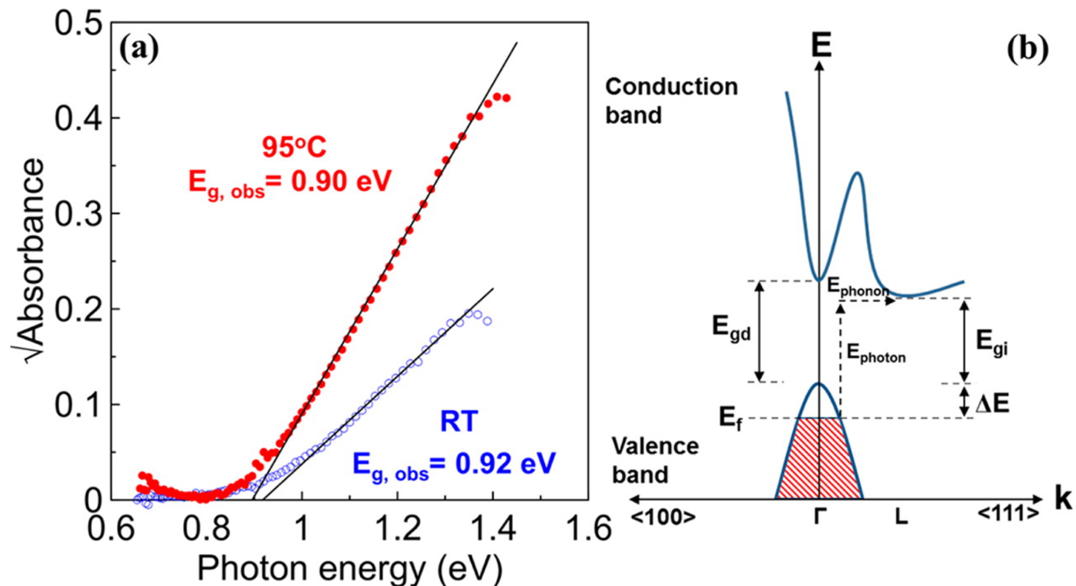

Figure 6. Optical bandgap measurements of Ge nanowires. (a) Square root of absorbance as a function of photon energy for Ge nanowires deposited at 95 °C (red solid circle) and room temperature (blue hollow circle). The energy-intercept of the fit to the linear region of the curve is the indirect bandgap. (b) Schematic diagram of the band structure for a degenerate p-Ge. The increase in energy (ΔE) is the Moss-Burstein shift due to the high carrier concentration.

is a close approximation to the actual bandgap of the nanowires. An optical bandgap of 0.92 eV (for 95 °C) and 0.90 eV (for RT) is observed from the absorbance data. Ge has an intrinsic bandgap of 0.67 eV, which gives a blue shift (ΔE) of 0.25 eV (for 95 °C) and 0.23 eV (for RT). Although a blue shift is expected for quantum confinement in nanoscale materials, the size of our nanowires is too large to account for this large shift. We attribute the blue shift to the fact that the electrodeposited Ge is doped with In to degeneracy. Indium is a p-type dopant for Ge. If the doping density is very high, the Fermi level can be shifted to an energy below the valence band. Figure 6b shows the schematic diagram of the band structure for a degenerate p-Ge. The shift of Fermi energy due to high carrier concentration can result in a blue shift in the absorption spectrum, known as the Moss-Burstein shift.[2,29] The carrier density can be estimated from the blue shift using the Moss-Burstein equation (eq 1).

$$\Delta E(eV) = E_f - E_v = \frac{\hbar^2(3\pi^2 n)^{2/3}}{2m_h^*} \quad (1)$$

Here, is the Moss-Burstein shift; E_f is the Fermi energy level; E_v is the energy at the top of valence band; $\hbar$ is the reduced Planck's constant; m_h^* is the effective hole mass, and n is the charge carrier density. With eq 1, the hole densities are calculated to be 8.4x10^{19} cm^{-3} (for 95 °C) and 7.4x10^{19} cm^{-3} (for RT). The optical bandgap and the carrier densities of the nanowires for both of the deposition temperatures are nearly the same within the experimental error of the measurement.

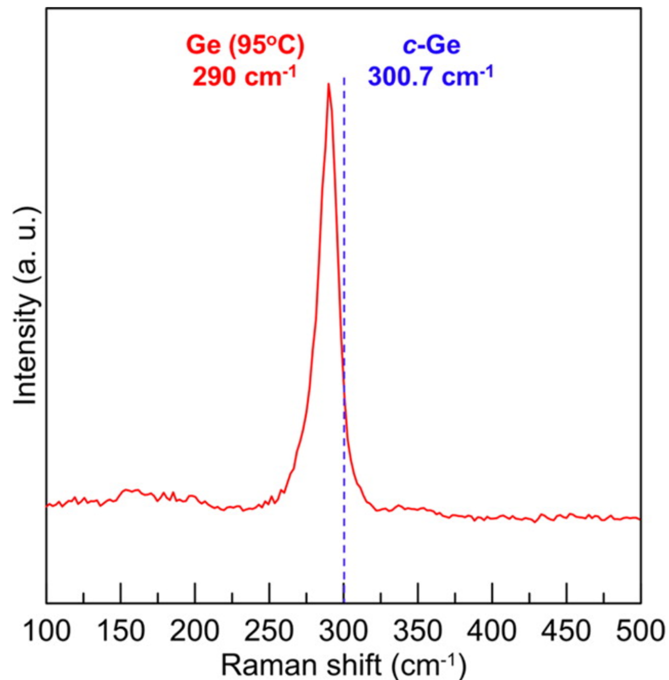

Figure 7. Raman spectrum of Ge nanowires deposited at 95 °C (red solid line); the blue dashed line corresponds to the first-order Stokes peak for crystalline bulk Ge.

The Ge nanowire sample was also probed using Raman spectroscopy to study the effect of carrier concentration and nanowire size on the Raman shift. The first-order Stokes peak for bulk crystalline Ge occurs at 300.7 cm^{-1}.[30] Several groups have studied the effect of carrier concentration (phonon-plasmon coupling),[31,32] and crystal and nanowire size (phonon confinement effect) on the Raman shift.[33,34] Contributions from any of these effects

cause a redshift and broadening of the Raman peaks. The Ge nanowires deposited at 95 °C show a redshift of ca. 10 cm^{-1}, with the peak of Ge shifted to 290 cm^{-1} (Figure 7). The blue dashed line in Figure 7 shows the first-order Stokes peak for bulk crystalline Ge and the red solid spectrum corresponds to the Ge nanowires deposited at 95 °C. This characteristic redshift for the nanowires is attributed to the presence of a high carrier concentration in the nanowires, consistent with a previous study by Cerdeira and Cardona.[32] We assume that the crystallite size and nanowire diameter are too large compared to the Bohr radius of Ge (24 nm) to show significant red shifts due to the phonon confinement effect.

The hole concentrations calculated from eq 1 can be used to estimate the In concentration in the Ge. The unit cell of Ge has a volume of 1.799×10^{-22} cm^3, and contains 8 Ge atoms. There are, therefore, 4.455×10^{22} Ge atoms per cm^3. If we assume that each hole in the material results from one substitutional In atom, the concentration of In in the Ge is 0.16 atom % for the wires grown at room temperature and 0.18 atom % for the wires grown at 95 °C. These calculated In concentrations agree well with the In content of 0.14 ± 0.04 atom % that was measured by EDS in the TEM for the Ge nanowire grown at 95 °C. We can also estimate the resistivity of the Ge nanowires based on the measured hole concentrations and the known bulk mobility of holes in Ge. The calculated resistivity is 3.8×10^{-5} Ω.cm (for 95 °C) and 4.4×10^{-5} Ω.cm (for RT). This indicates that the nanowires have a very high conductivity enabling the growth of long Ge nanowires, even at room temperature. Hence, the electrodeposited Ge nanowires may be too highly doped for conventional electronic applications, but they should be ideal as a high-capacity anode material for lithium ion batteries.

3. CONCLUSIONS

In summary, we have demonstrated the electrodeposition of crystalline Ge nanowires at room temperature by direct electroreduction of ITO in a single-step from aqueous solution. The similarity of the reduction potentials of ITO and Ge(IV) enables this single-step potentiostatic growth of Ge nanowires. The nanowires are deposited at 95 °C and room temperature, and the effect of temperature on the crystallinity, nanowire diameter, crystal size, and optical bandgap is examined. The nanowires deposited at both temperatures are polycrystalline. The grain size and the nanowire diameter decrease with a decrease in deposition temperature, consistent with the decrease in the diameter of the initially formed In nanoparticles. The In nanoparticles stay on top of the nanowires during the growth with the ITO at the base providing the electrical contact. The dissolution of Ge in In nanoparticle supports the notion of growth by dissolution and crystallization by the electrochemical liquid-liquid-solid (ec-LLS) mechanism proposed by Madonaldo and co-workers.[14,20–22] The optical bandgap of the material blue shifts due to the high carrier density (ca. $8x10^{19}$ cm^{-3}). The resistivity of the nanowires is estimated to be very low (ca. $4x10^{5}$ Ω.cm), enabling the growth of long wires even at room temperature.

4. MATERIALS AND METHODS

The Ge nanowires were electrodeposited at room temperature and 95 °C from a solution of 50 mM GeO_2, 0.5 M Na_2SO_4, and 0.1 M $C_4H_6O_4$ (succinic acid) with the pH adjusted to 6.5 using NaOH. The same solution without GeO_2 was used for the electrochemical reduction studies of ITO to In nanoparticles. Electrochemical measurements were performed with a potentiostat/galvanostat (EGG model 273A). A platinum mesh was used as the counter electrode, and an Ag/AgCl/(sat. KCl) was used as the reference electrode.

The crystallinity of the nanowires was characterized using a high-resolution Philips X-Pert MRD X-ray diffractometer with a Cu K_{α_1} radiation source (λ = 1.5405 Å). The morphology of the films was determined by means of scanning electron microscopy (Helios NanoLab 600 DualBeam and Hitachi S4700 field-emission). The transmission electron microscopy and energy dispersive spectroscopy of the nanowires and the In nanoparticles were measured using the Tecnai F20. Samples for TEM analysis were prepared by etching ITO with Ge nanowires using 1:1 (v/v) HCl solution and sonicating the wires in ethanol for 5 min. The suspension was then drop-cast onto copper grids coated with ultrathin carbon films on holey carbon (Pacific Grid Tech).

The bandgap measurements were performed using a dual beam UV-vis-NIR spectrophotometer (Varian Cary 5). The as-prepared Ge nanowire films were etched using a 1:1 (v/v) HCl solution to dissolve the ITO. A drop of etching solution cast on the nanowire film enabled the etching of ITO without causing the nanowire film to slide off the glass. The glass with nanowires was then dried and used for the absorbance measurements. This ensured that the absorbance was solely due to the nanowires. Raman measurements were carried out using a Horiba Jobin-Yvon LabRam Aramis Microscope with a HeNe laser (λ = 633 nm) as the excitation source with an incident power of 0.5 mW to minimize sample heating. The as-deposited Ge nanowire samples were rinsed using deionized (DI) water, dried in air, and used without any post processing.

SUPPORTING INFORMATION

Chemicals. Solutions were prepared with high purity reagents and nanopure deionized water (resistivity > 18 MΩ.cm). The electrolyte consisted of 50 mM GeO_2 (99.998%, Sigma Aldrich), 0.5 M Na_2SO_4 (≥99%, Sigma Aldrich) as supporting electrolyte and 0.1 M succinic acid, $C_4H_6O_4$ (≥99.8%, Fisher Scientific) as complexing agent, with the pH adjusted to about 6.5 using NaOH (≥98%, Sigma Aldrich). Acetone (Certified ACS, Fisher)

was used to clean the substrates. 1:1 (v/v) hydrochloric acid, 37% (Certified ACS, Sigma Aldrich) in water was used to etch the indium tin oxide (ITO). Ethanol (≥99.5%, Sigma Aldrich) was used to disperse Ge nanowires for TEM analysis. ITO on glass substrates with ca. 1-2% SnO_2 (DRLI Co.) were used as working electrodes.

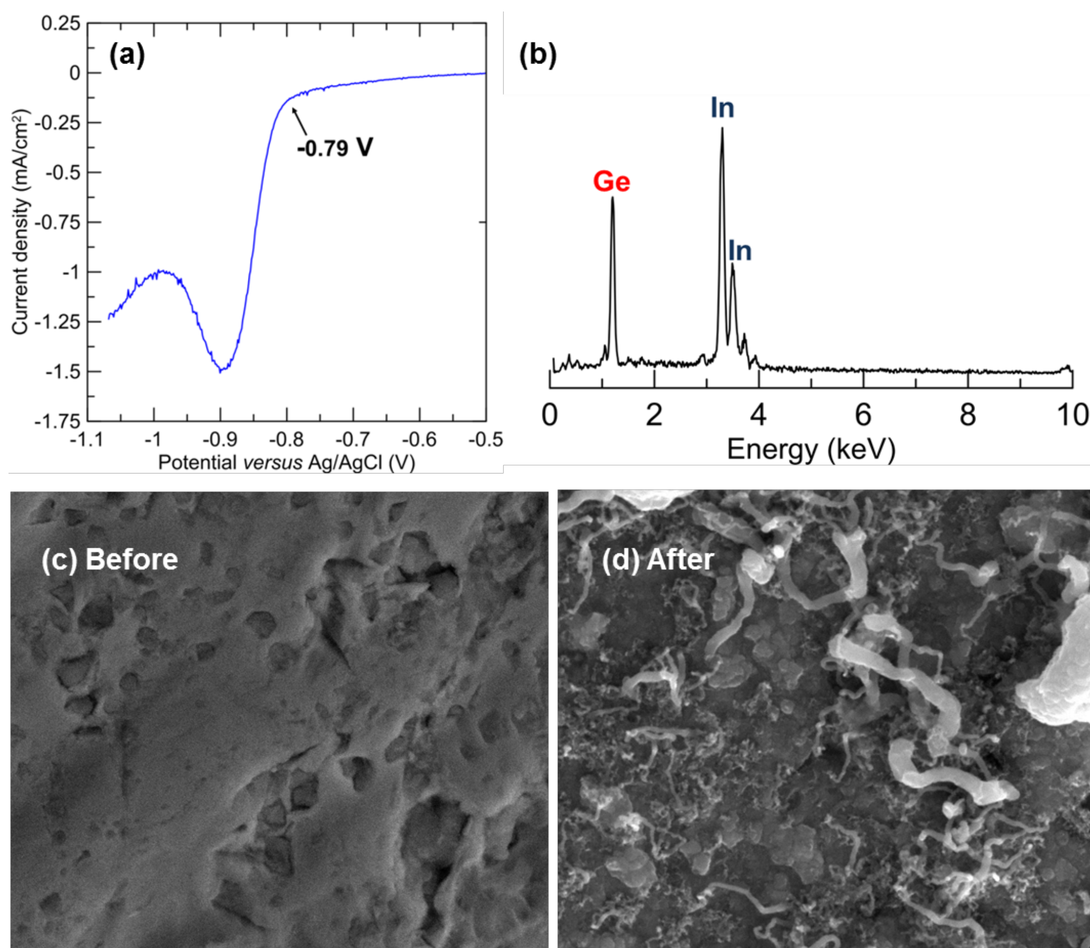

Figure S1. (a) Linear sweep voltammogram of In foil in a solution with Ge(IV) at a scan rate of 100 mV/s. (b) Energy dispersive spectroscopy of In foil with Ge nanowires. (c) Scanning electron microscope images of In foil before (c) and after (d) Ge deposition.

Ge Electrodeposition on Bulk In. The current-potential curves for electrodeposition of Ge were also recorded on an In(s) electrode to verify the hypothesis that the reduction of Ge(IV) occurs exclusively at the In nanoparticles. The potential for reduction of about -0.79 V *versus* Ag/AgCl (Figure S1a) was in close agreement with the reduction

potential on ITO with the In nanoparticles (-0.7 V *versus* Ag/AgCl). The electrodeposition was performed by applying a constant potential of -1 V *versus* Ag/AgCl for 5 min. Energy dispersive spectroscopic analysis after the deposition (Figure S1b) showed the presence of Ge. The SEM images of the In foil before (Figure S1c) and after (Figure S1d) the electrodeposition show the formation of nanowires of Ge on the surface of the In.

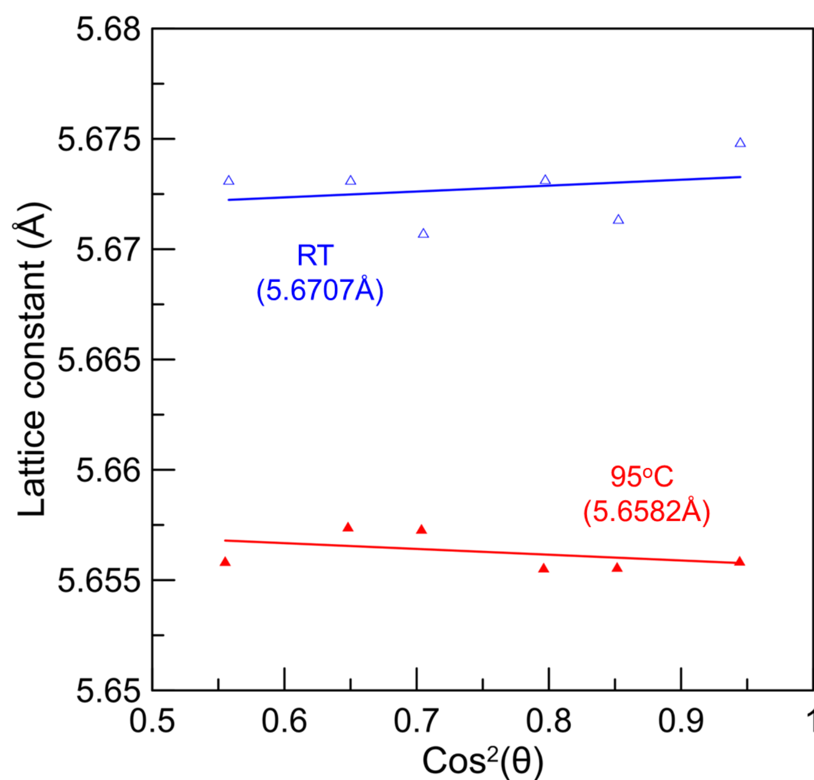

Figure S2. Nelson-Riley extrapolation for the determination of precision lattice parameter of Ge nanowires deposited at 95 °C (red solid triangle) and room temperature (blue hollow triangle).

Precision Lattice Parameter Measurement. Precision lattice parameters were determined for the Ge nanowires using the Nelson Riley extrapolation method.[26] A lattice parameter of 5.6582 Å for the 95 °C deposit and 5.6707 Å for the room-temperature deposit were determined from the intercept of the ordinate at $\theta = 90°$ (Fig. S2). Both the lattice parameters were close to the expected diamond cubic lattice parameter for Ge.[27,28]

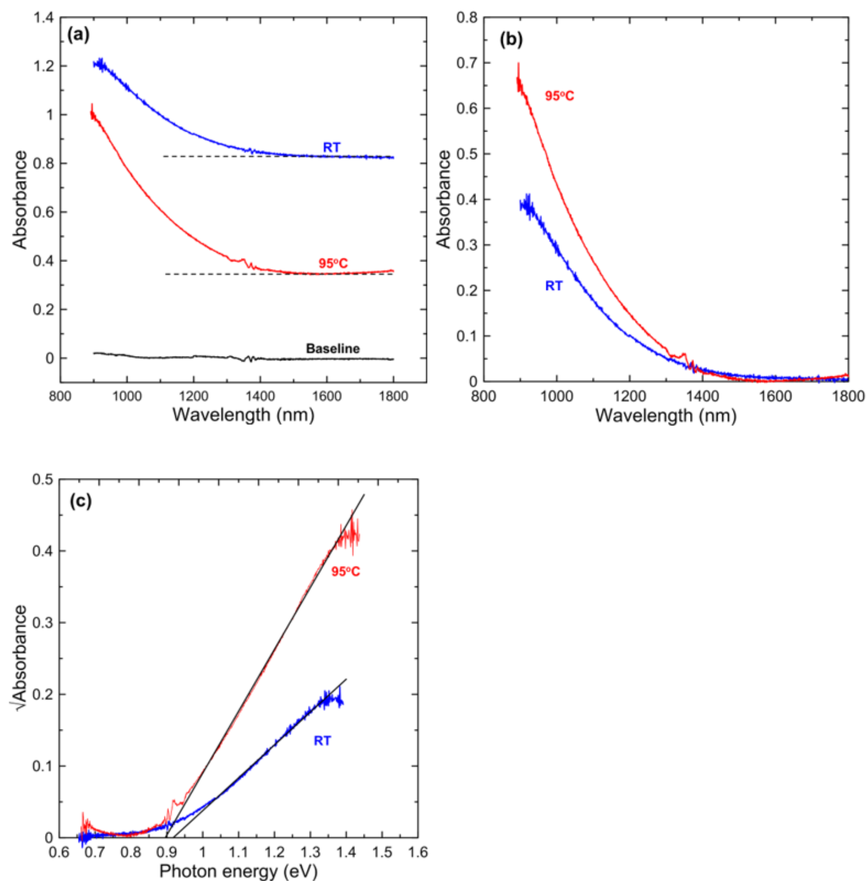

Figure S3. (a) Absorption spectrum of ITO etched Ge nanowires deposited at room-temperature (blue), 95 °C (red) and 100% T baseline (black). The dashed lines show the absorbance due to scattering in the nanowires. (b) Corrected absorption spectrum of ITO etched Ge nanowires with absorbance subtracted due to scattering. (c) Plot of square root of corrected absorbance versus photon energy for both the deposition temperatures to determine the indirect bandgaps.

Bandgap Measurement for Ge Nanowires. The bandgap of the nanowires was determined in the transmission mode using a Cary 5 dual beam UV-Vis-NIR spectrophotometer. To avoid any contribution from the substrate, ITO was dissolved before all the absorption measurements were performed. The as-deposited Ge nanowire samples were etched with a few drops of dilute HCl to dissolve the ITO followed by evaporation of etchant leaving the nanowires dispersed on glass. During the measurements a glass substrate without ITO was placed in the path of the reference beam to account for the contribution from

the glass. The absorption spectra of the ITO etched nanowires for both the deposition temperatures are shown in Fig. S3a. The nanowires show a constant but appreciable amount of absorbance in the longer wavelength range of the spectra shown with dashed lines in Fig. S3a. We attribute this constant absorbance at longer wavelength to scattering of the light by the nanowires. The absorbance for nanowires produced at both deposition temperatures is fairly constant in the range of 1800 - 1400 nm before rising at wavelengths less than about 1350 nm. The constant absorbance for the respective deposition temperatures was subtracted from the curves to eliminate the scattering contribution (Figure S3b). The indirect bandgap of Ge was then estimated from a plot of the square root of the corrected absorbance versus the photon energy (Figure S3c).

ACKNOWLEDGMENTS

This material is based upon work supported by the U.S. Department of Energy, Office of Basic Energy Sciences, Division of Materials Sciences and Engineering, under Grant No. DE-FG02-08ER46518. The authors declare no competing financial interest.

REFERENCES

1. Bardeen, J.; Brattain, W. H. The Transistor, a Semi-Conductor Triode. *Phys. Rev.* **1948**, 74, 230-231.
2. Pankove, J. I. *Optical Processes in Semiconductors*; Dover Publications: New York, 1975.
3. Yu, B.; Sun, X. H.; Calebotta, G. A.; Dholakia, G. R.; Meyyappan, M. One-Dimensional Germanium Nanowires for Future Electronics. *J. Cluster Sci.* **2006**, 17, 579-597.
4. Chui, C. O.; Ramanathan, S.; Triplett, B. B.; McIntyre, P. C.; Saraswat, K. C. Germanium MOS Capacitors Incorporating Ultrathin High-κ Gate Dielectric. *IEEE Electron Device Lett.* **2002**, 23, 473-475.
5. Maeda, T.; Ikeda, K.; Nakaharai, S.; Tezuka, T.; Sugiyama, N.; Moriyama, Y.; Takagi, S. High Mobility Ge-on-Insulator p-Channel MOSFETs Using Pt Germanide Schottky Source/ Drain. *IEEE Electron Device Lett.* **2005**, 26, 102-104.
6. Bojarczuk, N. A.; Copel, M.; Guha, S.; Narayanan, V.; Preisler, E. J.; Ross, F. M.; Shang, H. Epitaxial Silicon and Germanium on Buried Insulator Heterostructures and Devices. *Appl. Phys. Lett.* **2003**, 83, 5443-5445.
7. Graetz, J.; Ahn, C. C.; Yazami, R.; Fultz, B. Nanocrystalline and Thin Film Germanium Electrodes with High Lithium Capacity and High Rate Capabilities. *J. Electrochem. Soc.* **2004**, 151, A698-A702.
8. Yoon, S.; Park, C.-M.; Sohn, H.-J. Electrochemical Characterizations of Germanium and Carbon-Coated Germanium Composite Anode for Lithium-Ion Batteries. *Electrochem. Solid-State Lett.* **2008**, 11, A42-A45.
9. Song, T.; Cheng, H.; Town, K.; Park, H.; Black, R. W.; Lee, S.; Park, W. I.; Huang, Y.; Rogers, J. A.; Nazar, L. F.; et al. Electrochemical Properties of Si-Ge Heterostructures as an Anode Material for Lithium Ion Batteries. *Adv. Funct. Mater.* **2014**, 24, 1458-1464.
10. Lee, H.; Kim, M. G.; Choi, C. H.; Sun, Y.-K.; Yoon, C. S.; Cho, J. Surface-Stabilized Amorphous Germanium Nanoparticles for Lithium-Storage Material. *J. Phys. Chem. B* **2005**, 109, 20719-20723.
11. Rudawski, N. G.; Darby, B. L.; Yates, B. R.; Jones, K. S.; Elliman, R. G.; Volinsky, A. A. Nanostructured Ion Beam-Modified Ge Films for High Capacity Li Ion Battery Anodes. *Appl. Phys. Lett.* **2012**, 100, 083111.
12. Park, M. H.; Kim, K.; Kim, J.; Cho, J. Flexible Dimensional Control of High-Capacity Li-Ion-Battery Anodes: From 0D Hollow to 3D Porous Germanium Nanoparticle Assemblies. *Adv. Mater.* **2010**, 22, 415-418.

13. Chan, C. K.; Zhang, X. F.; Cui, Y. High Capacity Li Ion Battery Anodes Using Ge Nanowires. *Nano Lett.* **2007**, 8, 307-309.

14. Gu, J.; Collins, S. M.; Carim, A. I.; Hao, X.; Bartlett, B. M.; Maldonado, S. Template-Free Preparation of Crystalline Ge Nanowire Film Electrodes via an Electrochemical Liquid-Liquid-Solid Process in Water at Ambient Pressure and Temperature for Energy Storage. *Nano Lett.* **2012**, 12, 4617-4623.

15. Kennedy, T.; Mullane, E.; Geaney, H.; Osiak, M.; O'Dwyer, C.; Ryan, K. M. High-Performance Germanium NanowireBased Lithium-Ion Battery Anodes Extending Over 1000 Cycles through in Situ Formation of a Continuous Porous Network. *Nano Lett.* **2014**, 14, 716-723.

16. Hall, J. I.; Koenig, A. E. Electrochemical Properties of Germanium. Trans. *Electrochem. Soc.* **1934**, 65, 215-219.

17. Szekely, G. Electrodeposition of Germanium. *J. Electrochem. Soc.* **1951**, 98, 318-324.

18. Liang, X.; Jayaraju, N.; Stickney, J. L. Aqueous Ge Atomic Layer Deposition on Au. *ECS Trans.* **2007**, 11, 249-258.

19. Liang, X.; Kim, Y. G.; Gebergziabiher, D. K.; Stickney, J. L. Aqueous Electrodeposition of Ge Monolayers. *Langmuir* **2010**, 26, 2877-2884.

20. Carim, A. I.; Collins, S. M.; Foley, J. M.; Maldonado, S. Benchtop Electrochemical Liquid-Liquid-Solid Growth of Nanostructured Crystalline Germanium. *J. Am. Chem. Soc.* **2011**, 133, 13292-13295.

21. Fahrenkrug, E.; Gu, J.; Jeon, S.; Veneman, P. A.; Goldman, R. S.; Maldonado, S. Room-Temperature Epitaxial Electrodeposition of Single-Crystalline Germanium Nanowires at the Wafer Scale from an Aqueous Solution. *Nano Lett.* **2014**, 14, 847-852.

22. Ma, L.; Gu, J.; Fahrenkrug, E.; Maldonado, S. Electrochemical Liquid-Liquid-Solid Deposition of Crystalline Ge Nanowires as a Function of Ga Nanodroplet Size. *J. Electrochem. Soc.* **2014**, 161, D3044-D3050.

23. Huang, C. A.; Li, K. C.; Tu, G. C.; Wang, W. S. The Electrochemical Behavior of Tin-Doped Indium Oxide During Reduction in 0.3 M Hydrochloric Acid. *Electrochim. Acta* **2003**, 48, 3599-3605.

24. Butler, J. N.; Dienst, M. Hydrogen Evolution at a Solid Indium Electrode. *J. Electrochem. Soc.* **1965**, 112, 226-232.

25. Patterson, A. The Scherrer Formula for X-Ray Particle Size Determination. *Phys. Rev.* **1939**, 56, 978-982.

26. Nelson, J. B.; Riley, D. P. An Experimental Investigation of Extrapolation Methods in the Derivation of Accurate Unit Cell Dimensions of Crystals. *Proc. Phys. Soc.* **1945**, 57, 160.

27. Baker, J. F. C.; Hart, M. An Absolute Measurement of the Lattice Parameter of Germanium Using Multiple-Beam X-Ray Diffractometry. *Acta Crystallogr., Sect. A* **1975**, 31, 364-367.

28. Cooper, A. Precise Lattice Constants of Germanium, Aluminum, Gallium Arsenide, Uranium, Sulphur, Quartz and Sapphire. *Acta Crystallogr.* **1962**, 15, 578-582.

29. Burstein, E. Anomalous Optical Absorption Limit in InSb. *Phys. Rev.* **1954**, 93, 632-633.

30. Parker, J. H., Jr.; Feldman, D. W.; Ashkin, M. Raman Scattering by Silicon and Germanium. *Phys. Rev.* **1967**, 155, 712-714.

31. Sanson, A.; Giarola, M.; Napolitani, E.; Impellizzeri, G.; Privitera, V.; Carnera, A.; Mariotto, G. Study of Carrier Concentration Pro files in Al-Implanted Ge by Micro-Raman Spectroscopy under Different Excitation Wavelengths. *J. Raman Spectrosc.* **2013**, 44, 1097-4555.

32. Cerdeira, F.; Cardona, M. Effect of Carrier Concentration on the Raman Frequencies of Si and Ge. *Phys. Rev. B* **1972**, 5, 1440-1454.

33. Jalilian, R.; Sumanasekera, G. U.; Chandrasekharan, H.; Sunkara, M. K. Phonon Confinement and Laser Heating Effects in Germanium Nanowires. *Phys. Rev. B* **2006**, 74, 155421.

34. Wang, X.; Shakouri, A.; Yu, B.; Sun, X.; Meyyappan, M. Study of Phonon Modes in Germanium Nanowires. *J. Appl. Phys.* **2007**, 102, 014304.

II. NANOMETER-THICK GOLD ON SILICON AS A PROXY FOR SINGLE-CRYSTAL GOLD FOR THE ELECTRODEPOSITION OF EPITAXIAL CUPROUS OXIDE THIN FILMS

Jay A. Switzer[1,*], James C. Hill[1,Ψ], Naveen K. Mahenderkar[2], and Ying-Chau, Liu[1]

[1]Department of Chemistry and Graduate Center for Materials Research, Missouri University Science and Technology Rolla, Missouri, 65409.

[2]Department of Materials Science and Engineering and Graduate Center for Materials Research, Missouri University Science and Technology Rolla, Missouri, 65409.

[*]Email: jswitzer@mst.edu

ABSTRACT

Single-crystal Au is an excellent substrate for electrochemical epitaxial growth due to its chemical inertness, but the high cost of bulk Au single crystals prohibits their use in practical applications. Here, we show that ultrathin epitaxial films of Au electrodeposited onto Si(111), Si(100), and Si(110) wafers can serve as an inexpensive proxy for bulk single-crystal Au for the deposition of epitaxial films of cuprous oxide (Cu_2O). The Au films range in thickness from 7.7 nm for a film deposited for 5 min to 28.3 nm for a film deposited for 30 min. The film thicknesses are measured by low-angle X-ray reflectivity and X-ray Laue oscillations. High-resolution TEM shows that there is not an interfacial SiO_x layer between the Si and Au. The Au films deposited on the Si(111) substrates are smoother and have lower mosaic spread than those deposited onto Si(100) and Si(110). The mosaic spread of the Au(111) layer on Si(111) is only 0.15° for a 28.3 nm thick film. Au films deposited onto degenerate Si(111) exhibit ohmic behavior, whereas Au films deposited onto n-type Si(111) with a resistivity of 1.15 Ω.cm are rectifying with a barrier height of 0.85 eV. The Au and the Cu_2O follow the out-of-plane and in-plane orientations of the Si substrates, as determined by X-ray pole figures. The Au and Cu_2O films deposited on Si(100) and Si(110)

are both twinned. The films grown on Si(100) have twins with a [221] orientation, and the films grown on Si(110) have twins with a [411] orientation. An interface model is proposed for all Si orientations, in which the -24.9% mismatch for the Au/Si system is reduced to only +0.13% by a coincident site lattice in which 4 unit meshes of Au coincide with 3 unit meshes of Si. Although this study only considers the deposition of epitaxial Cu_2O films on electrodeposited Au/Si, the thin Au films should serve as high-quality substrates for the deposition of a wide variety of epitaxial materials.

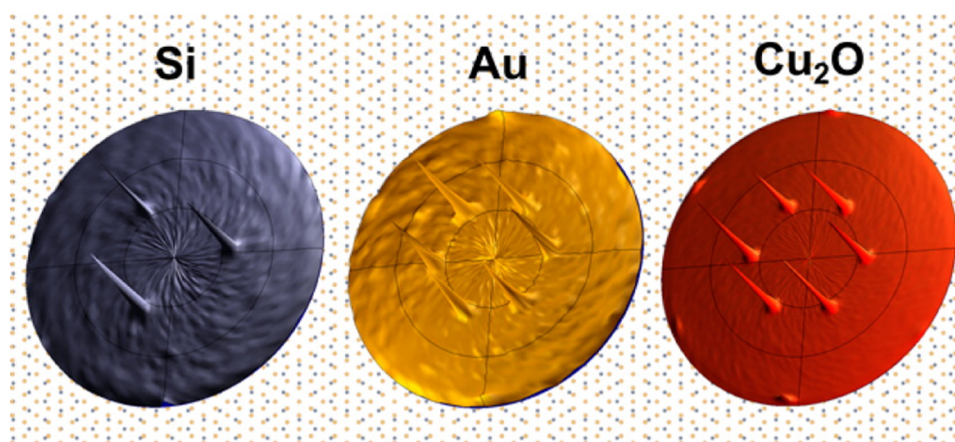

Keywords: coincident site lattice; cuprous oxide; electrodeposition; epitaxy; gold; silicon; thin films

1. INTRODUCTION

Gold metal electrodes are a preeminent choice for electrochemical studies due to their chemical inertness. Single-crystal Au has also been used extensively as a substrate for the electrodeposition of thin layers of metals by underpotential deposition (UPD)[1–3] and as a substrate for epitaxial growth of semiconductors.[4–8] Our group has been involved with the epitaxial electrodeposition of thin films and superlattices of metal oxide ceramics for several years. We define epitaxy as the growth of crystalline films on an ordered substrate in which the out-of-plane and in-plane orientation of the film is controlled by the substrate. Epitaxial films can provide superior electronic or optical properties because of the low

number of grain boundaries that can act as defects or electron-hole recombination sites. Although some work has been done in our laboratory on single-crystal Si[9] and InP[10–12] substrates, the majority of our epitaxial films have been electrodeposited onto single-crystal Au. Examples of epitaxial ceramic films that we have electrodeposited on Au include δ-Bi_2O_3,[13,14] Cu_2O,[15–17] ZnO,[18,19] Fe_3O_4,[20–24] CuO,[25,26] SnS,[27] $CoFe_2O_4$,[28] Mn_3O_4,[29] Co_3O_4,[30] and methylammonim lead iodide perovskites.[31] We have also electrodeposited ceramic superlattices based on PbO_2/Tl_2O_3 [32–35] and $Fe_3O_4/ZnFe_2O_4$ [23,28] onto single-crystal Au. Although single-crystal Au does provide a platform for studies of the basic science behind epitaxial electrodeposition, there is little probability that these epitaxial systems will be technologically exploited, due to the very high cost and small size (about 1 cm^2) of Au single crystals. Hence, an inexpensive alternative to Au single crystals is needed.

Researchers have used vapor-deposited Au layers on glass and mica as a proxy for single-crystal gold for the deposition of self-assembled monolayers.[36] However, the Au layers on glass are only [111]-oriented out-of-plane with no in-plane order, and the Au layers on mica have deep grooves between the [111]-oriented crystals. The Au on mica samples have large enough grains for scanning probe microscopy studies, but they do not have long-range, in-plane order that extends across the entire sample. Researchers have also produced epitaxial Au nanostructures on Si(111) and Si(100) substrates by galvanic displacement, in which the Si substrate acts as a reducing agent to deposit the epitaxial Au.[37] Although the Au nanostructures produced by galvanic displacement do follow the orientation of the Si substrates, the Au islands grow by the Volmer-Weber mechanism. This method, therefore, does not produce smooth Au films that mimic the surface of single-crystal Au substrates.

Allongue and co-workers pioneered an electrochemical method to grow thin, ultra-flat Au(111) epitaxial buffer layers on hydrogen-terminated Si(111).[38,39] Although metal films typically grow three-dimensionally on Si, and there is typically an SiO_x interlayer, the

Allongue group showed that Au deposited at large negative potentials (ca., -2 V *versus* the mercury sulfate electrode) at which there was concomitant evolution of hydrogen gas were very smooth and epitaxial and did not have an interfacial SiO_x layer. They deposited the Au onto 0.2 ° miscut Si(111) oriented toward $[11\bar{2}]$ with a long-range staircase structure. The goal of their work was to produce ultrathin layers of nonmagnetic substrates for the epitaxial growth of ultrathin magnetic metals, in order to probe the effects of thickness on the magnetic properties of the metals.[40,41]

Here, we show that nanometer-thick electrodeposited epitaxial layers of Au on Si(111), Si(100), and Si(110) can serve as a proxy for bulk single-crystal Au for the electrodeposition of epitaxial thin films of cuprous oxide (Cu_2O). Although this work focuses on the deposition of Cu_2O on Au/Si, the epitaxial Au/Si substrates will provide a platform for the deposition of a wide variety of epitaxial ceramic and semiconductor thin films. The highly ordered Au/Si substrates can be synthesized at a small fraction of the cost of bulk Au single crystals because of the low mass (i.e., micrograms) of Au that is used, they can conceivably be made as large as a Si wafer, and they may allow for the integration of electrodeposited functional ceramics with traditional semiconductor devices. In addition, the Au/Si interface is an interesting example of epitaxy, because high-quality, smooth Au epitaxial films are produced even though there is a -24.9% lattice mismatch between the Au film and Si substrate.

2. RESULTS AND DISCUSSION

Ultrathin films of Au were electrodeposited onto Si(111), Si(100), and Si(110) substrates using the method developed by Allongue and co-workers for the deposition of Au onto Si(111).[38,39] The deposition was performed on wafers with n-type doping, and on degenerately doped wafers. The n-Si(111) was miscut 0.2 ° toward $[11\bar{2}]$ with a resistivity

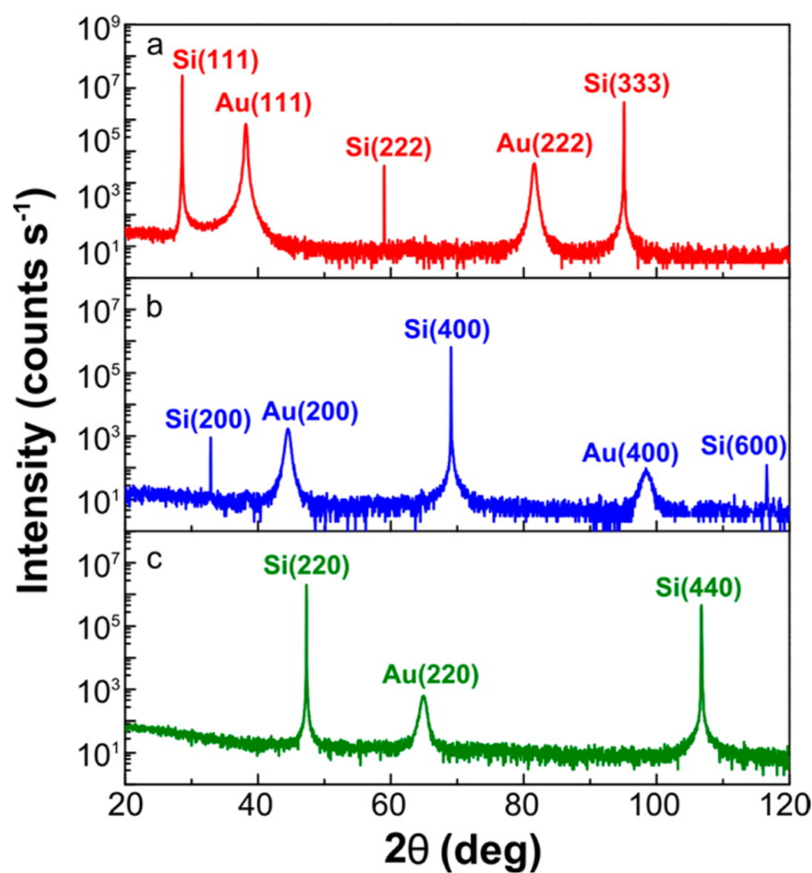

Figure 1. X-ray diffraction patterns of Au on Si. Out-of-plane orientation of electrodeposited (a) Au(111) on Si(111), (b) Au(100) on Si(100), and (c) Au(110) on Si(110).

of 1.15 Ω.cm, the n^{++}-Si(100) had a resistivity of 0.001 Ω.cm, and the p^{++}-Si(110) had a resistivity of 0.005 Ω.cm. The miscut Si(111) will hereafter be referred to simply as Si(111). The deposition was done at room temperature in a solution containing 0.1 mM $HAuCl_4$, 1 mM KCl, 1 mM H_2SO_4, and 0.1 M K_2SO_4 using a Si electrode that was prepolarized at -1.9 V *versus* Ag/AgCl before inserting it in the deposition solution. X-ray diffraction (XRD) patterns of films that were deposited for 30 min onto Si(111), Si(100), and Si(110) are shown in Figure 1. The XRD patterns show that the Au follows the out-of-plane orientation of the Si for all three orientations. The Au peaks are broader than the Si peaks primarily because of the nanoscale thickness (i.e., short X-ray coherence length) of the Au films.

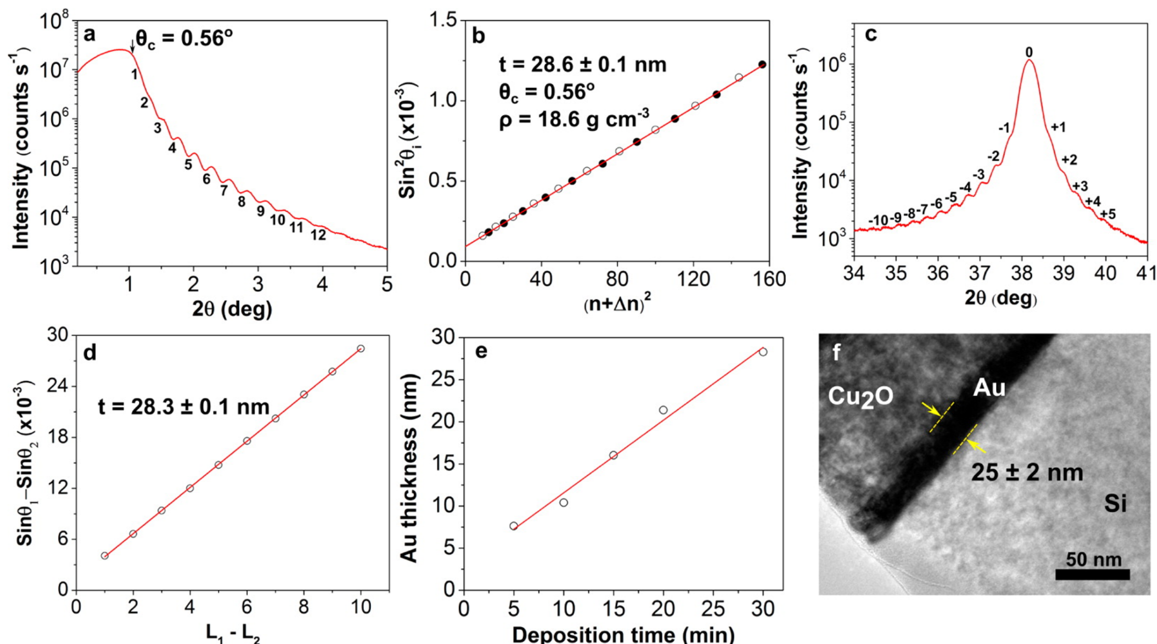

Figure 2. Thickness measurement of Au(111) on Si(111) by X-ray reflectivity, Laue oscillations, and TEM. (a) Low-angle X-ray reflectivity for a 30 min Au(111) on Si(111) deposit showing air-Au and Au-Si interference fringes (Kiessig fringes). (b) Plot of $\sin^2 \theta_i$ versus $(n+\Delta n)^2$ for the reflectivity data from (a) using eq 1. (c) Out-of-plane X-ray diffraction showing satellite peaks (Laue oscillations) corresponding to the X-ray coherence length of Au on Si. (d) Plot of $\sin\theta_1 - \sin\theta_2$ versus $L_1 - L_2$ for the Laue oscillations from (c) using eq 3. (e) Plot of Au thickness measured by the Laue oscillations as a function of deposition time. (f) TEM cross-section of Cu_2O/Au/Si layers with Au thickness of 25 ± 2 nm in close agreement with X-ray measurements.

The Au thickness on the Si wafers can be measured by X-ray diffraction. Constructive and destructive interference of X-rays that are reflected from the Au-air and Si-Au interfaces manifests itself as interference fringes in low-angle X-ray reflectivity (Kiessig fringes)[42,43] and as satellites flanking the Bragg peaks at higher angles (Laue oscillations).[23,28] These fringes and satellites are only observed for very smooth, nanometer-thick films. In our work, they were observed for films deposited onto Si(111) but not for films deposited onto Si(100) or Si(110). Kiessig fringes in the low-angle X-ray reflectivity are shown in Figure 2a for an Au film that was deposited for 30 min onto n-Si(111) with a resistivity of 1.15 Ω.cm. The Kiessig fringes can be used to calculate the Au film thickness and density from

$$\sin^2\theta_i = (n_i + \Delta n)^2 \left(\frac{\lambda}{2t}\right)^2 + \sin^2\theta_c \tag{1}$$

$$\rho = \left(\frac{\theta_c^2 \pi A}{N_A r_e \lambda^2 f}\right) \tag{2}$$

where θ_i is the Kiessig fringe angle, n_i is the fringe order of the minima, (n_i+ Δn) is the fringe order of the maxima (with Δn = 1/2), λ is the X-ray wavelength (0.15418 nm), t is the film thickness, θ_c is the critical angle, ρ is the film density (g cm^{-3}), N_A is Avogadro's number ($6.023x10^{23}$), r_e is the radius of the electron ($2.818x10^{-13}$ cm), f is the atomic scattering factor for Au [79], and A is the atomic mass for Au (196.97 g mol^{-1}).[42,43] Figure 2b shows a plot of $\sin^2\theta_i$ versus $(n+\Delta n)^2$ for the reflectivity data from Figure 2a. Fringe maxima are denoted as closed circles, whereas fringe minima are denoted as open circles. The slope of the plot ($(\lambda/2t)^2$) gives a film thickness of 28.6 ± 0.1 nm, and the intercept ($\sin^2\theta_c$) gives a critical angle of 0.56°. The density of the film calculated from eq 2 is 18.6 g cm^{-3}. Because the bulk density of Au is 19.31 g cm^{-3}, this measurement shows that the electrodeposited Au is 96.3% dense. Laue oscillations around the Au(111) peak are shown in Figure 2c for the same Au film. The film thickness can be determined from the satellite positions in the XRD pattern using

$$t = \left(\frac{(L_1 - L_2)\lambda}{2(\sin\theta_1 - \sin\theta_2)}\right) \tag{3}$$

where t is the film thickness, L is the satellite peak order, λ is the X-ray wavelength, and θ is the satellite angle.[23,28] This is the same equation that is used to calculate modulation wavelengths in epitaxial superlattices.[23,28] The plot of $\sin\theta_1 - \sin\theta_2$ versus $L_1 - L_2$ shown in Figure 2d gives a thickness of 28.3 ± 0.1 nm, in excellent agreement with the low-angle reflectivity data. Figure 2e shows a plot of Au thickness measured by the Laue oscillations as a function of deposition time. The Au thickness ranges from 7.7 nm for a film deposited for 5 min to 28.3 nm for a film deposited for 30 min. It is noteworthy that a 1 cm^2 electrode deposited with the thickest (28.3 nm) of these Au films contains only 54 μg of Au. Hence, the Au/Si substrate is a very inexpensive proxy for single-crystal Au. Figure 2f shows a cross-sectional transmission electron micrograph of the Au film that was deposited for 30 min followed by the deposition of a Cu_2O film. The measured film thickness for the Au was 25 ± 2 nm, in reasonable agreement with the more-accurate X-ray measurements. Also, the transmission electron microscopy (TEM) measurements did not show an interfacial SiO_x layer between the Si(111) and Au(111).

Plan-view scanning electron micrograph (SEM) images of 28 nm thick Au films grown on Si(111), Si(100), and Si(110) are shown in Figure 3. The images are consistent with the X-ray results, because the Au(111) surface is very smooth and featureless (except for 16 nm pores), whereas the Au(100) and Au(110) surfaces are rough. This explains why the Kiessig fringes and Laue oscillations are only observed for the Au(111) films on Si(111).

The Au/Si junction can have ohmic or rectifying behavior, depending on the doping type and concentration in the Si wafer. If the Si is doped to degeneracy, the Au/Si functions as an ohmic contact, whereas if the Si is n-doped to moderate doping densities, the Au/Si functions as a Schottky barrier. Figure 4a shows the ohmic response that is observed when 28 nm of Au are deposited onto n^{++}-Si(111) with a resistivity of 0.05 Ω.cm. The same behavior is observed with p^{++}-Si substrates. In both cases the Si acts like a metal because

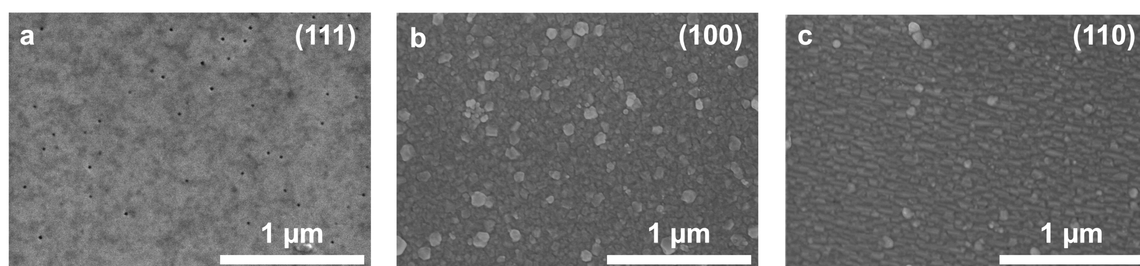

Figure 3. Surface morphology of the epitaxial Au films on Si. Plan-view SEM images of (a) Au(111), (b) Au(100), and (c) Au(110) films. The films are all approximately 28 nm thick. The Au(111) is smooth and featureless, whereas the Au(100) and Au(110) films are rough.

the Fermi level is situated either in the conduction band (n^{++}-Si) or in the valence band (p^{++}-Si) of the semiconductor. Degenerate Si substrates would be preferred if the Au/Si substrate were to be used for anodic depositions, or if precise control of the potential at the Au surface is required. As shown in Figure 4b, rectifying behavior is observed for 28 nm of Au deposited onto n-Si(111) with a resistivity of 1.15 Ω.cm. The Au/Si Schottky junction passes cathodic currents but is blocking to anodic currents. This type of junction could be used for cathodic deposition of materials, but materials requiring anodic currents for deposition would require photoassisted deposition. The interfacial energetics of the Au/Si Schottky barrier were determined by analysis of the current-voltage curves (Figure 4c) and by Mott-Schottky analysis (Figure 4d).[44] Figure 4c shows a plot of log(J) versus V in the forward bias regime. The slope of the plot gives a diode quality factor of 1.4, and the y-intercept gives a dark saturation current density of 2.5×10^{-8} A cm^{-2}, which corresponds to a barrier height of 0.85 eV. The Mott-Schottky plot of C^{-2} versus reverse bias gives the doping density in the depletion region of 3.8×10^{15} cm^{-3} from the slope of the line, and a flat-band voltage of -0.68 V from the x-intercept. This flat-band voltage corresponds to a barrier height of 0.90 eV, slightly larger than the 0.85 eV determined from the log(J) versus V plot. Mott-Schottky analysis often overestimates barrier heights, so we assume that the actual barrier height on the Au(111)/n-Si(111) is close to the 0.85 eV value determined from the forward bias current-voltage curve. It may be possible to exploit this relatively high

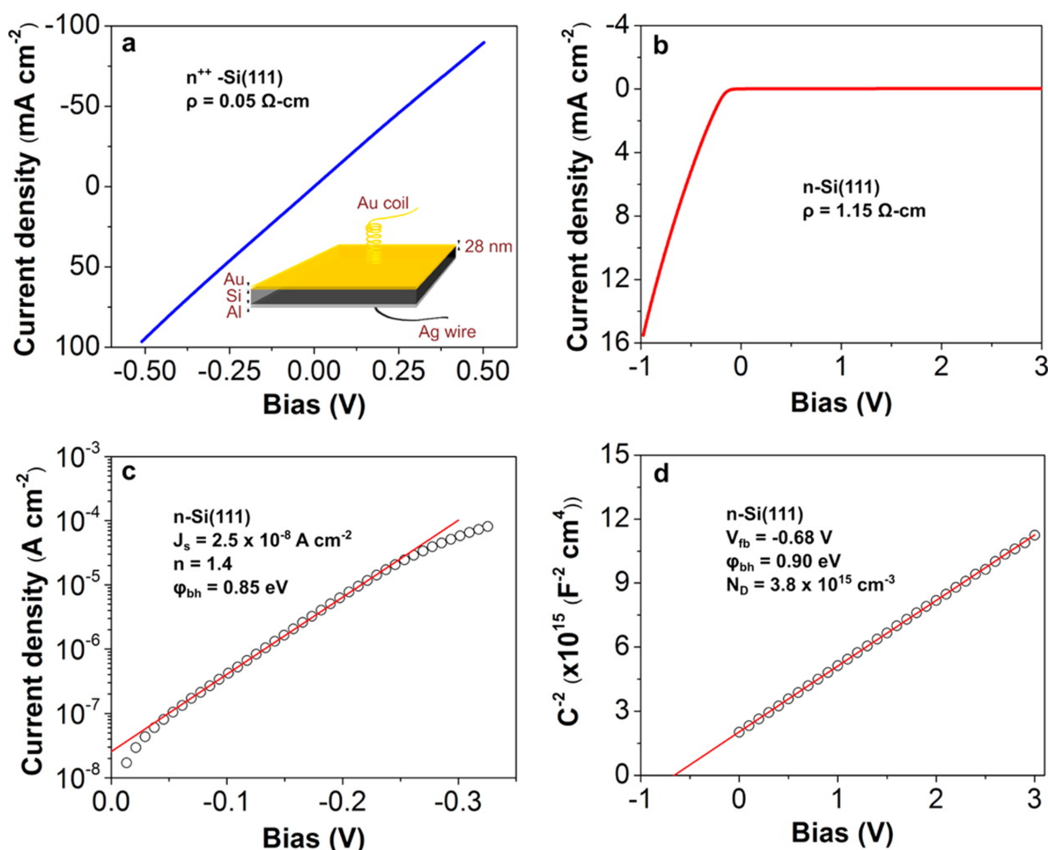

Figure 4. Junction characteristics of Au on Si(111). (a) Ohmic response of Au on n^{++}-Si(111) with a resistivity of 0.05 Ω.cm. Inset shows the schematic of measurement configuration with Au coil pressed against the Au layer as top contact and an aluminum sputtered back-contact with a silver wire. (b) Current-voltage response of Au on n-Si(111) with resistivity of 1.15 Ω.cm showing rectifying behavior. (c) Short-circuit current density, diode quality factor, and barrier height measured using log(J) versus V at forward bias for Au on n-Si(111). (d) Flat-band voltage, doping density, and barrier height measured using Mott-Schottky plot collected at 50 mV/s scan rate and 1 MHz frequency at reverse bias.

barrier height in the Au(111)/n-Si(111) epitaxial junction to produce high-photovoltage, stable photoanodes for photoelectrochemical cells.[44]

Cu_2O films were electrodeposited onto Si(111), Si(100), and Si(110) substrates covered with films of Au that were electrodeposited for 30 min. The deposition was performed from a solution containing 0.2 M $CuSO_4$, 0.2 M $C_4H_6O_6$ (tartaric acid), and 3.0 M NaOH at a constant cathodic current density of 1.0 mA cm^{-2} at 30 °C to a charge density of 0.1

C cm^{-2} (approximately 120 nm thick Cu_2O).[45] As shown in the XRD patterns in Figure 5, the Cu_2O followed the out-of-plane orientation of the Si substrates and the Au buffer layers for all three orientations of Si. Note that the log of intensity is plotted in the XRD patterns, so even minor orientations would be seen if they were present.

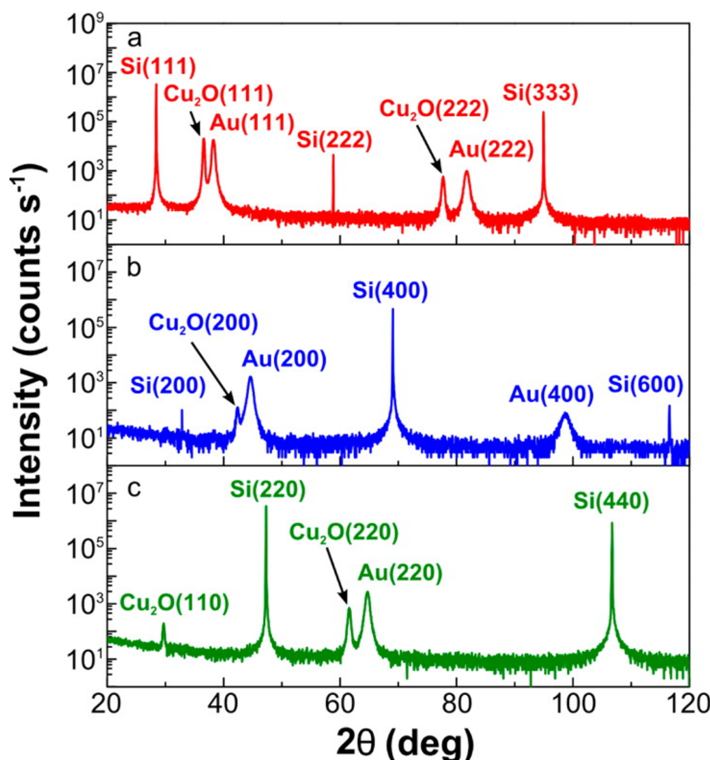

Figure 5. X-ray diffraction patterns of Cu_2O on Au on Si. Out-of-plane orientation of electrodeposited (a) Cu_2O(111) on Au(111)/Si(111), (b) Cu_2O(100) on Au(100)/Si(100), and (c) Cu_2O(110) on Au(110)/Si(110).

The out-of-plane perfection in the samples was also probed using X-ray rocking curves (Figure 6). The rocking angle, ω, is defined in Figure S1 of the Supporting Information. The rocking curves provide a direct measure of the mosaic spread (or distribution) of the films in the out-of-plane direction. The fwhm (full width at half-maximum) of the rocking curves with a Gaussian distribution is equal to $2(2 \ln 2)^{1/2}\, \alpha$, or 2.355α, where α is the standard deviation of the mosaic spread. Figure 6a shows rocking curves for Au films on Si(111) for various thicknesses of Au. It is seen that the rocking curve becomes sharper as

the Au film thickness increases, and the curves develop a shape with a broad base and sharp peak for the thicker films. In Figure 6b the 28 nm Au film on Si(111) that was deposited for 30 min is deconvoluted into two Gaussian curves with fwhm of 0.15° and 1.07°. These results show that the mosaic spread of the Au on Si(111) decreases dramatically as the film thickness increases. Figure 6c compares the Au rocking curves on Si(111), Si(100), and Si(110). The Au on all three orientations of Si was electrodeposited for 30 min. The Au rocking curves on the Si(100) and Si(110) substrates do not show the two components that were observed on Si(111). The fwhms of the Au films on Si(111), Si(100), and Si(110) were 0.15°, 2.03°, and 1.29°. Hence, the highest quality Au films are deposited on Si(111), and the quality of the film increases as the film thickness increases. Figure 6d shows rocking curves for 120 nm of Cu_2O that was deposited onto the three Au/Si orientations shown in Figure 6c. The fwhm of the Cu_2O rocking curves on Au(111)/Si(111), Au(100)/Si(100), and Au(110)/Si(110) was 1.15°, 1.84°, and 1.25°, respectively. Again, the Cu_2O with the smallest mosaic spread is observed on Au(111)/Si(111).

A high-resolution TEM micrograph is shown in Figure 7 for a 120 nm thick film of Cu_2O deposited onto a 25 nm thick Au buffer layer on miscut Si(111). The micrograph viewing direction is along the $[11\bar{2}]$ zone axis. Figure 7a is a view showing all three materials, Figure 7b is a close-up of the $Cu_2O(111)$/Au(111) interface, and Figure 7c is a close-up of the Au(111)/Si(111) interface. A fairly sharp transition is seen at both interfaces. There are also no obvious dislocations or twins in the Au buffer layer. The measured d-spacings for Au and Cu_2O are consistent with the bulk values. Most notable is the lack of an SiO_x interlayer at the Au(111)/Si(111) interface. We attribute this to the fact that the Si(111) electrode was prepolarized at -1.9 V *versus* Ag/AgCl before deposition of Au. Electron diffraction patterns of the Si and Au are shown in Figure S2 of the Supporting Information.

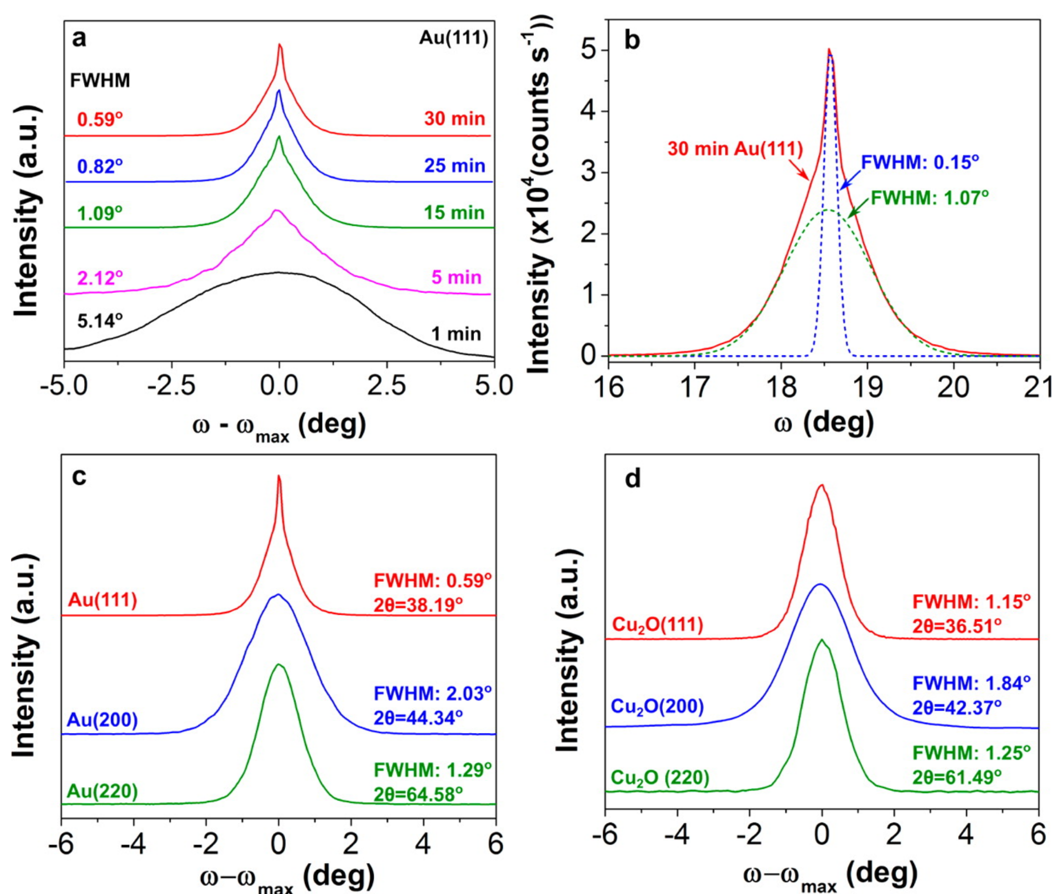

Figure 6. X-ray rocking curves of Au and Cu_2O on Si measure out-of-plane mosaic spread. (a) Rocking curves of Au on Si(111) as a function of deposition time. (b) Rocking curve of 30 min Au on Si(111) deconvoluted into two Gaussian fits showing a mosaic spread of 0.15° and 1.07°. (c) Rocking curves of Au(111) on Si with fwhm of 0.59°, Au(100) with 2.03°, and Au(110) with 1.29°. (d) Rocking curves of Cu_2O on Au/Si(111) with fwhm of 1.15°, Cu_2O(100) with 1.84°, and Cu_2O(110) with 1.25°.

The out-of-plane and in-plane orientations of the Au buffer layer and Cu_2O film can be determined by X-ray pole figures. Because X-rays penetrate through the Au and Cu_2O layers and into the Si substrate, the pole figures can be used to determine the epitaxial relationships of the film and buffer layer with respect to the Si substrate. In a pole figure, planes other than those parallel with the substrate surface are probed by selecting the Bragg angle, θ, for the plane of interest and then tilting the sample through a series of tilt angles, χ, from 0° to 90° and rotating the sample through a series of azimuthal angles, φ, from 0° to 360°. The measurement geometry for the pole figures is shown in Figure S1 of the Supporting

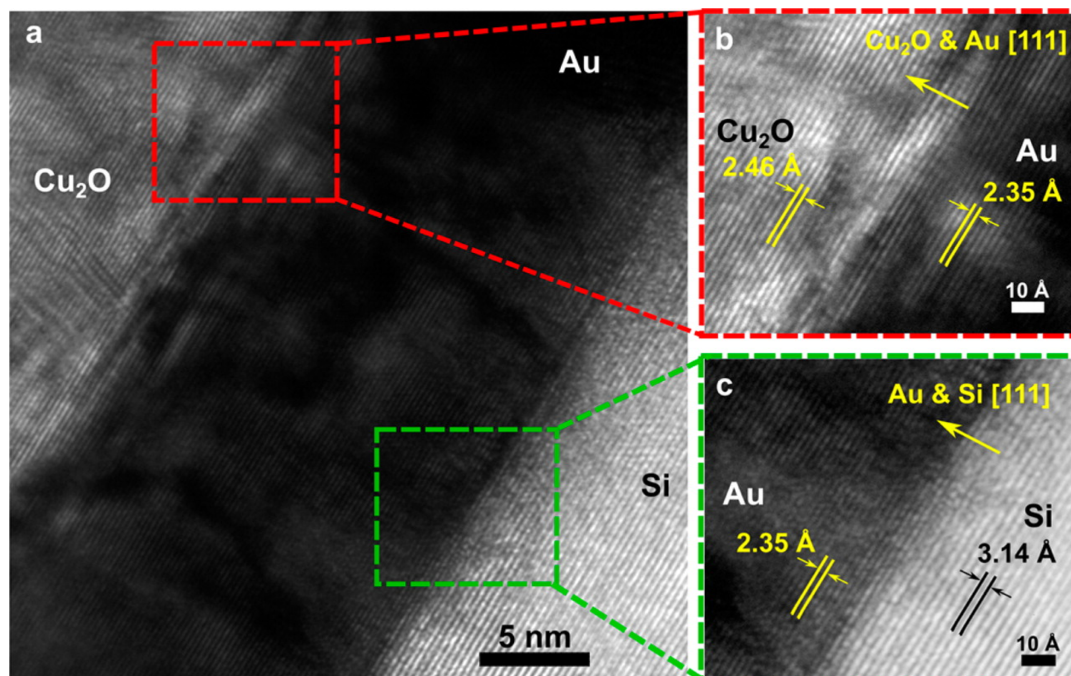

Figure 7. High-resolution cross-sectional TEM of $Cu_2O(111)$ and Au(111) on Si(111). (a) TEM cross-section of $Cu_2O(111)$/Au(111)/Si(111) layers. (b) Cu_2O and Au high-resolution TEM image with lattice spacings in agreement with bulk values and [111] growth direction. (c) Au and Si high-resolution TEM with lattice spacing in agreement with bulk values and no noticeable SiO_x interlayer.

Information. For films with in-plane order, peaks occur in the pole figure when the Bragg condition is satisfied, whereas for textured films with no in-plane order, rings are observed in the pole figure. X-ray pole figures of Si(111), Si(100), and Si(110) substrates with a 28 nm buffer layer of Au and a 120 nm film of Cu_2O are shown in Figure 8. In Figure 8a-c the (220) poles of Si(111), Au(111), and $Cu_2O(111)$ are probed. The assignment of peaks in the pole figures was achieved by comparing the pole figures to calculated stereographic projections that are shown in Figure S3 of the Supporting Information. The Si pole figure in Figure 8a shows the expected three spots separated azimuthally by 120° at a tilt angle of 35.5°, consistent with the angle between the [111] and [220] directions in a cubic system. The (220) pole figures of the Au buffer layer and Cu_2O films shown in Figure 8b,c also show spots at the expected tilt angle of 35.5°; however, there are now six spots that are

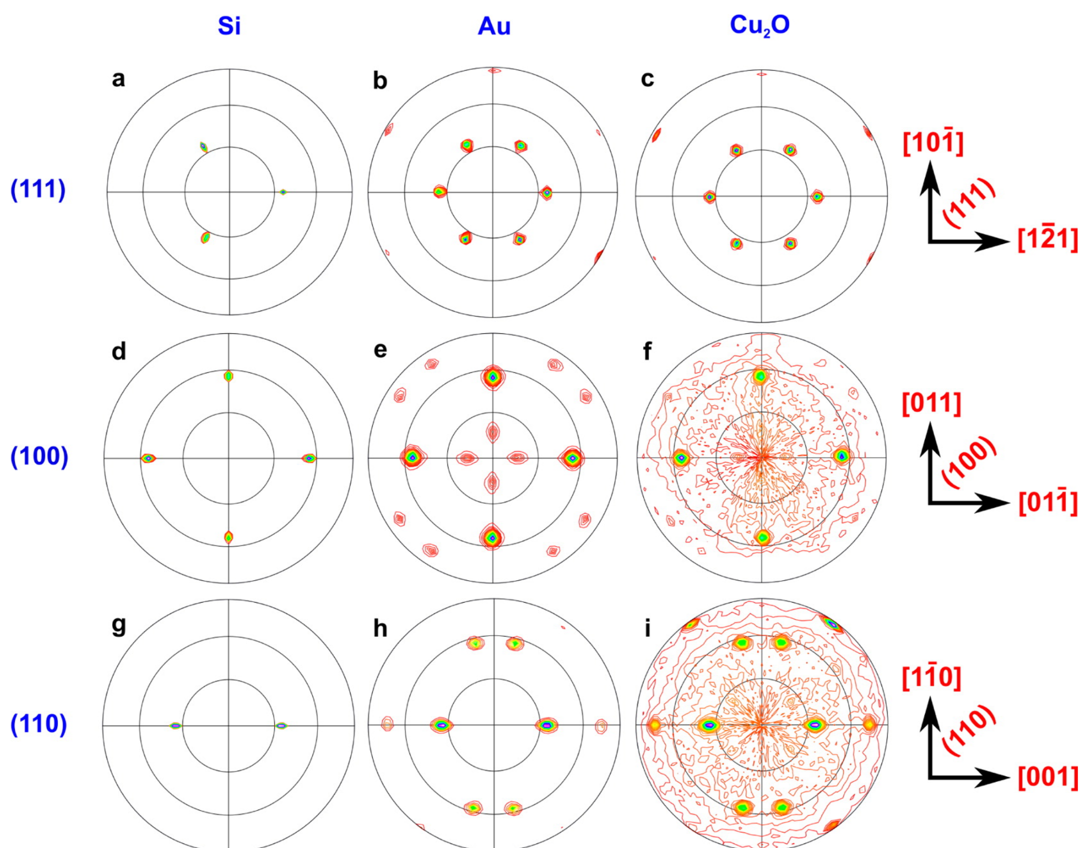

Figure 8. In-plane orientation of Au and Cu_2O on Si from X-ray pole figures. (a-c) (220) pole figures of Si(111), Au(111), and Cu_2O(111). (d-f) (111) pole figures of Si(100), Au(100), and Cu_2O(100) and (g-i) (111) pole figures of Si(110), Au(110, and Cu_2O(110). The radial grid lines in the pole figures represent 30° increments of the tilt angle.

separated azimuthally by 60°. These (220) pole figures show that the Si, Au, and Cu_2O all have a [111] out-of-plane orientation and that the Au and Cu_2O are aligned in-plane both parallel and antiparallel with the Si substrate. The parallel and antiparallel in-plane orientations can also be described as rotation twins. Azimuthal and tilt scans of Cu_2O(111) on Au(111)/Si(111) are shown in Figure S4 of the Supporting Information. Epitaxial relationships consistent with these pole figures are $Cu_2O(111)[10\bar{1}]\|Au(111)[10\bar{1}]\|Si(111)[10\bar{1}]$ and $Cu_2O(111)[10\bar{1}]\|Au(111)[10\bar{1}]\|Si(111)[\bar{1}01]$. In Figure 8d-f the (111) poles of Si(100) Au(100), and Cu_2O(100) are probed. All three pole figures show four spots separated azimuthally by 90° at a tilt angle of 54.0° consistent with the 54.74° tilt between the [111] and

[100] directions in a cubic system. The epitaxial relationship based on the major spots in the pole figures is $Cu_2O(100)[011]||Au(100)[011]||Si(100)[011]$. In addition to the major spots at the expected tilt angle, however, there are also four spots at a tilt angle of 15.65° and eight spots at a tilt angle of 78.0°. These additional spots are due to reflection twins with a [221] orientation.[21,46] That is, the [221] direction of the twinned crystallite is parallel to the [100] direction of the original crystallite. The (221) reflection is not observed in the 2θ plot in Figure 1b, because mixed-index reflections (i.e., even-even-odd) are systematically absent in an fcc structure. The higher-order (442) reflection should be observed, but it would occur at a 2θ value that exceeds our instrumental capability. Hence, the pole figure on the Si(100) sample shows the epitaxial relationship and it shows that the sample is twinned. A similar result is seen on Si(110). In Figure 8g-i the (111) poles of Si(110) Au(110), and $Cu_2O(110)$ are probed. All three pole figures show two spots separated azimuthally by 180° at a tilt angle of 34.5°, consistent with the expected 35.26° tilt between the [111] and [110] directions in a cubic system. The epitaxial relationship based on the major spots in the pole figures is $Cu_2O(110)[001]||Au(110)[001]||Si(110)[001]$. In addition to the major spots at the expected tilt angle, however, there are also four spots at a tilt angle of 57.0° and two spots at a tilt angle of 75.0°. These additional spots are due to reflection twins with a [411] orientation.(21, 46) That is, the [411] direction of the twinned crystallite is parallel to the [110] direction of the original crystallite. The (411) reflection is also not observed in the 2θ plot in Figure 1c, because it is a mixed-index reflection. Hence, the pole figures show that the Au buffer layers and Cu_2O films follow the out-of-plane and in-plane orientations of the Si(111), Si(100), and Si(110) substrates. In addition, the pole figures show that reflection twinning occurs in the samples on the Si(100) and Si(110) substrates but not on the Si(111) substrate. Reflection twinning on the Si(111) substrate would produce a [511] orientation,(21, 46) which is not observed in the pole figures.

At this point, it is instructive to review the twinning relationships in a cubic system. Additional details on the twinning transformation matrices are provided in the Supporting Information. Twinning can be described by the matrix, T(hkl), by the relationship

$$(PQR) = T_{(hkl)}(pqr) \tag{4}$$

where (PQR) is a column matrix for the lattice plane in a twinned crystallite that corresponds to the lattice plane, (pqr), of the original crystallite after twinning on (hkl). The general twin matrix for cubic systems is

$$T_{(hkl)} = \left(\frac{1}{h^2+k^2+l^2}\right)\begin{pmatrix} h^2-k^2-l^2 & 2hk & 2hl \\ 2hk & -h^2+k^2-l^2 & 2kl \\ 2hl & 2kl & -h^2-k^2+l^2 \end{pmatrix} \tag{5}$$

In face-centered-cubic (fcc) crystal structures, twinning occurs on 111 slip planes, and the twinning matrix becomes

$$T_{(111)} = \left(\frac{1}{3}\right)\begin{pmatrix} -1 & 2 & 2 \\ 2 & -1 & 2 \\ 2 & 2 & -1 \end{pmatrix} \tag{6}$$

Hence, by using the twin matrix in eq 6 and solving eq 4, the twinning relationships shown in eqs 7-9 result.

$$(pqr) = (300);\ (PQR) = (\bar{1}22) \tag{7}$$

$$(pqr) = (330);\ (PQR) = (114) \tag{8}$$

$$(pqr) = (\bar{3}33);\ (PQR) = (5\bar{1}\bar{1}) \tag{9}$$

The pole figures in Figure 8 show that reflection twinning of Au occurs on the Si(100) and Si(110) substrates, but not on the Si(111) substrate. The pole figures also show that this twinning on Au(100) and Au(110) is transferred to the Cu_2O films on these buffer layers. This is especially obvious in the pole figure in Figure 8i for the Cu_2O films deposited on Au(110) on Si(110). Hence, the twin orientation is present at the surface of the twinned Au films. There is not a simple explanation for why reflection twinning does not occur on the [111]-oriented substrate, whereas it does occur on the [100]- and [110]-oriented substrates, because the Au/Si lattice mismatch is the same on all three substrates. One possible explanation is that the [111] direction is both the thermodynamically and kinetically preferred growth direction for Au, because the (111) planes are the close-packed planes. This [111] orientation will develop even on polycrystalline or amorphous substrates. Hence, the Au films on the [100] and [110] substrates may be twinning as they slowly evolve into [111]-oriented films. As shown in the Supporting Information (Figure S5), a thick (ca. 5 μm) film of Au electrodeposited onto [110]-oriented Si does eventually develop a [111] orientation, consistent with this hypothesis.

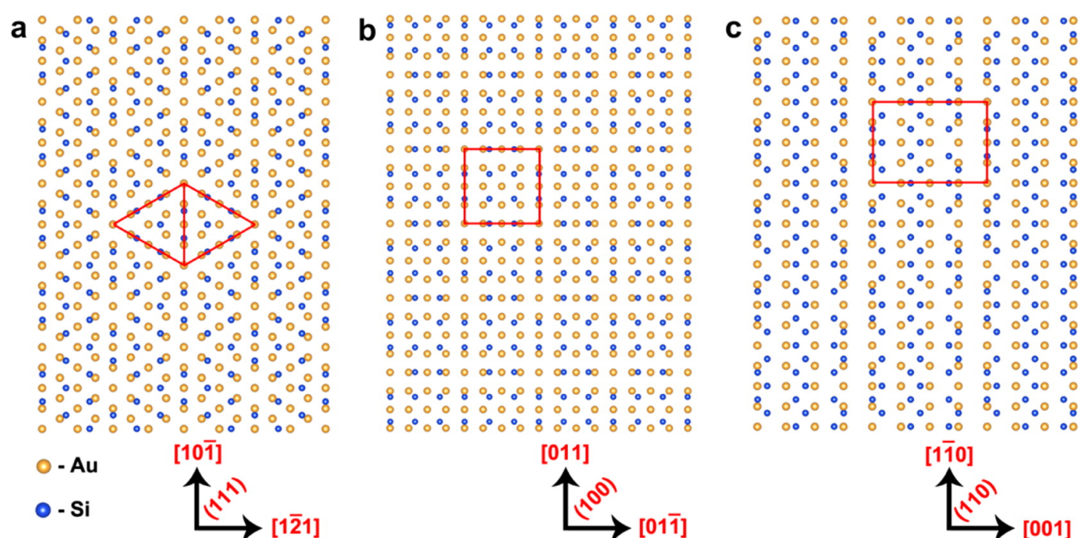

Figure 9. Interface models of Au on Si. (a) Au(111) on Si(111), (b) Au(100) on Si(100,) and (c) Au(110) on Si(110) Moir*é* patterns result from 4 unit meshes of Au coinciding with 3 unit meshes of Si with a coincidence site lattice mismatch of +0.13%.

The Cu_2O/Au/Si system is an interesting example of epitaxy. In this epitaxial system, Cu_2O with lattice parameter 0.42696 nm and primitive space group $Pn\bar{3}m$ is deposited onto Au with lattice parameter 0.40786 nm and fcc space group $Fm\bar{3}m$, which is deposited onto Si with lattice parameter 0.54309 nm and diamond cubic space group $Fd\bar{3}m$. The lattice mismatch $((d_{film} - d_{substrate})/d_{substrate})$ between Cu_2O and Au is +4.7%, and the lattice mismatch between Au and Si is -24.9%. Because all of the materials have cubic structures and the Au and Cu_2O on a given Si substrate both have the same out-of-plane orientation as the substrate, the lattice mismatch is independent of the Si orientation. The +4.7% mismatch in the Cu_2O/Au system is reasonable, and would be expected to produce a Cu_2O layer with moderate compressive in-plane strain and tensile out-of-plane strain. Interface models for the Cu_2O/Au interfaces for the three orientations are shown in Figure S6 of the Supporting Information. The -24.9% mismatch in the Au/Si system is too excessive, however, to produce a simple 1x1 epitaxial system. The epitaxy in the Au/Si system can be explained by the formation of coincident site lattices (CSLs) in which 4 unit meshes of Au coincide with 3 unit meshes of Si. These CSLs are shown in Figure 9, in which the surface Si atoms are blue and the Au atoms are gold. The out-of-plane and in-plane directions in these CSLs were directly measured from the pole figures in Figure 8. The CSLs produce Moir patterns on each of the Si surfaces. The lattice mismatch (i.e., $(4d_{Au(hkl)} - 3d_{Si(hkl)})/3d_{Si(hkl)}$) in the CSLs on all three Si orientations is reduced from -24.9% for the $1d_{Au(hkl)}$ x $1d_{Si(hkl)}$ lattice to +0.13% for the $4d_{Au(hkl)}$ x $3d_{Si(hkl)}$ CSL. In these CSLs the Au film would have very small compressive in-plane and tensile out-of-plane strains. Note that this same CSL was observed by Sayed et al. for epitaxial Au on Si produced by galvanic displacement[37] and by Li and Zuo for epitaxial Ag on Si produced by electron beam evaporation.[47]

In agreement with the CSL discussed above for Au on Si, the out-of-plane d-spacing as measured by XRD for very thin layers of Au on Si is greater than the bulk value of Au. Figure 10 shows the measured d_{111} for Au as a function of Au deposition time. The blue

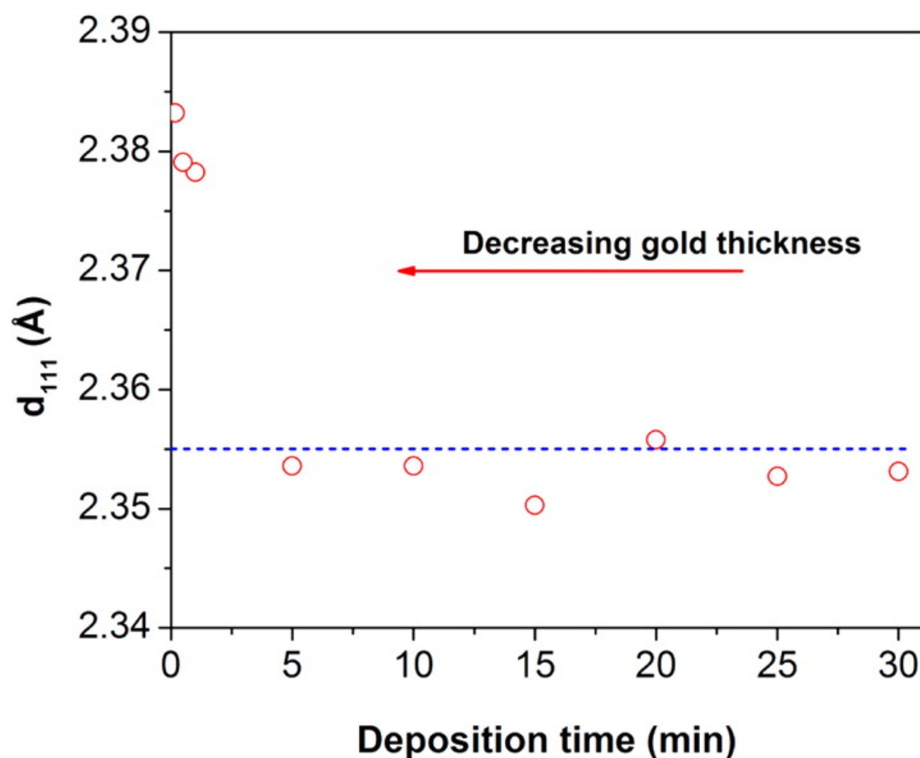

Figure 10. Evidence for out-of-plane tensile strain in ultrathin Au(111) films on Si(111). Out-of-plane d_{111} spacing measured for Au(111) on Si(111) deposit as a function of deposition time showing out-of-plane tensile strain for short deposition times. The blue horizontal dashed line corresponds to d_{111} for bulk Au

horizontal dashed line in Figure 10 corresponds to the d_{111} for bulk Au. For deposition times from 5 to 30 min, the measured out-of-plane d-spacing agrees well with the bulk value. The thickness of Au varies from 7.7 to 28.6 nm in this range (see Figure 2). For deposition times shorter than 5 min we were not able to measure the film thickness, because the Au had not coalesced into a smooth film. At these shorter times the d_{111} is larger than the bulk value, consistent with compressive in-plane and tensile out-of-plane strains. This is also consistent with the CSL. If the mismatch were -24.9% as for a $1d_{Au(111)}$ x $1d_{Si(111)}$, the in-plane strain would be tensile and the out-of-plane strain would be compressive.

3. CONCLUSIONS

We show that nanometer-thick electrodeposited epitaxial layers of Au on Si(111), Si(100), and Si(110) can serve as a platform for the electrodeposition of epitaxial thin films of Cu_2O. We exploit the fact that Si wafers with a high degree of perfection and well-defined orientation are both readily available and inexpensive. The highly ordered Au/Si substrates cost a small fraction of the cost of bulk Au single crystals because of the low mass of Au that is used, they can conceivably be made as large as a Si wafer, and they may allow for the integration of electrodeposited functional ceramics with traditional semiconductor devices. A 28.3 nm thick film of Au on a 1 cm^2 substrate contains only 54 μg of Au. Films of Au deposited onto degenerate Si produce ohmic contacts, whereas films deposited onto moderately doped n-type Si(111) produce a rectifying contact with a barrier height of 0.85 eV.

We use the method that Allongue and co-workers developed to deposit ultrathin Au films onto miscut Si(111).[38,39] The deposition is done at room temperature in a solution containing 0.1 mM $HAuCl_4$, 1 mM KCl, 1 mM H_2SO_4, and 0.1 M K_2SO_4 using a Si electrode that is prepolarized at -1.9 V *versus* Ag/AgCl before inserting it in the deposition solution. The prepolarization of the Si prevents the formation of an amorphous layer of SiO_x on the Si surface, as shown by cross-sectional TEM. The highest quality Au films are deposited onto Si(111). They are smooth enough to allow for thickness measurement by low-angle X-ray reflectivity and Laue oscillations, they are free of reflection twins, and they have an out-of-plane mosaic spread as low as 0.15°.

The Au/Si interface is an interesting example of epitaxy, because high-quality, smooth Au epitaxial films are produced even though there is a -24.9% lattice mismatch between the Au film and Si substrate. The epitaxy in the Au/Si system can be explained by the formation of coincident site lattices (CSLs) in which 4 unit meshes of Au coincide with

3 unit meshes of Si. The lattice mismatch in the CSLs on all three Si orientations is reduced from -24.9% for the 1$d_{Au(hkl)}$ x 1$d_{Si(hkl)}$ lattice to +0.13% for the 4$d_{Au(hkl)}$ x 3$d_{Si(hkl)}$ CSL.

Epitaxial Cu_2O is deposited onto the Au/Si substrates by cathodic electrodeposition from an alkaline tartrate bath. The Cu_2O follows the out-of-plane and in-plane orientations of the Si substrates and Au buffer layers, as determined by X-ray pole figures. The Au and Cu_2O films deposited on Si(100) and Si(110) are both twinned. The films grown on Si(100) have reflection twins with a [221] orientation, and the films grown on Si(110) have reflection twins with a [411] orientation. The method we have outlined for the deposition of epitaxial Cu_2O on Au/Si should be applicable to a very wide range of semiconductor and ceramic materials. It is especially well suited for applications that require a conducting back-contact (e.g., solar cells) or require integration with single-crystal Si (e.g., solid-state memory).

4. MATERIALS AND METHODS

4.1. Si Wafers and Etching Procedures. Si wafers with [111], [100], and [110] orientations were used to study epitaxial Au and Cu_2O electrodeposition. Phosphorus doped single-side polished n-Si(111) was miscut 0.2° toward [11$\bar{2}$] with resistivity of 1.15 Ω.cm. Phosphorus doped n^{++}-Si(100) with a resistivity of 0.001 Ω.cm and boron doped p^{++}-Si(110) with a resistivity less than 0.005 Ω.cm was used for the study of epitaxy. All wafers were obtained from Virginia Semiconductor Inc. Aluminum was sputtered on the back of Si wafers to form an ohmic contact, and silver wire with silver paste (GC electronics, silver print II) was used to make the back-contact for all orientations. Either silicone paste or nail polish was used as an insulating and inert layer on the back of Si to prevent contact in the electrolyte during electrodeposition. All wafers prior to use were etched in 5% hydrofluoric acid solution for 30 s to dissolve the native oxide, then soaked in hot

DI water (ca. 80-90 °C) for 15 min to passivate the surface with a SiO_x layer, and then etched again with 5% hydrofluoric acid for 30 s and buffered hydrofluoric acid for 30 s to produce a hydrogen-terminated surface. Ethanol was used to clean any organic residue, and the sample was rinsed with DI water prior to deposition. All depositions were performed immediately after the etching process to avoid any surface passivation.

4.2. Electrodeposition of Au and Cu_2O Films. Electrodeposition of Au and Cu_2O Films Au was electrodeposited from a plating solution containing 0.1 mM $HAuCl_4$, 1 mM KCl, 1 mM H_2SO_4, and 100 mM K_2SO_4 in deionized water. The solution was prepared by adding 10 mL of a stock solution containing 1 mM $HAuCl_4$, 10 mM KCl, and 10 mM H_2SO_4 to 90 mL of DI water. Lastly, 100 mM K_2SO_4 was added as a supporting electrolyte to produce a final solution with a pH of about 3. A -1.9 V *versus* Ag/AgCl prepolarized bias was applied at ambient temperatures with 200 rpm stirring. All depositions used an Ag/AgCl reference electrode and an Au coil as a high surface area counter electrode. The requisite step during deposition was the prepolarization of the Si electrode prior to immersion in the electrolyte to avoid native oxide formation and also to prevent deposition of Au on Si by galvanic displacement. After the deposition, films were rinsed with DI water and dried in air. Cu_2O was electrodeposited from a plating solution containing 0.2 M $CuSO_4$, 0.2 M $C_4H_6O_6$ (tartaric acid), and 3.0 M NaOH. A cathodic current density of 1.0 mA cm^{-2} was passed for 100 s at a temperature of 30 °C and a stir rate of 200 rpm. Cu_2O films on all orientations were deposited to a charge density of 0.1 C cm^{-2}. Electrodeposition of Au and Cu_2O films was done using either an EGG Model 273A or an Autolab 30 potentiostat/galvanostat.

4.3. X-ray Diffraction Measurements and Interface Models. All XRD measurements were made with a Philips X'Pert Materials Research diffractometer with Cu K_{α_1} radiation source (λ = 1.54056). All $2\theta - \omega$ (out-of-plane orientation) scans were done

using a two-bounce hybrid monochromator with a Ge 220 monochromator and Ni 0.125 mm automatic beam attenuator and a 0.18° parallel plate collimator diffracted optics. Pole figures were measured using a crossed slit collimator with 2 mm divergence slit and 2 mm mask with a Ni filter and a 0.27° parallel plate collimator. Rocking curves (ω scans) were measured using the hybrid monochromator incident optics and a triple axis diffracted optics. X-ray reflectivity scans were measured using an X-ray mirror Cu module with Ni 0.125 mm beam attenuator and a 0.18° parallel plate collimator. Lattice constants for interface models and X-ray measurements were obtained from JCPDS card no. 027-1402 for Si, no. 004-0784 for Au, and no. 005-0667 for Cu_2O. All the interface models for Au on Si and Cu_2O on Au were made in VESTA (visualization for electronic and structural analysis) software ver. 3.3.2.

4.4. SEM Measurements. Plan-view SEM images were obtained at 5 kV using a Helios NanoLab 600 DualBeam instrument for the Au(111) film and at 15 kV on an Hitachi S4700 instrument for the Au(100) and Au(110) films.

4.5. TEM Measurements. Focused ion-beam milling for TEM sample preparation was done using the Helios NanoLab 600 DualBeam. Prior to focused ion-beam milling, the films were sputtered with a thin AuPd layer to protect the Au and Cu_2O films during the milling process and to provide a contrast difference to determine the thickness of films accurately. High-resolution TEM images and electron diffraction patterns for individual layers were measured using the Tecnai F20 transmission electron microscope.

4.6. Measurement of Interfacial Energetics. All J-V and Mott-Schottky curves were measured using a PARSTAT 2273 potentiostat/galvanostat with Au coil as top contact (schematic shown in the inset of Figure 3a), and Mott-Schottky scans were collected at a 50 mV/s scan rate and 1 MHz modulation frequency.

SUPPORTING INFORMATION

X-ray Measurement Geometry Showing θ, ω, ϕ, χ Angles. X-ray rocking curves, azimuthal scans and pole figures are texture analysis tools for highly ordered crystalline materials. All of these scans require 2θ angle fixed at the peak of interest. For example, 2θ = 47.304° for probing the Si(220) plane(s). The sample stage is tilted or rotated in different directions and angles in order to determine the in-plane and out-of-plane order of the sample. As shown in Figure S1, rocking the sample along the axis perpendicular to the source-sample-detector plane is known as the ω scan or rocking curve. Rocking curves determine the mosaic spread of the out-of-plane orientation. Rotation of the sample around the sample normal is the ϕ scan, or the azimuthal scan. Tilting the sample along the axis orthogonal to both the ω and the ϕ axes is the χ scan (or sometimes referred to as the Ψ scan). Diffraction signals collected from the azimuthal scans (ϕ = 0° to 360°) at each tilt angle (χ = 0° to 90°) can be used to construct a pole figure.

Stereographic Projections of Si, Au and Cu_2O. The out-of-plane and in-plane orientations of films relative to substrates can be determined from X-ray pole figures. Stereographic projections display the expected peak positions in each X-ray pole figure pattern. The stereographic projections shown in Figure S3 were simulated using CaRine software. Figure S3-a is the stereographic projection of Si(220) poles on the Cu_2O/Au/Si(111) sample. Because of the three-fold symmetry around the [111] direction, three spots (ϕ = 120°

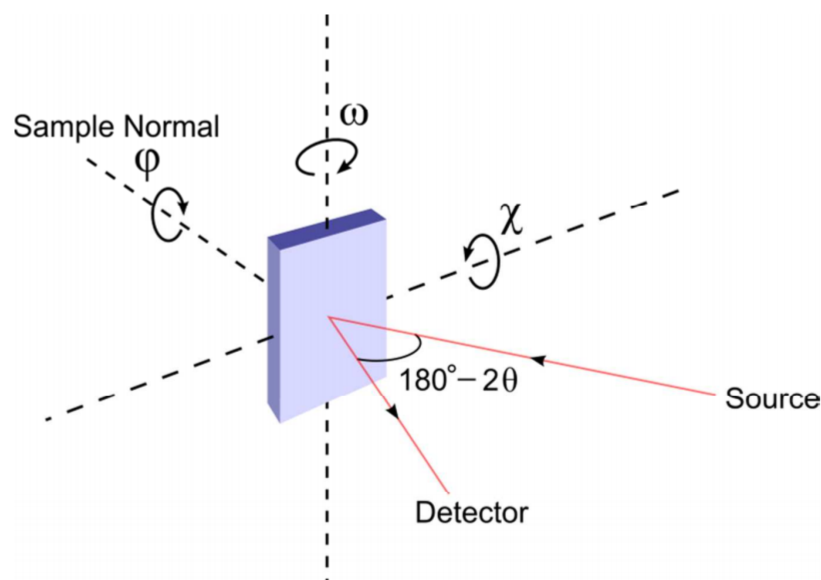

Figure S1. X-ray measurement geometry showing θ, ω, ϕ, χ angles

apart) are expected and shown as the closed circles in Figure S3-a. The tilt angle of these three spots is χ = 35.26°, which is the angle between [111] and [110]. Due to the narrow diffraction peaks of the Si substrates, the peaks at χ = 90° are usually not observed. Figure S3-b represents the stereographic projection for the domain that is antiparallel to the domain in Figure S3-a. The antiparallel domain is only seen in the electrodeposited Au and Cu_2O layers. Notice that the pattern of the antiparallel domain (shown as open circles) is rotated 180° with respect to the pattern of the parallel domain. When both domains are present in a sample, the resulting stereographic projection becomes the combination of both, as shown in Figure S3-c. The closed circles enclosed by the open circles represent the overlapping pattern between parallel and antiparallel domains. Figure S3-d shows the simulated Si(111) poles on the Cu_2O/Au/Si(100) sample. The 4-fold symmetry along the [100] out-of-plane direction results in 4 spots separated at ϕ = 90°. The tilt angle of χ = 54.74° originates from the angle between [100] and [111]. The (111) poles of Au and Cu_2O are at identical positions as the Si(111) poles of the same sample. The red triangles in Figure S3-e are also the Au(111) or Cu_2O(111) poles, but their out-of-plane direction is [221], which is

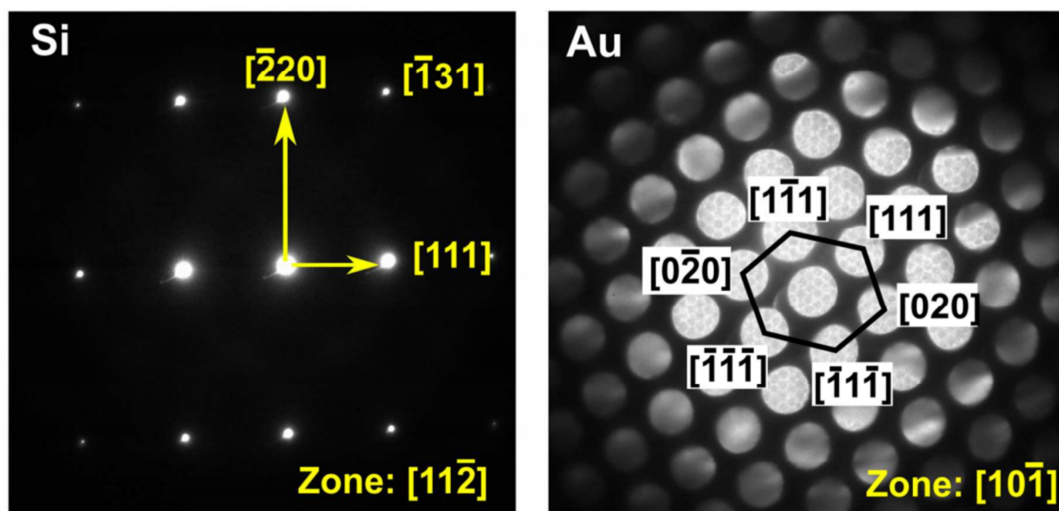

Figure S2. Electron diffraction patterns of Si and Au. Electron diffraction patterns of Si along zone axis $[11\bar{2}]$ and Au along zone axis $[10\bar{1}]$ showing spot pattern. Convergent beam diffraction was performed for Au because of lower thickness of the film (ca. 30 nm).

the twin of [300]. The triangles at different tilt angles are attributed to different angles between different directions. The tilt angle from [221] to [111] is 15.79°, to [111] is 54.74°, and to [111] and [111] is 78.90°. Rotating the pattern of this twin 4-fold around the [221] direction results in the pattern (open triangles) shown in Figure S3-f. Figure S3-g represents the simulated Si(111) poles on the Cu_2O/Au/Si(110) sample. Two spots at χ = 35.26° are due to the angle between [110] and [111], and the 2-fold symmetry around the [110] pole results in ϕ = 180° separation of the spots. The same pattern is observed in Au(111) and Cu_2O(111) stereographic projections of the same sample. The [330] has a twin of [411]. The stars in Figure S3-h represent a set of the (111) poles from the twin. The tilt angle from [411] to [111] is 35.26°, to [111] and [111] is 57.02° and to [111] is 74.21°. The 2-fold rotation symmetry around the [411] direction results in the other set of (111) poles, represented as the open stars in Figure S3-i.

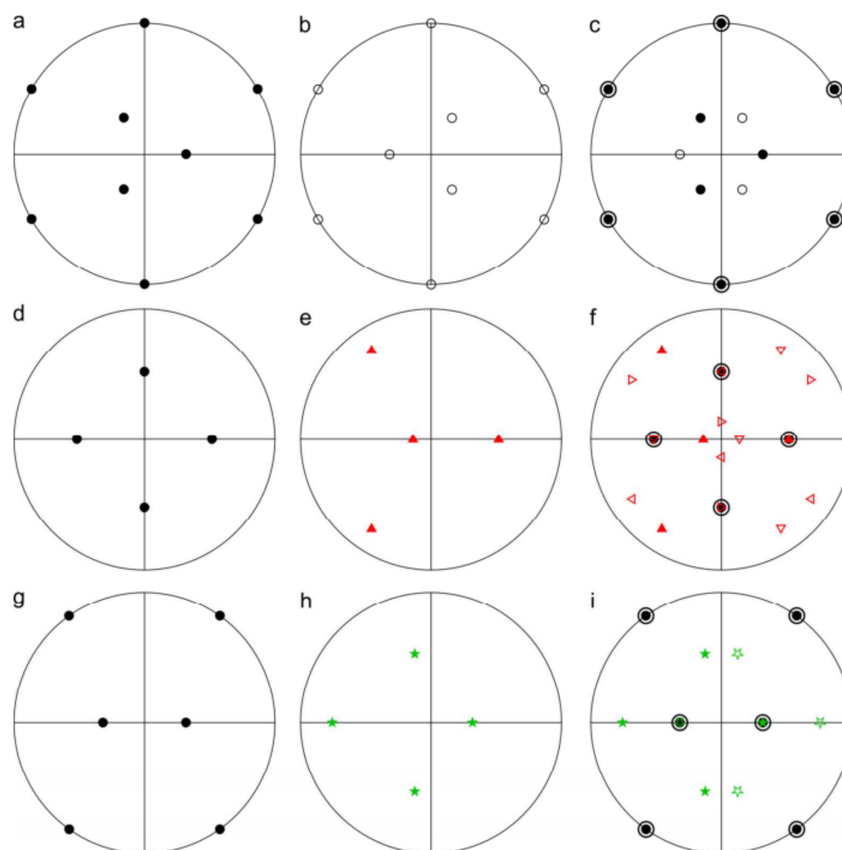

Figure S3. Stereographic projections of (a-c) (220) poles on the Cu_2O/Au/Si(111) sample, (d-f) (111) poles on the Cu_2O/Au/Si(100) sample, and (g-i) (111) poles on the Cu_2O/Au/Si(110) sample. The patterns from the parallel domains are shown as closed circles whereas the patterns from the antiparallel domains are shown as open circles. For the [111] out-of-plane sample, the (220) poles of Cu_2O, Au and Si all exhibit the same pattern as in (a). However, the deposited Cu_2O and Au have antiparallel domains whose pattern is shown in (b). The resulting pattern is the combination of both (a) and (b), which is shown in (c). For the [100] out-of-plane sample, the (111) poles of Cu_2O, Au and Si all have the same pattern as in (d). Cu_2O and Au films on the Si(100) substrate have twins whose out-of-plane is [221]. One set of the (111) poles of the twin is shown in (e). Rotating the pattern in (e) 4-fold around the out-of-plane direction results in the pattern in (f), where the circles are from the parallel and antiparallel (100) domains, and the triangles are from the twin (221) domains. For the [110] out-of-plane sample, the (111) poles of Cu_2O, Au and Si all have the same pattern as in (g). The twins in Cu_2O and Au layers are [411] out-of-plane, and one set of their (111) poles are shown as stars in (h). Because of the 2-fold symmetry around the out-of-plane direction, the overall patterns for Cu_2O and Au layers are presented in (i), where the circles are from the parallel and antiparallel (110) domains, and the stars are from the twin (411) domains.

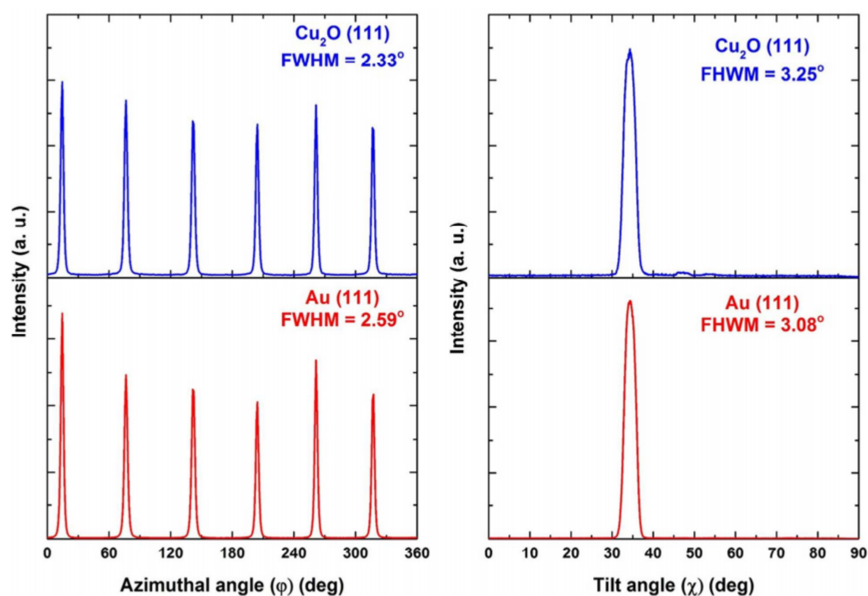

Figure S4. Azimuthal and tilt scans of Cu_2O and Au on Si(111). (a) Azimuthal scan (ϕ-scans) of Au on Si(111) (red) and Cu_2O on Au/Si(111) (blue) was performed for 0 to 360° ϕ at a tilt angle of 35.3°. FWHM of Au on Si(111) is 2.59° and Cu_2O on Au/Si(111) is 2.33°. (b) Tilt scans (χ-scans) of Au on Si(111) (red) with a FWHM of 3.08° and Cu_2O on Au/Si(111) (blue) with a FWHM of 3.25° was performed for 0 to 90° χ.

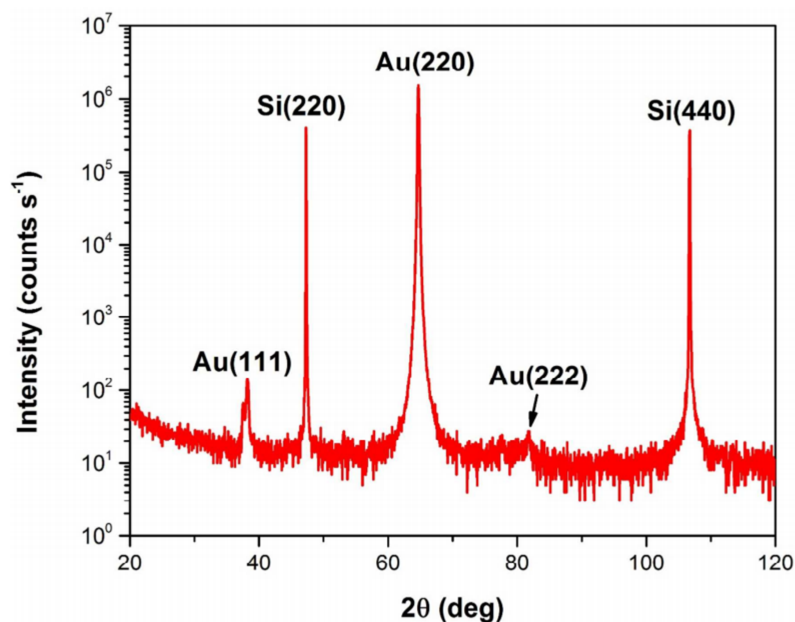

Figure S5. X-ray diffraction pattern of thick Au on Si. Out-of-plane orientation of thick (ca. 5 μm) Au on Si(110). A strong epitaxial Au[110] orientation is observed with minor Au[111] orientation.

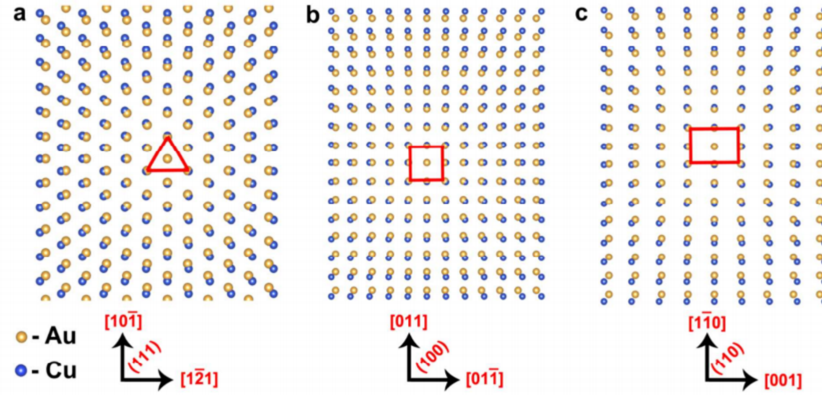

Figure S6. Interface models of Cu_2O on Au. Interface models of Cu atoms of Cu_2O (blue colored) overlay on Au atoms (gold colored) for (a) $Cu_2O(111)/Au(111)$, (b) $Cu_2O(100)/Au(100)$ and (c) $Cu_2O(110)/Au(110)$ orientations. A lattice mismatch of +4.7% is observed for 1x1 unit mesh of Cu_2O on Au for all orientation.

Transformation Matrices for Twinning in Face-Centered Cubic Systems. Twinning can be described by the matrix, $T_{(hkl)}$, by the relationship

$$(PQR) = T_{(hkl)}(pqr) \tag{10}$$

where (PQR) is a column matrix for the lattice plane in a twinned crystallite that corresponds to the lattice plane, (pqr), of the original crystallite after twinning on (hkl). The indices of reciprocal lattice point (PQR) for the twinned crystal will be related to the point (pqr) in the reciprocal lattice of original crystal after twinning on (hkl) plane by the following general expression:

$$P = \frac{p(h^2 - k^2 - l^2) + q(2hk) + r(2hl)}{(h^2 + k^2 + l^2)}$$

$$Q = \frac{p(2hk) + q(-h^2 + k^2 - l^2) + r(2kl)}{(h^2 + k^2 + l^2)}$$

$$R = \frac{p(2hl) + q(2kl) + r(-h^2 - k^2 + l^2)}{(h^2 + k^2 + l^2)}$$

In the matrix form (PQR) = $T_{(hkl)}$ (pqr) can be represented as a general twin matrix

$$T_{(hkl)} = \left(\frac{1}{h^2 + k^2 + l^2}\right) \begin{pmatrix} h^2 - k^2 - l^2 & 2hk & 2hl \\ 2hk & -h^2 + k^2 - l^2 & 2kl \\ 2hl & 2kl & -h^2 - k^2 + l^2 \end{pmatrix} \quad (11)$$

In face-centered cubic crystal structures, twinning occurs on {111} slip planes, and the twinning matrix becomes,

$$T_{(111)} = \left(\frac{1}{3}\right) \begin{pmatrix} -1 & 2 & 2 \\ 2 & -1 & 2 \\ 2 & 2 & -1 \end{pmatrix} \quad (12)$$

Twin plane for Au on Si(100):

(pqr) = (300) and (hkl) = (111)

$$\begin{pmatrix} P \\ Q \\ R \end{pmatrix} = \left(\frac{1}{3}\right) \begin{pmatrix} -1 & 2 & 2 \\ 2 & -1 & 2 \\ 2 & 2 & -1 \end{pmatrix} \begin{pmatrix} 3 \\ 0 \\ 0 \end{pmatrix}$$

$$\begin{pmatrix} P \\ Q \\ R \end{pmatrix} = \left(\frac{1}{3}\right) \begin{pmatrix} \bar{3} \\ 6 \\ 6 \end{pmatrix} = \begin{pmatrix} \bar{1} \\ 2 \\ 2 \end{pmatrix}$$

Twin plane for Au on Si(110):

(pqr) = (330) and (hkl) = (111)

$$\begin{pmatrix} P \\ Q \\ R \end{pmatrix} = \left(\frac{1}{3}\right)\begin{pmatrix} -1 & 2 & 2 \\ 2 & -1 & 2 \\ 2 & 2 & -1 \end{pmatrix}\begin{pmatrix} 3 \\ 3 \\ 0 \end{pmatrix}$$

$$\begin{pmatrix} P \\ Q \\ R \end{pmatrix} = \left(\frac{1}{3}\right)\begin{pmatrix} 3 \\ 3 \\ 12 \end{pmatrix} = \begin{pmatrix} 1 \\ 1 \\ 4 \end{pmatrix}$$

Twin plane for Au on Si(111):

(pqr) = ($\bar{3}$33) and (hkl) = (111)

$$\begin{pmatrix} P \\ Q \\ R \end{pmatrix} = \left(\frac{1}{3}\right)\begin{pmatrix} -1 & 2 & 2 \\ 2 & -1 & 2 \\ 2 & 2 & -1 \end{pmatrix}\begin{pmatrix} \bar{3} \\ 3 \\ 3 \end{pmatrix}$$

$$\begin{pmatrix} P \\ Q \\ R \end{pmatrix} = \left(\frac{1}{3}\right)\begin{pmatrix} 15 \\ \bar{3} \\ \bar{3} \end{pmatrix} = \begin{pmatrix} 5 \\ \bar{1} \\ \bar{1} \end{pmatrix}$$

Thus, using the general matrix and applying the twin plane matrix transformation, the following twinning planes result.

(pqr) = (300); (PQR) = ($\bar{1}$22)

(pqr) = (330); (PQR) = (114)

(pqr) = ($\bar{3}$33); (PQR) = (5$\bar{1}\bar{1}$)

AUTHOR INFORMATION

[Ψ]Bioanalytical Systems, Inc., 2701 Kent Ave., West Lafayette, IN 47906, United States.

ACKNOWLEDGEMENTS

This material is based upon work supported by the U.S. Department of Energy, Office of Basic Energy Sciences, Division of Materials Sciences and Engineering, under Grant No. DE-FG02-08ER46518. The authors declare no competing financial interest.

REFERENCES

1. Kolb, D. M.; Przasnyski, M.; Gerischer, H. Underpotential Deposition of Metals and Work Function Differences. *J. Electroanal. Chem. Interfacial Electrochem.* **1974**, 54, 25-38.

2. Herrero, E.; Buller, L. J.; Abruna, H. D. Underpotential Deposition at Single Crystal Surfaces of Au, Pt, Ag and Other Materials. *Chem. Rev.* **2001**, 101, 1897-1930.

3. Brankovic, S. R.; Wang, J. X.; Adzic, R. R. Metal Monolayer Deposition by Replacement of Metal Adlayers on Electrode Surfaces. *Surf. Sci.* **2001**, 474, L173-L179.

4. Stickney, J. L. Electrochemical Atomic Layer Epitaxy. *Electroanal. Chem.* **1999**, 21, 75-209.

5. Gregory, B. W.; Stickney, J. L. Electrochemical Atomic Layer Epitaxy (ECALE). *J. Electroanal. Chem. Interfacial Electrochem.* **1991**, 300, 543-561.

6. Vaidyanathan, R.; Cox, S. M.; Happek, U.; Banga, D.; Mathe, M. K.; Stickney, J. L. Preliminary Studies in the Electrodeposition of PbSe/PbTe Superlattice Thin Films via Electrochemical Atomic Layer Deposition (ALD). *Langmuir* **2006**, 22, 10590-10595.

7. Villegas, I.; Stickney, J. L. Preliminary Studies of Gallium Arsenide Deposition on Gold (100), (110), and (111) Surfaces by Electrochemical Atomic Layer Epitaxy. *J. Electrochem. Soc.* **1992**, 139, 686-694.

8. Huang, B. M.; Colletti, L. P.; Gregory, B. W.; Anderson, J. L.; Stickney, J. L. Preliminary Studies of the Use of an Automated Flowcell Electrodeposition System for the Formation of CdTe Thin Films by Electrochemical Atomic Layer Epitaxy. *J. Electrochem. Soc.* **1995**, 142, 3007-3016.

9. Switzer, J. A.; Liu, R.; Bohannan, E. W.; Ernst, F. Epitaxial Electrodeposition of a Crystalline Metal Oxide onto Single-Crystalline Silicon. *J. Phys. Chem. B* **2002**, 106, 12369-12372.

10. Liu, R.; Bohannan, E. W.; Switzer, J. A.; Oba, F.; Ernst, F. Epitaxial Electrodeposition of Cu_2O Films onto InP(001). *Appl. Phys. Lett.* **2003**, 83, 1944-1946.

11. Liu, R.; Oba, F.; Bohannan, E. W.; Ernst, F.; Switzer, J. A. Shape Control in Epitaxial Electrodeposition: Cu_2O Nanocubes on InP(001). *Chem. Mater.* **2003**, 15, 4882-4885.

12. Liu, R.; Kulp, E. A.; Oba, F.; Bohannan, E. W.; Ernst, F.; Switzer, J. A. Epitaxial Electrodeposition of High-Aspect-Ratio $Cu_2O(110)$ Nanostructures on InP(111). *Chem. Mater.* **2005**, 17, 725-729.

13. Switzer, J. A.; Shumsky, M. G.; Bohannan, E. W. Electrodeposited Ceramic Single Crystals. *Science* **1999**, 284, 293-296.

14. Bohannan, E. W.; Jaynes, C. C.; Shumsky, M. G.; Barton, J. K.; Switzer, J. A. Low-temperature Electrodeposition of the Hightemperature Cubic Polymorph of Bismuth(III) Oxide. *Solid State Ionics* **2000**, 131, 97-107.

15. Bohannan, E. W.; Shumsky, M. G.; Switzer, J. A. Epitaxial Electrodeposition of Copper(I) Oxide on Single-Crystal Gold(100). *Chem. Mater.* **1999**, 11, 2289-2291.

16. Switzer, J. A.; Kothari, H. M.; Bohannan, E. W. Thermodynamic to Kinetic Transition in Epitaxial Electrodeposition. *J. Phys. Chem. B* **2002**, 106, 4027-4031.

17. Oba, F.; Ernst, F.; Yu, Y.; Liu, R.; Kothari, H. M.; Switzer, J. A. Epitaxial Growth of Cuprous Oxide Electrodeposited onto Semiconductor and Metal Substrates. *J. Am. Ceram. Soc.* **2005**, 88, 253-270.

18. Liu, R.; Vertegel, A. A.; Bohannan, E. W.; Sorenson, T. A.; Switzer, J. A. Epitaxial Electrodeposition of Zinc Oxide Nanopillars on Single-crystal Gold. *Chem. Mater.* **2001**, 13, 508-512.

19. Limmer, S. J.; Kulp, E. A.; Switzer, J. A. Epitaxial Electrodeposition of ZnO on Au(111) from Alkaline Solution: Exploiting Amphoterism in Zn(II). *Langmuir* **2006**, 22, 10535-10539.

20. Nikiforov, M. P.; Vertegel, A. A.; Shumsky, M. G.; Switzer, J. A. Epitaxial Electrodeposition of Fe_3O_4 on Single-crystal Au(111). *Adv. Mater. (Weinheim, Ger.)* **2000**, 12, 1351-1353.

21. Sorenson, T. A.; Morton, S. A.; Waddill, G. D.; Switzer, J. A. Epitaxial Electrodeposition of Fe_3O_4 Thin Films on the Low-Index Planes of Gold. *J. Am. Chem. Soc.* **2002**, 124, 7604-7609.

22. Kulp, E. A.; Kothari, H. M.; Limmer, S. J.; Yang, J.; Gudavarthy, R. V.; Bohannan, E. W.; Switzer, J. A. Electrodeposition of Epitaxial Magnetite Films and Ferrihydrite Nanoribbons on Single-Crystal Gold. *Chem. Mater.* **2009**, 21, 5022-5031.

23. Switzer, J. A.; Gudavarthy, R. V.; Kulp, E. A.; Mu, G.; He, Z.; Wessel, A. J. Resistance Switching in Electrodeposited Magnetite Superlattices. *J. Am. Chem. Soc.* **2010**, 132, 1258-1260.

24. He, Z.; Gudavarthy, R. V.; Koza, J. A.; Switzer, J. A. Roomtemperature Electrochemical Reduction of Epitaxial Magnetite Films to Epitaxial Iron Films. *J. Am. Chem. Soc.* **2011**, 133, 12358-12361.

25. Switzer, J. A.; Kothari, H. M.; Poizot, P.; Nakanishi, S.; Bohannan, E. W. Enantiospecific Electrodeposition of a Chiral Catalyst. *Nature* **2003**, 425, 490-493.

26. Kothari, H. M.; Kulp, E. A.; Boonsalee, S.; Nikiforov, M. P.; Bohannan, E. W.; Poizot, P.; Nakanishi, S.; Switzer, J. A. Enantiospecific Electrodeposition of Chiral CuO Films from Copper-(II) Complexes of Tartaric and Amino Acids on Single-Crystal Au(001). *Chem. Mater.* **2004**, 16, 4232-4244.

27. Boonsalee, S.; Gudavarthy, R. V.; Bohannan, E. W.; Switzer, J. A. Epitaxial Electrodeposition of Tin(II) Sulfide Nanodisks on Single Crystal Au(100). *Chem. Mater.* **2008**, 20, 5737-5742.

28. He, Z.; Koza, J. A.; Mu, G.; Miller, A. S.; Bohannan, E. W.; Switzer, J. A. Electrodeposition of $Co_xFe_{3-x}O_4$ Epitaxial Films and Superlattices. *Chem. Mater.* **2013**, 25, 223-232.

29. Koza, J. A.; Schroen, I. P.; Willmering, M. M.; Switzer, J. A. Electrochemical Synthesis and Nonvolatile Resistance Switching of Mn_3O_4 Thin Films. *Chem. Mater.* **2014**, 26, 4425-4432.

30. Koza, J. A.; He, Z.; Miller, A. S.; Switzer, J. A. Electrodeposition of Crystalline Co_3O_4-A Catalyst for the Oxygen Evolution Reaction. *Chem. Mater.* **2012**, 24, 3567-3573.

31. Koza, J. A.; Hill, J. C.; Demster, A. C.; Switzer, J. A. Epitaxial Electrodeposition of Methylammonium Lead Iodide Perovskites. *Chem. Mater.* **2016**, 28, 399-405.

32. Switzer, J. A.; Shane, M. J.; Phillips, R. J. Electrodeposited Ceramic Superlattices. *Science* **1990**, 247, 444-446.

33. Switzer, J. A.; Raffaelle, R. P.; Phillips, R. J.; Hung, C. J.; Golden, T. D. Scanning Tunneling Microscopy of Electrodeposited Ceramic Superlattices. *Science* **1992**, 258, 1918-1921.

34. Switzer, J. A.; Hung, C. J.; Breyfogle, B. E.; Shumsky, M. G.; Van Leeuwen, R.; Golden, T. D. Electrodeposited Defect Chemistry Superlattices. *Science* **1994**, 264, 1573-1576.

35. Kothari, H. M.; Vertegel, A. A.; Bohannan, E. W.; Switzer, J. A. Epitaxial Electrodeposition of Pb-Tl-O Superlattices on Single-Crystal Au(100). *Chem. Mater.* **2002**, 14, 2750-2756.

36. Love, J. C.; Estroff, L. A.; Kriebel, J. K.; Nuzzo, R. G.; Whitesides, G. M. Self-assembled Monolayers of Thiolates on Metals as a Form of Nanotechnology. *Chem. Rev.* **2005**, 105, 1103-1169.

37. Sayed, S. Y.; Wang, F.; Malac, M.; Meldrum, A.; Egerton, R. F.; Buriak, J. M. Heteroepitaxial Growth of Gold Nanostructures on Silicon by Galvanic Displacement. *ACS Nano* **2009**, 3, 2809-2817.

38. Prod'homme, P.; Maroun, F.; Cortes, R.; Allongue, P. Electrochemical Growth of Ultraflat Au(111) Epitaxial Buffer Layers on H-Si(111). *Appl. Phys. Lett.* **2008**, 93, 171901.

39. Warren, S.; Prod'homme, P.; Maroun, F.; Allongue, P.; Cortes, R.; Ferrero, C.; Lee, T.-L.; Cowie, B. C. C.; Walker, C. J.; Ferrer, S.;Zegenhagen, J. Electrochemical Au Deposition on Stepped Si(111)-H surfaces: 3D versus 2D Growth Studied by AFM and X-ray Diffraction. *Surf. Sci.* **2009**, 603, 1212-1220.

40. Allongue, P.; Maroun, F. Electrodeposited Magnetic Layers in the Ultrathin Limit. *MRS Bull.* **2010**, 35, 761-770.

41. Tournerie, N.; Engelhardt, A. P.; Maroun, F.; Allongue, P. Influence of the Surface Chemistry on the Electric-field Control of the Magnetization of Ultrathin Films. *Phys. Rev. B: Condens. Matter Mater. Phys.* **2012**, 86, 104434.

42. Kulp, E. A.; Limmer, S. J.; Bohannan, E. W.; Switzer, J. A. Electrodeposition of Nanometer-thick Ceria Films by Oxidation of Cerium(III)-acetate. *Solid State Ionics* **2007**, 178, 749-757.

43. Phung, T. M.; Johnson, D. C.; Antonelli, G. A. A Detailed Experimental and Analytical Study of the Thermal Expansion of Dielectric Thin Films on Si by X-ray Reflectivity. *J. Appl. Phys.* **2006**, 100, 064317.

44. Hill, J. C.; Landers, A. T.; Switzer, J. A. An Electrodeposited Inhomogeneous Metal-insulator-semiconductor Junction for Efficient Photoelectrochemical Water Oxidation. *Nat. Mater.* **2015**, 14, 1150-1155.

45. Poizot, P.; Hung, C.-J.; Nikiforov, M. P.; Bohannan, E. W.; Switzer, J. A. An Electrochemical Method for CuO Thin Film Deposition from Aqueous Solution. Electrochem. *Solid-State Lett.* **2003**,6, C21-C25.

46. Thomas, G.; Goringe, M. J.: *Transmission Electron Microscopy of Materials;* John Wiley Sons: New York, 1979. pp 94-100.

47. Li, B. Q.; Zuo, J. M. The Development of Epitaxy of Nanoclusters on Lattice-Mismatched Substrates: Ag on H-Si(111) *Surfaces. Surf. Sci.* **2002**, 520, 7-17.

III. EPITAXIAL LIFT-OFF OF ELECTRODEPOSITED SINGLE-CRYSTAL GOLD FOILS FOR FLEXIBLE ELECTRONICS

Naveen K. Mahenderkar[1], Qingzhi Chen[2], Ying-Chau Liu[2], Alexander R. Duchild[2], Seth Hofheins[2], Eric Chason[3], and Jay A. Switzer[2,*]

[1]Department of Materials Science and Engineering and Graduate Center for Materials Research, Missouri University Science and Technology Rolla, Missouri, 65409.

[2]Department of Chemistry and Graduate Center for Materials Research, Missouri University Science and Technology Rolla, Missouri, 65409.

[3]School of Engineering, Brown University, Providence, Rhode Island, 02912

*Email: jswitzer@mst.edu

ABSTRACT

We introduce a simple and inexpensive procedure for epitaxial lift-off of wafer-size flexible and transparent foils of single-crystal gold using silicon as a template. Lateral electrochemical undergrowth of a sacrificial SiO_x layer was achieved by photoelectrochemically oxidizing silicon under light irradiation. A 28-nanometer-thick gold foil with a sheet resistance of 7 ohms per square showed only a 4% increase in resistance after 4000 bending cycles. A flexible organic light-emitting diode based on tris(bipyridyl)ruthenium(II) that was spin-coated on a foil exploited the transmittance and flexibility of the gold foil. Cuprous oxide as an inorganic semiconductor that was epitaxially electrodeposited onto the gold foils exhibited a diode quality factor n of 1.6 (where n = 1.0 for an ideal diode), compared with a value of 3.1 for a polycrystalline deposit. Zinc oxide nanowires electrodeposited epitaxially on a gold foil also showed flexibility, with the nanowires intact up to 500 bending cycles.

1. INTRODUCTION

Single-crystal silicon (Si) is the bedrock of semiconductor devices; its high crystalline perfection minimizes electron-hole recombination, and its dense SiO_x native oxide minimizes surface states. There is interest in moving beyond the planar structure of conventional Si-based chips to produce flexible electronic devices such as wearable solar cells, sensors, and flexible displays.[1−5] Flexible devices and beautiful architectures have been produced using ultrathin foils of Si.[6−8] Conductive polymers,[9] carbon nanotubes,[10] graphene,[11] and metal nanostructures[12,13] have been used as transparent and flexible substrates for flexible electronics. Ultrathin (5 to 30 nm) metal films[14,15] have relatively high optical transmittance, flexibility, improved device efficiency, and low sheet resistance. However,they usually are grown by vacuum evaporation or sputtering, which gives a polycrystalline or textured deposit. Polycrystalline electronic materials suffer from electron-hole recombination at grain boundaries.[16] To expand the palette of electronic materials beyond planar Si, an inexpensive source of highly ordered material is needed that can serve as an inert substrate for the epitaxial growth of grain boundary-free semiconductors, optical materials, and superconductors.

We show that wafer-size transparent and flexible single-crystal foils of gold (Au) can be produced by a simple and inexpensive lift-off procedure using single-crystal Si as the template for electrochemical epitaxial growth. The transparency of these single-crystal Au foils is exploited to fabricate a flexible organic light-emitting diode (OLED) based on tris(bipyridyl)ruthenium(II). The single-crystal nature of the Au is used to produce an inorganic diode based on epitaxial cuprous oxide (Cu_2O) that has more ideal diode characteristics than a diode based on polycrystalline Cu_2O.

2. RESULTS AND DISCUSSION

Epitaxial lift-off of films on single-crystal substrates by dissolving a sacrificial adhesion layer can produce free-standing single-crystal foils.[17] The epitaxial lift-off procedure for ultrathin single-crystal foils of Au electrodeposited onto Si(111) substrate is shown in Figure 1. Electrodeposition of epitaxial Au on a Si(111) substrate was carried out using the method developed by Allongue and co-workers.[18,19] Previously, we showed that epitaxial electrodeposition of Au on Si(111), Si(100), and Si(110) substrates can serve as a proxy for bulk single-crystal Au.[20] Single-crystal Si(111) with a 0.2° miscut toward Embedded Image and a resistivity of 1.15 Ω.cm was used as the substrate to grow the Au foils (Figure 1A). The deposition was performed at room temperature in a solution containing 0.1 mM $HAuCl_4$, 1 mM KCl, 1 mM H_2SO_4, and 0.1 M K_2SO_4 with a Si electrode that was prepolarized at -1.9 V *versus* Ag/AgCl before inserting it in the solution (Figure 1B). Prepolarizing the electrode inhibited the formation of an amorphous native oxide layer on the surface of Si and enabled epitaxial growth of Au.

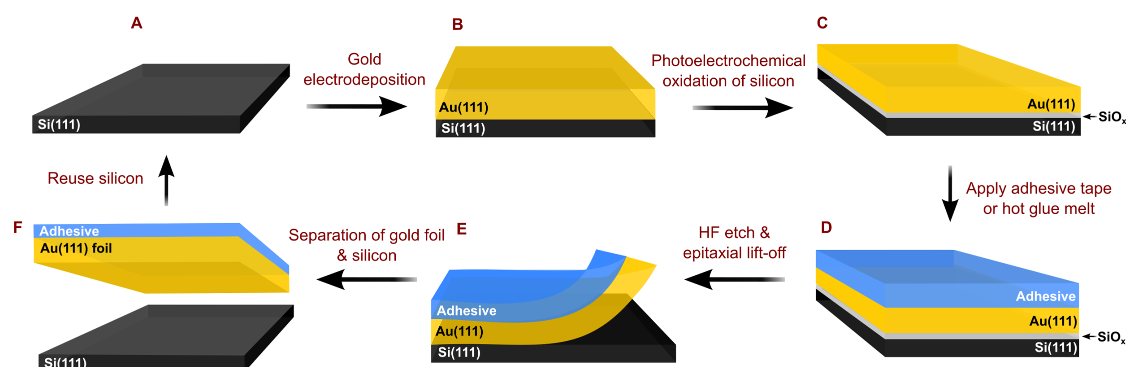

Figure 1. Schematic for epitaxial lift-off of single-crystal Au foil. (A) Miscut n-type Si(111) wafer without the native oxide layer. (B) Epitaxial electrodeposition of Au on Si(111) from a 0.1 mM $HAuCl_4$ solution at -1.9 V *versus* Ag/AgCl with prepolarized electrode. (C) Photoelectrochemical oxidation of Si under irradiation of light in 0.5 M H_2SO_4 solution at 0.75 V *versus* Ag/AgCl. (D) A polymer adhesive (tape/hot glue) is applied to the surface of Au to aid the foil separation. (E) A sacrificial SiO_x interlayer is etched using dilute (5%) hydrofluoric acid to separate the foil from the Si substrate. (F) Single-crystal Au foil completely detached from the Si surface.

After the epitaxial growth of Au, lateral undergrowth of a sacrificial SiO_x layer was achieved by photoelectrochemically oxidizing Si under irradiation of light at +0.75 V *versus* Ag/AgCl in 0.5 M H_2SO_4 solution (Figure 1C). Au/n-Si forms a Schottky (rectifying) junction, so irradiation of light is required to generate holes at the Au/n-Si interface to oxidize the Si. The epitaxy of the Au foil was maintained during the lateral undergrowth of SiO_x, analogous to the epitaxial lateral overgrowth process in silicon-on-insulator technology.[21] A polymer adhesive (tape or hot glue) was applied to the Au surface as a support and facilitator for foil separation (Figure 1D). The SiO_x layer was etched using dilute (5%) hydrofluoric acid to detach the Au foil from the Si substrate (Figure 1E); this enabled an effortless separation of the foil (Figure 1F). Both the tape and hot glue have high optical transmittance in the visible range (400 to 800 nm) and are resistant to chemical etching procedures. After the foil separation, the Si substrate was etched using a 0.6 M KI and 0.1 M I_2 solution to dissolve any residual Au and then reused. Because only a 2-to 3-nm-thick layer of SiO_x is removed during each fabrication cycle without extensive roughening, the Si should be reusable thousands of times.

High-resolution transmission electron microscopy (HRTEM) was used to study the interfacial changes during photoelectrochemical oxidation of Si. The as-deposited 30-min film (i.e., 30 min of deposition time) did not show an interfacial SiO_x layer between the Si(111) and Au(111), as seen by the abrupt transition at the interface in Figure 2A. Electron diffraction patterns for the as-deposited layers of Au on Si showed a spot pattern with in-plane and out-of-plane order (Figure S1). After the photoelectrochemical oxidation of Si, an amorphous SiO_x interface with a thickness of 2.45 nm was evident in Figure 2B. Native oxide formation on the Si surface in ambient air is limited to 0.5 to 1 nm because of the dense pinhole-free oxide layer that protects the Si from further oxidation. However, during photoelectrochemical oxidation of Si, tunneling of electrons through the insulating oxide layer caused the SiO_x layer to grow thicker. The tunneling of electrons completely ceased

when the oxide layer reached a thickness of 2.0 to 2.5 nm and the photocurrent dropped nearly to zero (Figure S2). The electron diffraction pattern of Au on Si with an interfacial oxide layer showed a similar spot pattern, indicating that the epitaxy was maintained after the lateral undergrowth of SiO_x (Figure S3). Both micrographs (Figure 2, A and B) are viewed along the Embedded Image zone axis, and the measured d-spacings for Au and Si are consistent with bulk values.

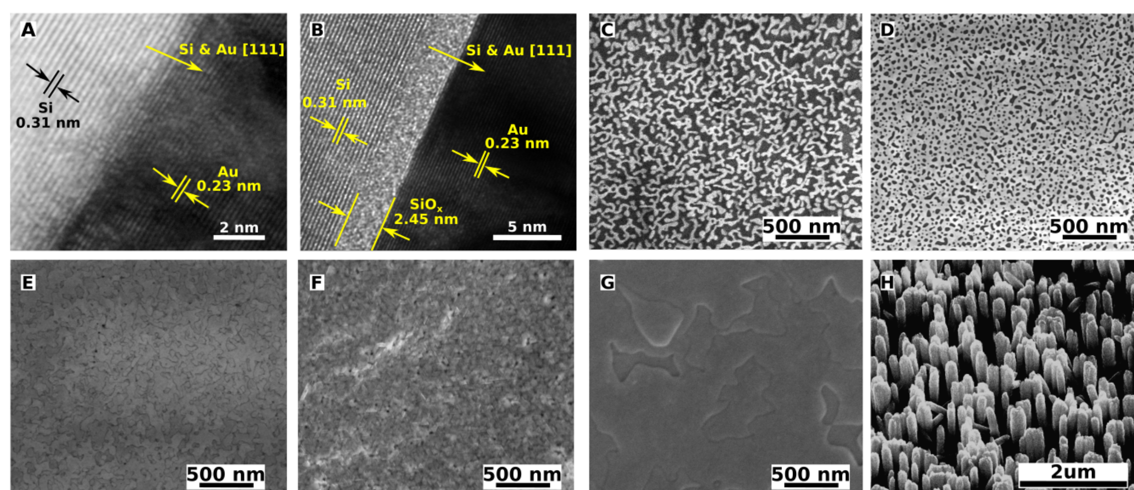

Figure 2. Electron microscopy of the single-crystal Au, epitaxial Cu_2O, and epitaxial ZnO. (A and B) High-resolution TEM cross section of epitaxial Au on Si without the SiO_x interlayer for the as-deposited film (A) and with the SiO_x layer after photoelectrochemical oxidation of Si (B). (C to F) Surface morphology of Au foils deposited for 5 min (7 nm) (C), 10 min (11 nm) (D), 20 min (21 nm) (E), and 30 min (28 nm) (F). (G) Electrodeposited epitaxial Cu_2O on 30-min Au foil. (H) Electrodeposited ZnO nanowires on 10-min Au foil subjected to 500 bending cycles.

Scanning electron microscopy (SEM) was performed to study the surface morphology and the initial nucleation and growth of Au foils. All of the foils for SEM were separated with an adhesive tape as the support layer. Figure 2C shows a segment of Au foil formed after 5 min with a fractal morphology that had been reported for evaporated ultrathin films of Au.[22,23] We attribute these fractal features to the diffusion-limited aggregation of Au on the surface of Si during the initial nucleation period. This Au foil has a coverage of 56% and appears to be at the percolation threshold thickness (5 to 6 nm), in agreement

with the results of Hövel et al.[24] Beyond the percolation threshold, the fractal features are interconnected in a large network mesh with electrical connectivity across the entire foil. Figure 2D shows Au foils deposited for 10 min with 70% coverage; Au foils deposited for 20 min and 30 min, respectively, are shown in Figure 2, E and F.

The applicability of Au foils as a substrate was shown by depositing and characterizing inorganic semiconductor thin film and nanowires. Cu_2O was electrodeposited on a 30-min Au foil (Figure 2G) for study of the diode characteristics. Zinc oxide (ZnO) nanowires were electrodeposited on a 10-min Au foil (Figure 2H) and were subjected to 500 bending cycles with a radius of curvature of 3 mm. The ZnO remained intact after the bending cycles, which can be attributed to its nanowire morphology and the flexibility of Au foil. Although the 5 and 10-min Au foils appear porous, foils beyond the percolation threshold thickness (5 to 6 nm) enable electrical contact over the entire sample area and make electrodeposition feasible.

We probed epitaxial Au on Si and free-standing Au foils using x-rays to study the out-of-plane and in-plane orientations. Figure 3A shows the x-ray diffraction (XRD) pattern of a 30-min Au deposition on Si, where Au follows the [111] orientation of Si, indicating a high out-of-plane order. The Au thickness on Si was measured from the interference fringes in the XRD pattern (Figure 3B). Satellite peaks (Laue oscillations) around a Bragg peak caused by constructive and destructive interference of x-rays reflected from Si-Au and Au-air interfaces were used to precisely measure the Au thickness.[19] Figure 3B shows Laue oscillations around the Au(111) peak for Au films on Si as a function of deposition time. The film thickness was determined from the satellite peak positions according to

$$t = \left[\frac{(L_1 - L_2)\lambda}{2(\sin\theta_1 - \sin\theta_2)} \right] \tag{1}$$

where t is the film thickness, L is the satellite peak order (numbering of peaks in Figure 3B), λ is the x-ray wavelength (0.15418 nm), and θ is the satellite peak angle. The calculated thicknesses from the Laue oscillations for the corresponding deposition times are listed in Figure 3B. A linear dependence of thickness with time was observed (Figure S4). Figure 3C shows the XRD pattern of a segment of Au foil and electrodeposited Cu_2O and ZnO on Au foil. Both the Au foil and the electrodeposited Cu_2O had a strong [111] out-of-plane orientation. The thickness of a 10-min deposition of Au on Si agreed closely with that of Au foil measured using Laue oscillations (Figure S5). The ZnO also grew epitaxially on Au foil but showed a strong [0001] out-of-plane orientation because of its hexagonal crystal structure.

The in-plane orientation and the epitaxial relation of the Au on Si, Au foil, Cu_2O, and ZnO was determined with x-ray pole figures. In a pole figure, planes other than those parallel to the substrate surface are probed while tilting and rotating the sample through a series of tilt and azimuthal angles (Figure S6). Figure 3D shows a (220) pole figure of Si(111), with three spots separated azimuthally by 120° at a tilt angle of 35.5°, corresponding to the three-fold symmetry of the (111) plane. A (220) pole figure of Au(111) on Si(111) is shown in Figure S7 with three spots expected at a tilt angle of 35.5°; however, there are also an additional three spots separated azimuthally by 60°. The two sets of spots on the (220) pole figure of Au correspond to the 180° in-plane rotation of parallel and antiparallel domains. Figure 3E shows a (220) pole figure of Au(111) foil, with the six spots at a tilt angle of 35.5° separated azimuthally by 60°. This pattern shows that the Au maintained its high in-plane and out-of-plane order after the foil separation. Figure 3F shows a (220) pole figure of Cu_2O(111) electrodeposited on Au(111) foil with the expected six spots at a tilt angle of 35.5°. Figure 3G shows a (102) pole figure of ZnO(002) with six spots at a tilt

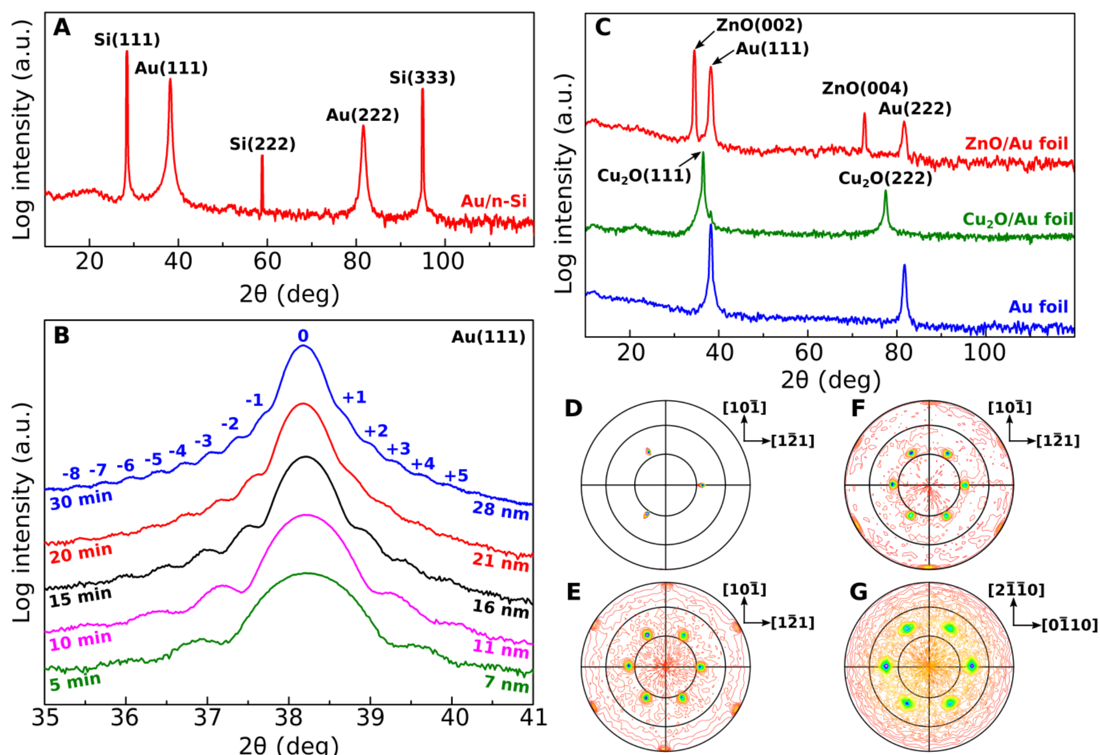

Figure 3. X-ray diffraction and pole figures to study the in-plane and out-of-plane orientation. (A) Out-of-plane orientation of electrodeposited Au(111) on Si(111). (B) Out-of-plane x-ray diffraction showing satellite peaks (Laue oscillations) caused by constructive and destructive interference. (C) Out-of-plane orientation of Au(111) foil, electrodeposited Cu_2O on 30-min Au foil, and electrodeposited ZnO on 10-min Au foil. (D to G) In-plane orientation was determined using (220) pole figure of Si(111) (D), (220) pole figure of Au(111) foil (E), (220) pole figure of Cu_2O(111) on Au(111) foil (F), and (102) pole figure of ZnO(002) on Au(111) foil (G). The radial lines in the pole figure correspond to 30° increments of the tilt angle.

angle of 42.77° separated azimuthally by 60°. The six spots for ZnO are expected from the six-fold symmetry of the (0002) basal plane of the hexagonal crystal structure.

To understand the epitaxial relation, it is crucial to look at the lattice mismatch of the film and the substrate. The lattice mismatch can be defined as $[(d_{film} - d_{substrate})/d_{substrate}]$, where d is the lattice spacing of the plane parallel to the substrate. Au on Si has a lattice mismatch of -24.9%, which is too high to produce epitaxial deposits. Therefore, the epitaxy in the Au-Si system can be explained by the formation of coincidence site lattices (CSLs),

in which four unit meshes of Au coincide with three unit meshes of Si.[20] These CSLs lower the mismatch from -24.9% for a single unit cell to +0.13% for the CSL (Figure S8). Similarly, the lattice mismatch for ZnO on Au was minimized from +12.7% to +0.16% for the CSL (Figure S9). The lattice mismatch for Cu_2O on Au is +4.7%, which is low enough to produce cube-on-cube epitaxial films with reasonable in-plane and out-of-plane strain in the material (Figure S10).

High optical transmittance and low sheet resistance are imperative for Au foils to be used as flexible and transparent substrates. Figure 4A shows the photograph of a wafer-size Au foil with a diameter of 50.8 mm. Figure 4B shows the optical transmittance of Au foils as a function of thickness. All of the foils showed a maximum in transmittance around 500 nm and the peaks slightly red-shifted with an increase in thickness. The sheet resistance, in terms of ohms per square, for all of the foils (measured with a four-point probe) increased along with transmittance as the Au foil thickness decreased. A 7-nm-thick Au foil showed the highest transmittance at 85%, and the 28-nm-thick foil showed the lowest at 25%. The maximum transmittance (ca. 500 nm) as a function of thickness is in close agreement with previous studies on evaporated gold thin films.[25] The endurance of the Au foils as a function of sheet resistance was measured by subjecting the foils to as many as 4000 bending cycles (Figure 4C). Bending cycles for all of the foils were performed with a steel rod as a guide with a radius of curvature of 3 mm. The sheet resistance of 28-, 16-, and 11-nm-thick Au foils increased by 4%, 6.3%, and 34%, respectively, after 4000 cycles of bending.

To evaluate the flexibility and transmittance of Au foils for light emission, we spin-coated an OLED based on tris(bipyridyl)ruthenium(II).[26,27] The complex showed strong photoluminescence with an excitation wavelength of 455 nm and an emission of bright red-orange color around 660 nm.[26] The complex was dissolved in a 3% (w/v) polyvinyl alcohol solution, spin-coated onto a 28-nm-thick Au foil, and dried in air. An indium/gallium

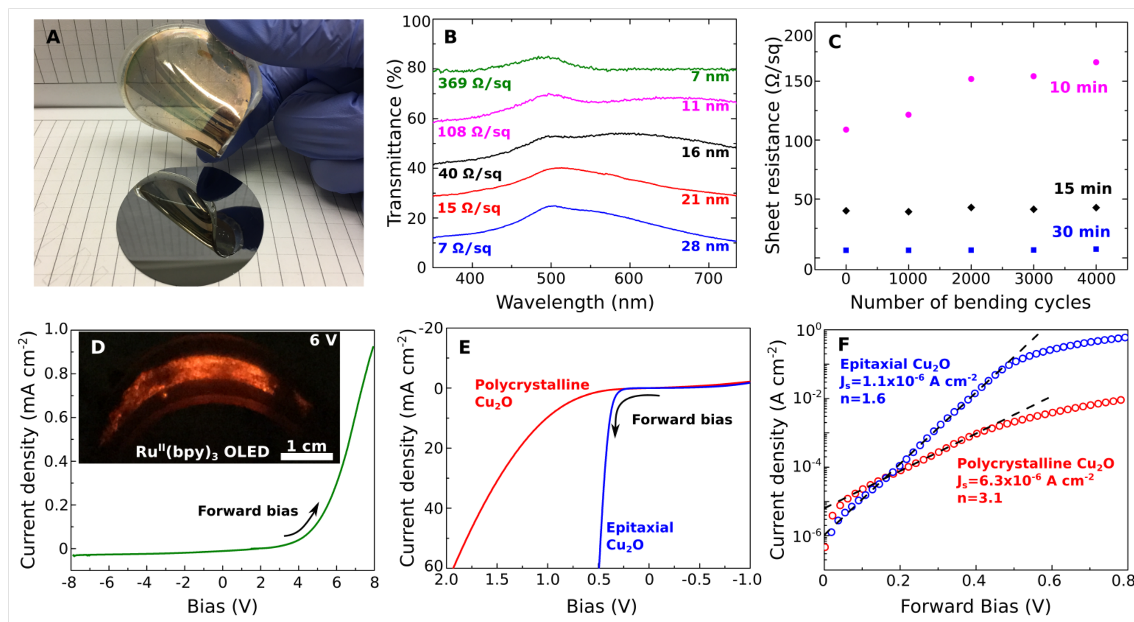

Figure 4. Transmittance, sheet resistance, and flexibility of Au foils with diode and OLED fabrication. (A) Wafer-size Au foil with diameter of 50.8 mm and thickness of 28 nm. (B) Transmittance and sheet resistance of Au foils as a function of thickness. (C) Sheet resistance of Au foils with thicknesses of 11, 16, and 28 nm as a function of bending cycles with a bending curvature of 3 mm. (D) Current-voltage response of Au foil/Ru^{II}(bpy)$_3$/InGa junction, showing rectifying behavior. Inset: Red-orange electrogenerated chemiluminescence of Ru^{II}(bpy)$_3$BF$_4$ OLED on flexible 28-nm-thick Au foil. (E) Current-voltage response of Cu_2O diode on Au foil (epitaxial) and stainless steel (polycrystalline) substrates. (F) Dark saturation current density (J_s) and diode quality factor (n) of epitaxial and polycrystalline Cu_2O diodes measured using $\log(J)$ versus V at forward bias.

(InGa) eutectic was used as a back contact as a low-work function metal, whereas the Au foil acted as a high-work function contact. Figure 4D shows the current-voltage response of Au foil/Ru^{II}(bpy)$_3$/InGa junction with a diode (rectifying) behavior. The inset in Figure 4D shows a flexible Au foil with electrogenerated chemiluminescence from the OLED at an applied forward bias of 6 V.

To study the single-crystal nature of Au foils, we prepared an inorganic diode by using electrodeposited Cu_2O on Au foil. InGa eutectic was used to make a rectifying contact to the p-Cu_2O, and the Au foil substrate served as the ohmic contact. Polycrystalline

Cu_2O was electrodeposited on a stainless steel substrate from the same deposition solution at low overpotentials to produce a sample with a random orientation. Cu_2O on both the Au foil and the stainless steel were deposited for a constant charge density to maintain similar thickness. The XRD pattern of Cu_2O on stainless steel with a polycrystalline powder pattern is shown in Figure S11. Defects or grain boundaries in a material increase the probability of electron-hole recombination and lower the overall efficiency of the diode or solar cell. In a single crystal, an ideal diode quality factor (n) of 1 indicates diffusion-controlled currents with no electron-hole recombination in the material, but in polycrystalline materials, n varies from 2 to 7.[28,29] The n value for polycrystalline Si also increases with decreasing grain size.[29] Figure 4E shows current-voltage responses for a Cu_2O diode on Au foil and stainless steel. The epitaxial Cu_2O had an n of 1.6, whereas the polycrystalline Cu_2O had an n of 3.1 (Figure 4F). The higher value of n for polycrystalline Cu_2O is consistent with previous results for films of Cu/Cu_2O Schottky diode solar cells.[30]

3. CONCLUSIONS

Single-crystal Au foils offer the order of traditional semiconductors such as Si wafers without the constraint of a rigid substrate. The foils are flexible and optically transparent, and show promise for producing flexible and wearable displays, solar cells, and sensors. The epitaxial growth of Cu_2O and ZnO that we have demonstrated can be applied to a wide range of inorganic semiconductors such as CdSe, CdTe, and ZnSe for use in flexible solar cells. Because ZnO is both a wide-bandgap semiconductor and a piezoelectric material, it should be possible to produce pressure-sensitive electronic skin and LEDs based on the ZnO/Au system.[31,32] Also, Au is hypoallergenic and could serve as a platform for wearable sweat sensors for continuous health monitoring.[5] Although this work focused on the production of ordered substrates for flexible electronics, the processing method can be used to provide an inexpensive source of large metallic single crystals. These could serve as

ordered substrates for photovoltaics, high-temperature superconductors, stress-free micro-electromechanical systems (MEMS), catalysts, underpotential deposition, self-assembled monolayers, and molecular electronics.

SUPPLEMENTARY MATERIALS

Si Wafer and Etching Procedure. Phosphorous doped single-side polished n-Si(111) was miscut 0.2 degrees towards $[11\bar{2}]$ with resistivity of 1.15 Ω.cm. The wafer was obtained from Virginia Semiconductor Inc. Aluminum was sputtered on the back of Si wafer to form an ohmic contact and silver wire with silver paste (GC electronics, silver print II) was used to make the back contact. Silicone paste and/or nail polish was used as an insulating and inert layer on the back of Si to prevent contact with the electrolyte during electrodeposition. Si wafers prior to use were etched in 5% hydrofluoric acid (HF) solution for 30 seconds to dissolve the native oxide, then soaked in hot DI water (ca. 80-90 °C) for 15 minutes to passivate the surface with an SiO_x layer and then etched again with 5% HF for 30 seconds and buffered hydrofluoric acid for 30 seconds to make a H-terminated surface. Ethanol was used to clean any organic residue and rinsed with DI water prior to deposition. All depositions were immediately followed by the etching process to avoid any surface passivation. After photoelectrochemical oxidation of Si, SiO_x was etched using 5% HF to separate the Au foil.

Electrodeposition of Au and Au Foil Fabrication. Au was electrodeposited from a plating solution containing 0.1 mM $HAuCl_4$, 1 mM KCl, 1 mM H_2SO_4, and 100 mM K_2SO_4 in deionized (DI) water (18-20). The solution was prepared by adding 10 mL of a stock solution containing 1 mM $HAuCl_4$, 10 mM KCl, and 10 mM H_2SO_4 to 90 mL of DI water. Finally, 100 mM K_2SO_4 was added as a supporting electrolyte with a pH of ca. 3. All depositions used an Ag/AgCl reference electrode and a Pt coil as a high surface area

counter electrode. A -1.9 V *versus* Ag/AgCl pre-polarized potential was applied before inserting the Si electrode into the solution and the deposition was carried out for various deposition times at room temperature with 200 rpm stirring. The key step during deposition was the pre-polarized dip of Si in the electrolyte to avoid native oxide formation and to prevent electroless deposition of Au on Si. After the deposition, films were rinsed with DI water and dried in air. Au on Si films showed no native oxide passivation at the Si interface and were stable in lab atmosphere for more than a year. As deposited Au on Si deposits were photoelectrochemically oxidized under light irradiation at an applied potential of +0.75 V *versus* Ag/AgCl in 0.5M H_2SO_4 solution at room temperature. All the Au on Si samples were photoxidized for 30 minutes. A polymer adhesive or tape is applied to the Au film while on Si and then SiO_x was etched using 5% HF to detach the Au foil. All the foils after etching separated effortlessly enabling a crack-free Au foil.

Electrodeposition of Cu_2O and ZnO. Cu_2O was electrodeposited from a plating solution containing 0.2 M $CuSO_4.5H_2O$, 0.2 M $C_4H_6O_6$ (L-tartaric acid), and 3 M NaOH.[33,34] A solution of $CuSO_4$ and L-tartaric acid was prepared separately and was slowly added to the solution of 3 M NaOH. A dark blue solution is obtained. The solution was stored at 0 °C and all the deposition were performed at 30 °C. A cathodic current density of 1.0 mA cm^{-2} was passed for a constant charge density of 1.8 C cm^{-2} at a temperature of 30 °C and a stir rate of 200 rpm. All the deposits were rinsed with DI water and dried in air and used as deposited without any post-processing. Electrodeposition of ZnO[35,36] was performed from a solution containing 0.1 mM $Zn(NO_3)_2$ and 0.1 M KCl at an applied potential of -1.1 V *versus* Ag/AgCl at 70 °C and 200 rpm stirring. Electrodeposition of Au, Cu_2O and ZnO films was done using either an EGG Model 273A or an Autolab 30 potentiostat/galvanostat.

X-ray Diffraction Measurements and Interface Models. All XRD measurements were made with a Philips X-Pert Panalytical (Materials Research Diffractometer) with Cu K_{α_1} radiation source (λ = 1.54056 Å). All 2theta-omega (out-of-plane orientation) and Laue oscillation scans were done using a hybrid 2-bounce with 2xGe 220 Asym. monochromator and Ni 0.125 mm automatic beam attenuator and a 0.18° parallel plate collimator diffracted optics. Pole figures were measured using a crossed slit collimator with 2 mm divergence slit and 2 mm mask with a Ni filter and a 0.27° parallel plate collimator. Lattice constants for interface models and X-Ray measurements of Si were referred from JCPDS card no. 027-1402, Au from 004-0784, Cu_2O from 005-0667 and ZnO from 036-1451. All the interface models for Au on Si, Cu_2O on Au foil and ZnO on Au foil were made using VESTA (visualization for electronic and structural analysis) software version 3.3.2.

SEM and TEM Measurements. High resolution cross-sectional TEM images for Au on Si before and after photoelectrochemical oxidation were measured using the Tecnai F20. SEM of Au foil, Cu_2O and ZnO were determined using Helios Nanolab 600 DualBeam. Focused ion-beam milling for TEM sample preparation was done using Helios Nanolab 600 DualBeam. Prior to focused ion-beam milling, the films were sputtered with a thin carbon layer using a Denton sputtering system to protect the Au film during milling process and to provide a contrast difference in order to determine the thickness of films accurately.

Transmittance and Sheet Resistance Measurements. Transmittance for all the Au foils were measured using a Varian Cary 5 UV-Vis-NIR dual-beam spectrophotometer. All the Au foils for transmittance measurement were separated using scotch tape as the support layer, therefore a bare tape sample was used in the reference beam during measurement. A baseline scan was measured without any sample in both the beam paths prior to the Au foil. The sheet resistance measurements were performed using a C4S 44/5S

four-probe measurement system from Cascade Microtech, Inc. The current was applied using a Keithley 220 programmable current source and the voltage was measured using a HP 3457A multimeter. A minimum of 3 measurements were performed on each sample and averaged to obtain the sheet resistance.

Tris(bipyridyl)ruthenium (II) terafluoroborate ($[Ru(bpy)_3](BF_4)$) Synthesis and OLED Fabrication. $RuCl_3.3H_2O$ was dehydrated by placing the powder in an oven at 100 °C overnight and slowly cooling it to room temperature. All the reactions were performed in a fume hood. 0.083 g of dried $RuCl_3$ was mixed with 8 mL of DI water in a 25 mL Erlenmeyer flask and heated to reflux while stirring. To the solution while heating, 0.188 g of 2,2"-bipyridine and 440 μL of 6M NaH_2PO_2 was added. The solution has a dark blackish color before heating and after heating at 80 °C for about 30 minutes, the solution color changes to bright orange. The water level was marked and during refluxing, DI water was added as necessary to maintain the same volume. After refluxing, a 1.5 mL solution with 0.333 g of $NaBF_4$ was added to the refluxing orange solution and stirred for 5 minutes. The solution was cooled to room temperature and then placed in a refrigerator to further cool down to enable precipitation of the complex. The solution was filtered using a Büchner funnel and the precipitate was dried at room temperature. The OLED was fabricated by spin-coating the solution of $[Ru(bpy)_3](BF_4)$ dissolved in a 3% (w/v) polyvinyl alcohol (PVA) solution. The PVA solution was prepared by slowly dissolving 0.15 g of PVA in 5 mL of boiling water.[26,27] 0.035 g of as-prepared $[Ru(bpy)_3](BF_4)$ complex was dissolved in 3 mL of PVA solution and the mixture was spin-coated on Au foil at 500 rpm. The coating was dried at room temperature for 2-3 hours. Indium-gallium eutectic was applied on the OLED coating as a back contact.

Measurement of Interfacial Energetics. All current voltage response curves were measured using a PARSTAT 2273 potentiostat/galvanostat with a Au coil in contact with InGa eutectic as a back contact and the Au foil or stainless steel as front contact.

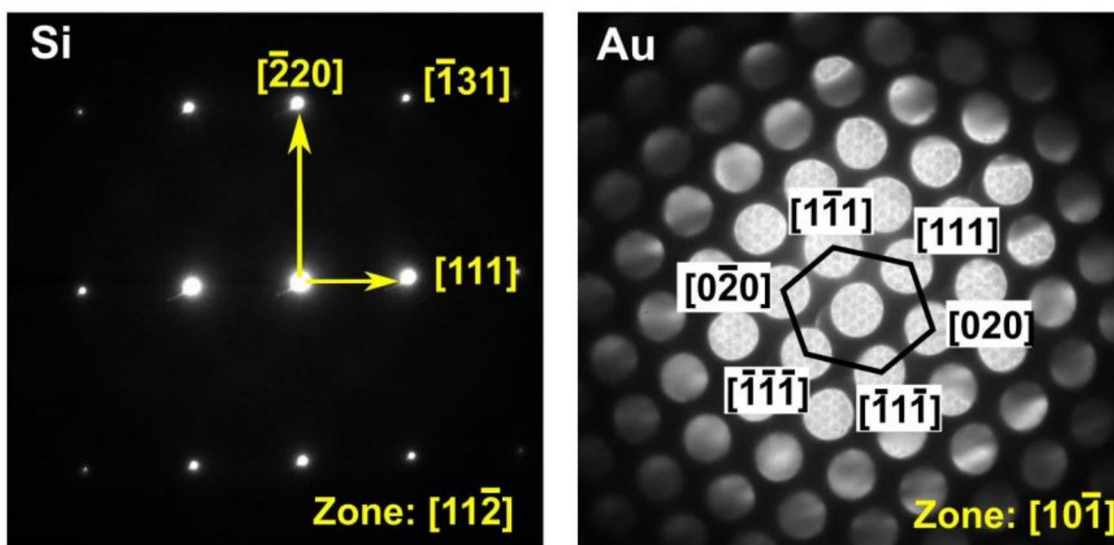

Figure S1. Electron diffraction pattern of as-deposited Au on Si showing a spot pattern. Convergent beam diffraction on Au films because of lower thickness yields broader spots.

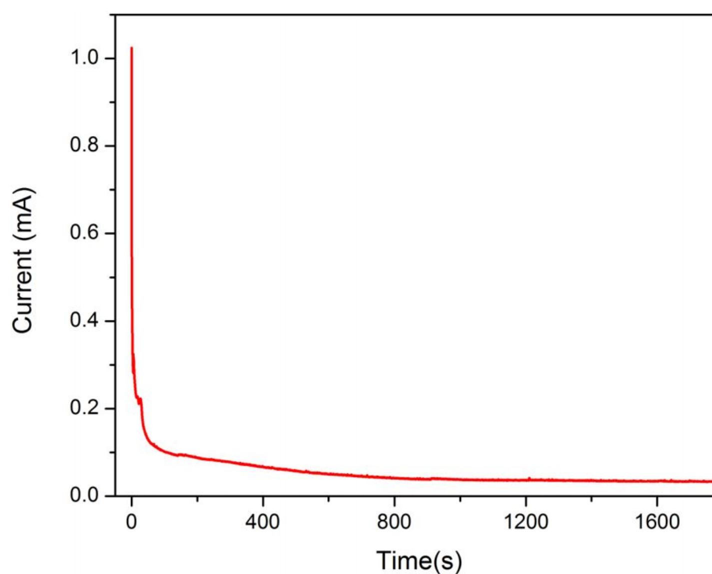

Figure S2. Photoelectrochemical oxidation of a 28 nm thick film of Au on Si sample under irradiation of light at 0.75 V *versus* Ag/AgCl in 0.5 M H_2SO_4 solution. The photocurrent gradually drops to near zero as the thickness of SiO_x increases.

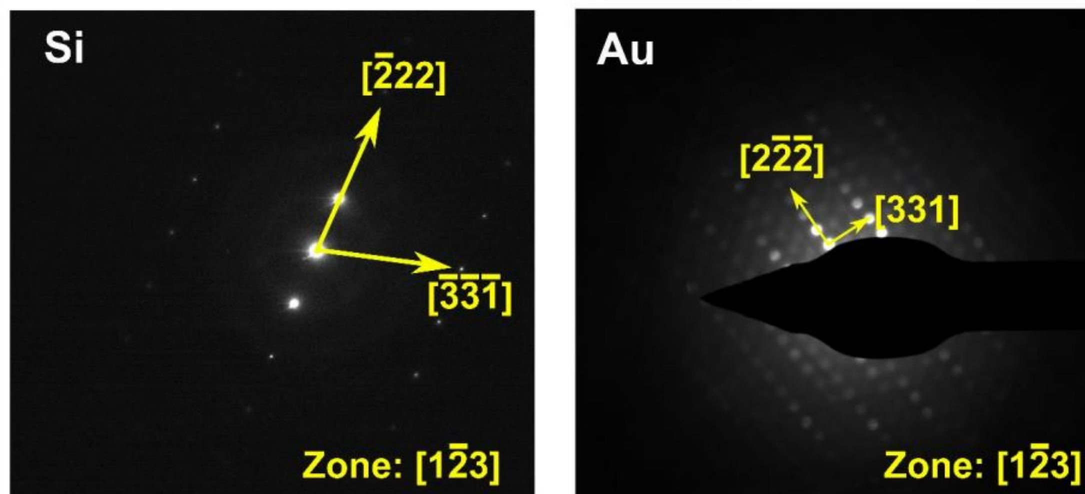

Figure S3. Electron diffraction pattern of Si and Au after photoelectrochemical oxidation at +0.75V in 0.5 M H_2SO_4 solution for 30 min. A spot pattern shows that the Au is still epitaxial with Si. The rotation in directions is due to the difference in camera length used to capture the patterns.

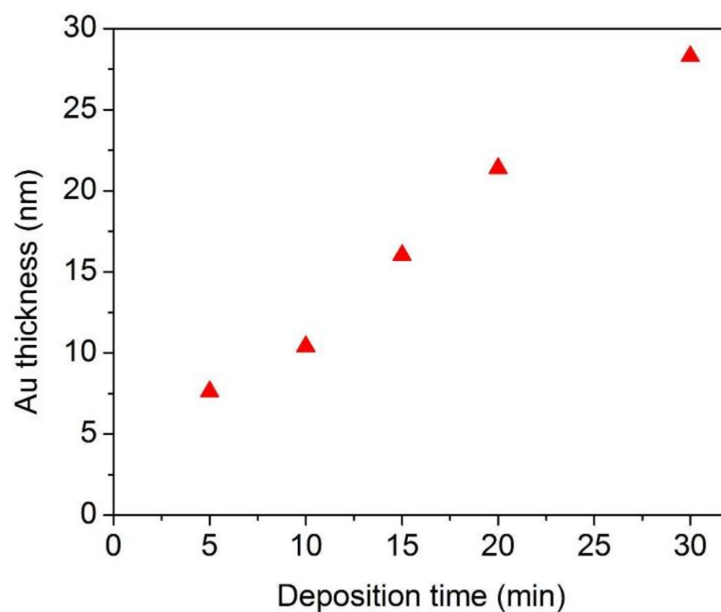

Figure S4. Thickness of Au on Si as a function of deposition time measured by Laue oscillations.

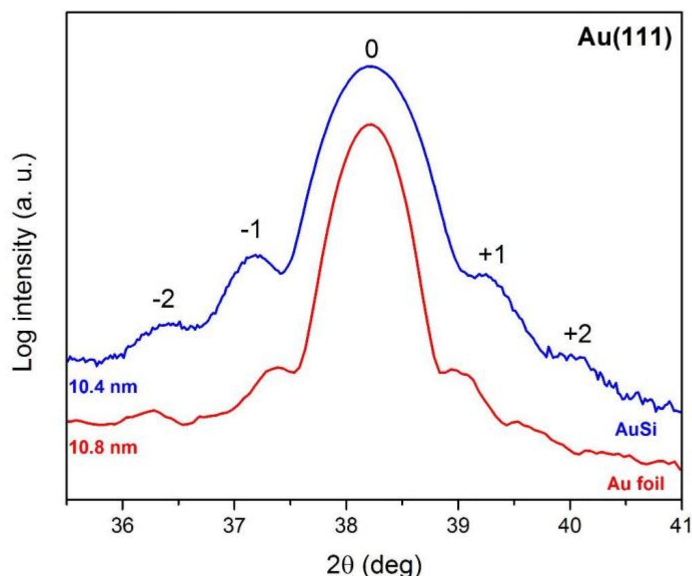

Figure S5. X-ray diffraction of a 10 nm Au on Si and a 10 nm Au foil showing Laue oscillations around the (111) Bragg peak. The measured thickness for Au on Si is in agreement with the thickness of the foil after separation. The foil was not produced from the Au film shown in the figure. It was produced from another film that was electrodeposited for the same amount of time.

X-ray rocking curves, azimuthal scans and pole figures are texture analysis tools for highly ordered crystalline materials. All of these scans require a 2θ angle fixed at the peak of interest. For example, $2\theta = 47.304°$ for probing the Si(220) planes. The sample stage is tilted or rotated in different directions and angles in order to determine the in-plane and out-of-plane order of the sample. Rocking the sample along the axis perpendicular to the source-sample-detector plane is known as the ω scan or rocking curve. Rocking curves determine the mosaic spread of the out-of-plane orientation. Rotation of the sample around the sample normal is the ϕ scan, or the azimuthal scan. Tilting the sample along the axis orthogonal to both the ω and the ϕ axes is the χ scan (or sometimes referred to as the ψ scan). Diffraction signals collected from the azimuthal scans (ϕ = 0° to 360°) at each tilt angle (χ = 0° to 90°) are used to construct a pole figure.

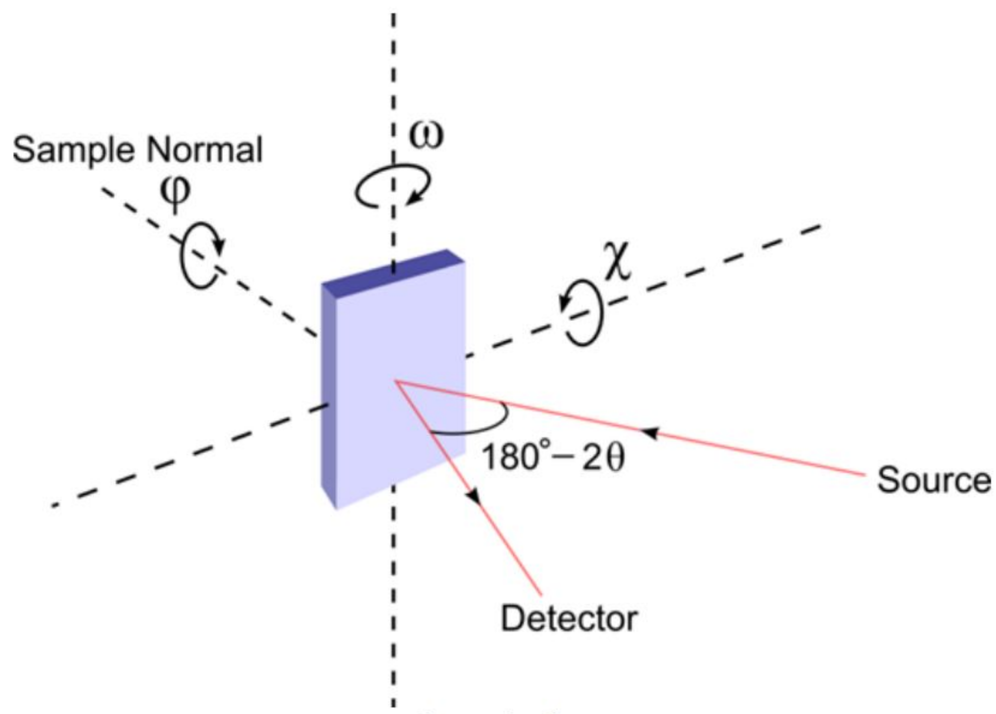

Figure S6. X-ray measurement geometry for pole figures.

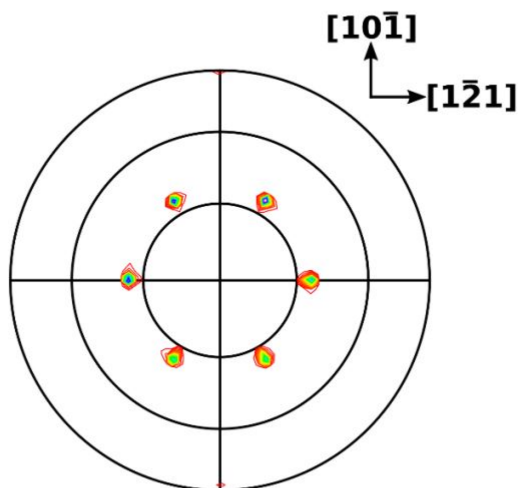

Figure S7. (220) pole figure of Au(111) on Si(111). Six spots corresponding to the parallel and anti-parallel domains at an expected tilt angle of 35.5 ° rotated azimuthally by 60°.

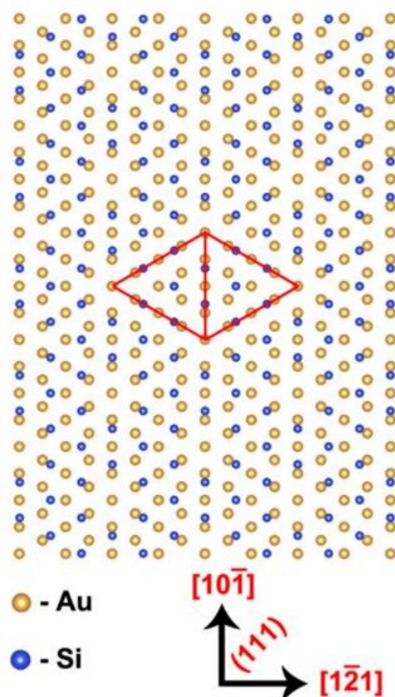

Figure S8. Interface model of Au(111) on Si(111) atoms. The coincidence lattice is shown in red lines forming two triangles rotated in-plane 180°. The lattice mismatch lowers from -24.9% for a 1$d_{Au(hkl)}$ x 1$d_{Si(hkl)}$ to +0.13% for the 4$d_{Au(hkl)}$ x 3$d_{Si(hkl)}$.

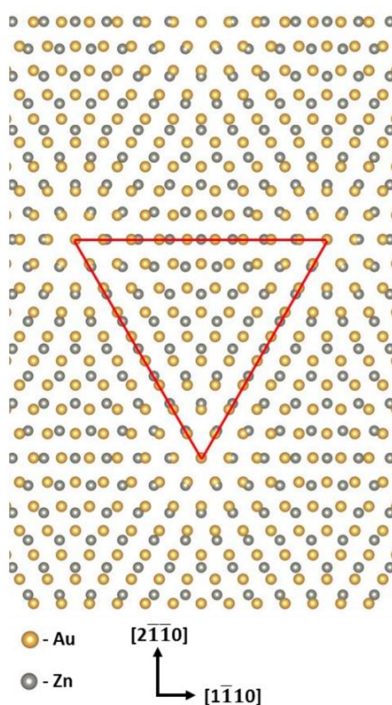

Figure S9. Interface model of Zn atoms of ZnO(0002) on Au(111). The lattice mismatch lowers from +12.7% for a 1$d_{Au(hkl)}$ x 1$d_{Zn(hkl)}$ to +0.16% for the 9$d_{Au(hkl)}$ x 8$d_{Si(hkl)}$.

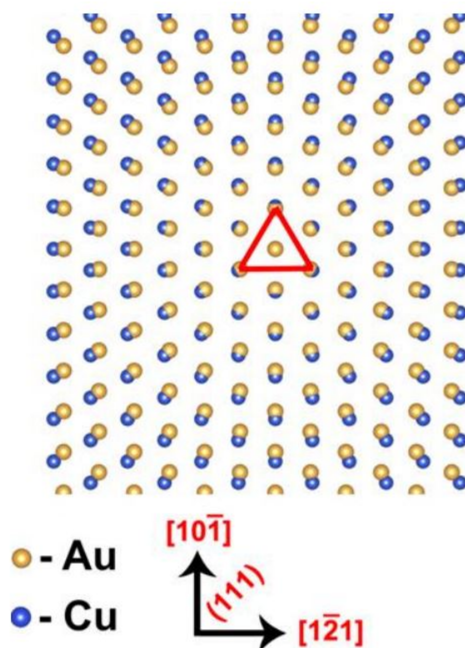

Figure S10. Interface model of Cu atoms of $Cu_2O(111)$ on Au(111). The lattice mismatch for a $1d_{Au(hkl)}$ x $1d_{Cu(hkl)}$ is +4.7%, which is low enough to form epitaxial deposits with moderate compressive in-plane strain and tensile out-of-plane strain.

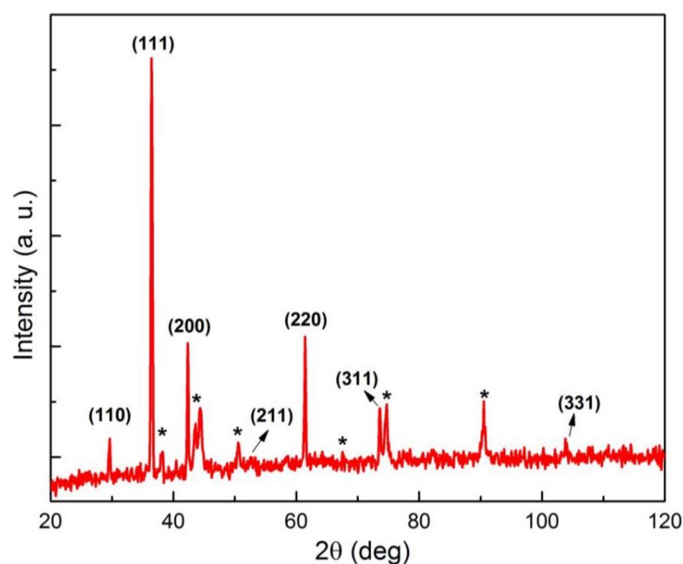

Figure S11. X-ray diffraction pattern of polycrystalline Cu_2O electrodeposited on a stainless-steel substrate to a charge density of 1.8 C cm^{-2}. The marked Miller indices represent Cu_2O peaks and the asterisks correspond to the stainless-steel substrate. The pattern indicates that the Cu_2O has a near-random crystallographic orientation.

ACKNOWLEDGEMENTS

The material is based on work supported by the U.S. Department of Energy, Office of Basic Sciences, Division of Materials Sciences and Engineering, under grants DE-FG02-08ER46518 (J.A.S.) and DE-SC0008799 (E.C.). All data are presented in the main paper and supplementary materials.

REFERENCES

1. B. D. Gates, Flexible electronics. *Science* **2009**, 323, 1566-1567.
2. J. C. Kenry, J. C. Yeo, C. T. Lim, Emerging flexible and wearable physical sensing platforms for healthcare and biomedical applications. *Microsyst. Nanoeng.* **2016**, 2, 16043.
3. D. Akinwande, N. Petrone, J. Hone, Two-dimensional flexible nanoelectronics. *Nat. Commun.* **2014**, 5, 5678.
4. J. A. Rogers, T. Someya, Y. Huang, Materials and mechanics for stretchable electronics. *Science* **2010**, 327, 1603-1607.
5. W. Gao, S. Emaminejad, H. Y. Y. Nyein, S. Challa, K. Chen, A. Peck, H. M. Fahad, H. Ota, H. Shiraki, D. Kiriya, D.-H. Lien, G. A. Brooks, R. W. Davis, A. Javey, Fully integrated wearable sensor arrays for multiplexed in situ perspiration analysis. *Nature* **2016**, 529, 509-514.
6. D. Shahrjerdi, S. W. Bedell, Extremely flexible nanoscale ultrathin body silicon integrated circuits on plastic. *Nano Lett.* **2013**, 13, 315-320.
7. J. Yoon, A. J. Baca, S.-I. Park, P. Elvikis, J. B. Geddes 3rd, L. Li, R. H. Kim, J. Xiao, S. Wang, T.-H. Kim, M. J. Motala, B. Y. Ahn, E. B. Duoss, J. A. Lewis, R. G. Nuzzo, P. M. Ferreira, Y. Huang, A. Rockett, J. A. Rogers, Ultrathin silicon solar microcells for semitransparent, mechanically flexible and microconcentrator module designs. *Nat. Mater.* **2008**, 7, 907-915.
8. S. Xu, Z. Yan, K.-I. Jang, W. Huang, H. Fu, J. Kim, Z. Wei, M. Flavin, J. McCracken, R. Wang, A. Badea, Y. Liu, D. Xiao, G. Zhou, J. Lee, H. U. Chung, H. Cheng, W. Ren, A. Banks, X. Li, U. Paik, R. G. Nuzzo, Y. Huang, Y. Zhang, J. A. Rogers, Assembly of micro/nanomaterials into complex, three-dimensional architectures by compressive buckling. *Science* **2015**, 347, 154-159.
9. T. Cheng, Y.-Z. Zhang, J.-D. Zhang, W.-Y. Lai, W. Huang, High-performance free-standing PEDOT:PSS electrodes for flexible and transparent all-solid-state supercapacitors. *J. Mater. Chem. A* **2016**, 4, 10493-10499.
10. D. M. Sun, M. Y. Timmermans, Y. Tian, A. G. Nasibulin, E. I. Kauppinen, S. Kishimoto, T. Mizutani, Y. Ohno, Flexible high-performance carbon nanotube integrated circuits. *Nat. Nanotechnol.* **2011**, 6, 156-161.
11. S. Bae, H. Kim, Y. Lee, X. Xu, J.-S. Park, Y. Zheng, J. Balakrishnan, T. Lei, H. R. Kim, Y. I. Song, Y.-J. Kim, K. S. Kim, B. Ozyilmaz, J.-H. Ahn, B. H. Hong, S. Iijima, Roll-to-roll production of 30-inch graphene films for transparent electrodes. *Nat. Nanotechnol.* **2010**, 5, 574-578.

12. W.-K. Kim, S. Lee, D. Hee Lee, I. Hee Park, J. Seong Bae, T. Woo Lee, J.-Y. Kim, J. Hun Park, Y. Chan Cho, C. Ryong Cho, S.-Y. Jeong, Cu mesh for flexible transparent conductive electrodes. *Sci. Rep.* **2015**, 5, 10715.

13. J. H. M. Maurer, L. Gonzalez-Garcia, B. Reiser, I. Kanelidis, T. Kraus, Templated self-assembly of ultrathin gold nanowires by nanoimprinting for transparent flexible electronics. *Nano Lett.* **2016**, 16, 2921-2925.

14. Y.-G. Bi, J. Feng, J.-H. Ji, Y. Chen, Y.-S. Liu, Y.-F. Li, Y.-F. Liu, X.-L. Zhang, H.-B. Sun, Ultrathin and ultrasmooth Au films as transparent electrodes in ITO-free organic light-emitting devices. *Nanoscale* **2016**, 8, 10010-10015.

15. B. O'Connor, C. Haughn, K.-H. An, K. P. Pipe, M. Shtein, Transparent and conductive electrodes based on unpatterned, thin metal films. *Appl. Phys. Lett.* **2008**, 93, 223304.

16. J. A. Koza, J. C. Hill, A. C. Demster, J. A. Switzer, Epitaxial electrodeposition of methylammonium lead iodide perovskites. *Chem. Mater.* **2016**, 28, 399-405.

17. J. W. Shin, A. Standley, E. Chason, Epitaxial electrodeposition of freestanding large area single crystal substrates. *Appl. Phys. Lett.* **2007**, 90, 261909.

18. S. Warren, P. Prod'homme, F. Maroun, P. Allongue, R. Cortes, C. Ferrero, T. L. Lee, B. C. C. Cowie, C. J. Walker, S. Ferrer, J. Zegenhagen, Electrochemical Au deposition on stepped Si(111)-H surfaces: 3D versus 2D growth studied by AFM and X-ray diffraction. *Surf. Sci.* **2009**, 603, 1212-1220.

19. P. Prod'homme, F. Maroun, R. Cortes, P. Allongue, Electrochemical growth of ultraflat Au(111) epitaxial buffer layers on H-Si(111). *Appl. Phys. Lett.* **2008**, 93, 171901.

20. J. A. Switzer, J. C. Hill, N. K. Mahenderkar, Y.-C. Liu, Nanometer-thick gold on silicon as a proxy for single-crystal gold for the electrodeposition of epitaxial cuprous oxide thin films. *ACS Appl. Mater. Interfaces* **2016**, 8, 15828-15837.

21. L. Jastrzebski, SOI by CVD: Epitaxial lateral overgrowth (ELO) process-review. *J. Cryst. Growth* **1983**, 63, 493-526.

22. G. B. Smith, G. A. Niklasson, J. S. E. M. Svensson, C. G. Granqvist, Noble-metal-based transparent infrared reflectors: Experiments and theoretical analyses for very thin gold films. *J. Appl. Phys.* **1986**, 59, 571-581.

23. D. N. Jarrett, L. Ward, Optical properties of discontinuous gold films. *J. Phys. D* **1976**, 9, 1515-1527.

24. M. Hövel, B. Gompf, M. Dressel, Dielectric properties of ultrathin metal films around the percolation threshold. *Phys. Rev. B* **2010**, 81, 035402.

25. O. S. Heavens, Optical properties of thin films. *Rep. Prog. Phys.* **1960**, 23, 1.

26. F. G. Gao, A. J. Bard, Solid-state organic light-emitting diodes based on tris(2,2"-bipyridine)ruthenium(II) complexes. *J. Am. Chem. Soc.* **2000**, 122, 7426-7427.

27. J. A. Broomhead, C. G. Young, P. Hood, Tris(2,2"-bipyridine)ruthenium(II) dichloride hexahydrate. *Inorg. Synth.* **2007**, 28, 338-340.

28. K. Sen, B. P. Tyagi, Diode quality factor in polycrystalline solar cells. *J. Appl. Phys.* **1984**, 56, 1240-1241.

29. S. Kumari, N. K. Arora, G. C. Jain, Grain size dependence of the photovoltaic properties of solar grade polysilicon. *Sol. Energy Mater.* **1981**, 5, 383-390.

30. R. J. Iwanowski, D. Trivich, Cu/Cu_2O Schottky barrier solar cells prepared by multistep irradiation of a Cu_2O substrate by H^+ ions. *Solar Cells* **1985**, 13, 253-264.

31. W. Wu, X. Wen, Z. L. Wang, Taxel-addressable matrix of vertical-nanowire piezotronic transistors for active and adaptive tactile imaging. *Science* **2013**, 340, 952-957.

32. C. Wang, R. Bao, K. Zhao, T. Zhang, L. Dong, C. Pan, Enhanced emission intensity of vertical aligned flexible ZnO nanowire/p-polymer hybridized LED array by piezo-phototronic effect. *Nano Energy* **2015**, 14, 364-371.

33. P. Poizot, C.-J. Hung, M. P. Nikiforov, E. W. Bohannan, J. A. Switzer, An electrochemical method for CuO thin film deposition from aqueous solution. *Electrochem. Solid-State Lett.* **2003**, 6, C21-C25.

34. S. Yazdanparast, J. A. Koza, J. A. Switzer, Copper nanofilament formation during unipolar resistance switching of electrodeposited cuprous oxide. *Chem. Mater.* **2015**, 27, 5974-5981.

35. R. Liu, A. A. Vertegel, E. W. Bohannan, T. A. Sorenson, J. A. Switzer, Epitaxial electrodeposition of zinc oxide nanopillars on single-crystal gold. *Chem. Mater.* **2001**, 13, 508-512.

36. M. Skompska, K. Zarebska, Electrodeposition of ZnO nanorod arrays on transparent conducting substrates-a review. *Electrochim. Acta* **2014**, 127, 467-488.

SECTION

2. CONCLUSIONS & FUTURE WORK

2.1. CONCLUSIONS

Current semiconductor industry uses Si as the standard for electronic applications due to its high crystalline perfection which helps minimize the electron-hole recombination, a dense SiO_x dielectric layer that helps lower the surface states and the abundance of SiO_2 in nature. However, with the fast-evolving field of flexible electronics, there is a need for new materials and fabrication techniques. The foldable, bendable and stretchable electronic devices demand functionality under high strain conditions,[1–2] which the conventional rigid Si architectures cannot withstand. There have been extensive studies on lab scale research for flexible devices such as smart skin sensors,[31] displays,[53] solar cells[180] and biomedical implants.[26,68] However, they lack the crystalline order that traditional Si substrates offers, which lowers the overall efficiency of the device.[14] The aim of this research is to fabricate semiconducting nanostrucutres and thin films using a simple benchtop electrochemical process.

Paper I introduces a simple one-step process for the direct electrodeposition of polycrystalline Ge nanowires on an indium-tin oxide (ITO) substrate from an aqueous solution. Ge is an attractive anode material for Li-ion batteries with a higher theoretical charge-discharge capacity (600-1140 mAh/g) compared to the traditionally used graphite (370 mAh/g). The single-step electrodeposition works due to the similarity in the reduction potential of ITO and Ge(IV), which decorates the substrate with In nanoparticles. The Ge nanowires grow on the In metal catalyst by dissolution and crystallization by the electro-

chemical liquid-liquid-solid (ec-LLS) mechanism. It is also shown that the diameter of the nanowire can be controlled using the deposition solution temperature.

Paper II describes nanometer-thick electrodeposition of epitaxial Au thin films on Si(111), Si(100) and Si(110) to serve as a proxy for single crystal Au. The thickness of the Au films can be controlled using the deposition time ranging from 7 nm for a 5 min deposit to 28 nm for a 30 min deposit. The requisite step for the epitaxial deposition of Au on Si from an aqueous solution was the prepolarization of Si substrate prior to the immersion in the electrolyte. This also enables the deposition of very smooth films required for the determination of thickness using low-angle x-ray reflectivity and Laue oscillations. Epitaxial Cu_2O is electrodeposited on all three orientations of Au/Si to demonstrate the applicability of the substrate as a proxy for single crystal. The outlined method is also applicable for the electrodeposition of a wide range of semiconductors and ceramic materials.

Paper III demonstrates the utilization of the wafer-scale epitaxial Au on Si thin films for the fabrication of wafer size foils of single crystal gold, which acts as a flexible, transparent, chemically inert, and highly ordered substrate to grow epitaxial inorganic semiconductors for flexible solar cells and LEDs. Single crystal Au costs about a US$ 1000 for 1 cm^2 which limits its practical application. However, a 28 nm thick Au foil with an area of 1 cm^2 costs about a penny to fabricate. The inexpensive fabrication and scalability of this process could help realize the improvement of efficiencies in flexible electronic devices. To evaluate the single crystal nature of Au foils, a Cu_2O inorganic diode is prepared by direct electrodeposition of Cu_2O from an aqueous solution. The epitaxial diode showed improved diode quality factor (n = 1.6) compared to a polycrystalline film (n = 3.1). The flexibility and transmittance of the the foil is evaluated by spin coating an organic light emitting diodes based on $Ru^{II}(bpy)_3$. Similar to the Au on Si substrates, Au foils can be used for the deposition of wide range of semiconductors such as CdTe, CdSe and ZnSe for

flexible electronic devices. Below the percolation threshold thickness, the Au films can also act as a fractal mesh providing superior optical transmission while maintaining electrical conductivity and crystallinity.

2.2. FUTURE WORK

2.2.1. Spin Coated Epitaxial Perovskite Thin Films on Au Foil.

Methylammonium lead iodide ($MAPbI_3$) is an inorganic-organic hybrid solar cell material with a record conversion efficiency exceeding 20%. Typically, this material is prepared by spin coating the organic and inorganic precursors dissolved in a non-aqueous solvent on a transparent conducting oxide substrate. The final product is usually polycrystalline which results in electron-hole recombination at the grain boundaries. Due to the inherent flexibility, $MAPbI_3$ is currently being studied as a promising candidate for flexible solar cells. Similar studies will also be performed on $CsPbBr_3$ all-inorganic stable perovskite material for light emitting diodes. The proposed work for epitaxial perovskite solar cells include:

1. Fabrication of epitaxial Au on Si and Au foil.
2. Epitaxial electrodeposition of p-type Cu_2O as a dense electron blocking layer which also acts as a hole transport layer.
3. Epitaxial spin coating of the perovskite on Cu_2O thin films.
4. Spin coating of an electron transport layer and top contact for solar cell or light emitting diode.

2.2.2. Electrodeposition of Epitaxial Ge Nanowires.

Ge is shown to electrodeposit on In nanoparticles, where the nanoparticles appear to be at the top of the nanowire. Because of polycrystalline indium-tin oxide, the electrochemically reduced In nanoparticles

also tend to be polycrystalline. To enable epitaxial growth of Ge, a single crystal substrate with epitaxial In nanoparticles are required. The proposed work for epitaxial growth of Ge nanowires includes:

1. Fabrication of a single crystal Au foil.
2. Epitaxial electrodeposition of In nanoparticles.
3. Epitaxial growth of Ge nanowires on Au foil.
4. Ge nanowire growth using other epitaxial nanoparticles such as Ga and InGa eutectic alloy.
5. Characterization of Ge nanowires as a function of flexibility.

BIBLIOGRAPHY

1. Gates, B. D. Flexible electronics. *Science* **2009**, 323, 1566-1567.

2. Rogers, J. A.; Someya, T.; Huang, Y. Materials and mechanics for stretchable electronics. *Science* **2010**, 327, 1603-1607.

3. Kenry; Yeo, J. C.; Lim, C. T. Emerging flexible and wearable physical sensing platforms for healthcare and biomedical applications. *Microsystems & Nanoengineering* **2016**, 2, 16043.

4. Akinwande, D.; Petrone, N.; Hone, J. Two-dimensional flexible nanoelectronics. *Nature Communications* **2014**, 5, 5678.

5. Gao, W.; Emaminejad, S.; Nyein, H. Y. Y.; Challa, S.; Chen, K.; Peck, A.; Fahad, H. M.; Ota, H.; Shiraki, H.; Kiriya, D.; Lien, D.-H.; Brooks, G. A.; Davis, R. W.; Javey, A. Fully integrated wearable sensor arrays for multiplexed in situ perspiration analysis. *Nature* **2016**, 529, 509-514.

6. Root, S. E.; Savagatrup, S.; Printz, A. D.; Rodriquez, D.; Lipomi, D. J. Mechanical Properties of Organic Semiconductors for Stretchable, Highly Flexible, and Mechanically Robust Electronics. *Chemical Reviews* **2017**, 117, 6467-6499.

7. Lee, S. M.; Kwon, J. H.; Kwon, S.; Choi, K. C. A Review of Flexible OLEDs Toward Highly Durable Unusual Displays. *IEEE Transactions on Electron Devices* **2017**, 64, 1922-1931.

8. Yun, J.; Wang, W.; Bae, T. S.; Park, Y. H.; Kang, Y.-C.; Kim, D.-H.; Lee, S.; Lee, G.-H.; Song, M.; Kang, J.-W. Preparation of Flexible Organic Solar Cells with Highly Conductive and Transparent Metal-Oxide Multilayer Electrodes Based on Silver Oxide. *ACS Applied Materials & Interfaces* **2013**, 5, 9933-9941.

9. Nathan, A.; Ahnood, A.; Cole, M. T.; Lee, S.; Suzuki, Y.; Hiralal, P.; Bonaccorso, F.; Hasan, T.; Garcia-Gancedo, L.; Dyadyusha, A.; Haque, S.; Andrew, P.; Hofmann, S.; Moultrie, J.; Chu, D.; Flewitt, A. J.; Ferrari, A. C.; Kelly, M. J.; Robertson, J.; Amaratunga, G. A. J.; Milne, W. I. Flexible Electronics: The Next Ubiquitous Platform. *Proceedings of the IEEE* **2012**, 100, 1486-1517.

10. Guilln, C.; Herrero, J. TCO/metal/TCO structures for energy and flexible electronics. *Thin Solid Films* **2011**, 520, 1-17.

11. Bi, Y.-G.; Feng, J.; Ji, J.-H.; Chen, Y.; Liu, Y.-S.; Li, Y.-F.; Liu, Y.-F.; Zhang, X.-L.; Sun, H.-B. Ultrathin and ultrasmooth Au films as transparent electrodes in ITO-free organic light-emitting devices. *Nanoscale* **2016**, 8, 10010-10015.

12. Lee, J.-Y.; Connor, S. T.; Cui, Y.; Peumans, P. Solution-Processed Metal Nanowire Mesh Transparent Electrodes. *Nano Letters* **2008**, 8, 689-692.

13. Elschner, A.; Kirchmeyer, S.; Lovenich, W.; Merker, U.; Reuter, K. PEDOT: principles and applications of an intrinsically conductive polymer. *CRC Press*: 2010.

14. Koza, J. A.; Hill, J. C.; Demster, A. C.; Switzer, J. A. Epitaxial electrodeposition of methylammonium lead iodide perovskites. *Chemistry of Materials* **2016**, 28, 399-405.

15. Mahenderkar, N. K.; Liu, Y.-C.; Koza, J. A.; Switzer, J. A. Electrodeposited Germanium Nanowires. *ACS Nano* **2014**, 8, 9524-9530.

16. Switzer, J. A.; Hill, J. C.; Mahenderkar, N. K.; Liu, Y.-C. Nanometer-thick gold on silicon as a proxy for single-crystal gold for the electrodeposition of epitaxial cuprous oxide thin films. *ACS Applied Materials & Interfaces* **2016**, 8, 15828-15837.

17. Chen, Q.; Switzer, J. A. Photoelectrochemistry of Ultrathin, Semitransparent, and Catalytic Gold Films Electrodeposited Epitaxially onto n-Silicon(111). *ACS Applied Materials & Interfaces* **2018**.

18. Mahenderkar, N. K.; Chen, Q.; Liu, Y.-C.; Duchild, A. R.; Hofheins, S.; Chason, E.; Switzer, J. A. Epitaxial lift-off of electrodeposited single-crystal gold foils for flexible electronics. *Science* **2017**, 355, 1203-1206.

19. Tao, C.; Yizhou, Z.; Wen-Yong, L.; Wei, H. Stretchable Thin-Film Electrodes for Flexible Electronics with High Deformability and Stretchability. *Advanced Materials* **2015**, 27, 3349-3376.

20. Y., S.; A., R. J. Inorganic Semiconductors for Flexible Electronics. *Advanced Materials* **2007**, 19, 1897-1916.

21. Zhang, W.; Dehghani-Sanij, A. A.; Blackburn, R. S. Carbon based conductive polymer composites. *Journal of Materials Science* **2007**, 42, 3408-3418.

22. Hu, L.; Kim, H. S.; Lee, J.-Y.; Peumans, P.; Cui, Y. Scalable Coating and Properties of Transparent, Flexible, Silver Nanowire Electrodes. *ACS Nano* **2010**, 4, 2955-2963.

23. Park, S.; Vosguerichian, M.; Bao, Z. A review of fabrication and applications of carbon nanotube film-based flexible electronics. *Nanoscale* **2013**, 5, 1727-1752.

24. Zardetto, V.; Brown, T. M.; Reale, A.; Di Carlo, A. Substrates for flexible electronics: A practical investigation on the electrical, film flexibility, optical, temperature, and solvent resistance properties. *Journal of Polymer Science Part B: Polymer Physics* **2011**, 49, 638-648.

25. Toivola, M.; Halme, J.; Miettunen, K.; Aitola, K.; Lund, P. D. Nanostructured dye solar cells on flexible substrates-Review. *International Journal of Energy Research* **2009**, 33, 1145-1160.

26. Lipomi, D. J.; Bao, Z. Stretchable, elastic materials and devices for solar energy conversion. *Energy & Environmental Science* **2011**, 4, 3314-3328.

27. Hecht, D. S.; Kaner, R. B. Solution-processed transparent electrodes. *MRS Bulletin* **2011**, 36, 749-755.

28. Snook, G. A.; Kao, P.; Best, A. S. Conducting-polymer-based supercapacitor devices and electrodes. *Journal of Power Sources* **2011**, 196, 1-12.

29. Bhadra, S.; Khastgir, D.; Singha, N. K.; Lee, J. H. Progress in preparation, processing and applications of polyaniline. *Progress in Polymer Science* **2009**, 34, 783-810.

30. Heeger, A. J. Nobel Lecture: Semiconducting and metallic polymers: The fourth generation of polymeric materials. *Reviews of Modern Physics* **2001**, 73, 681-700.

31. Benight, S. J.; Wang, C.; Tok, J. B. H.; Bao, Z. Stretchable and self-healing polymers and devices for electronic skin. *Progress in Polymer Science* **2013**, 38, 1961-1977.

32. Nyholm, L.; Nystrm, G.; Mihranyan, A.; Stromme, M. Toward Flexible Polymer and Paper-Based Energy Storage Devices. *Advanced Materials* **2011**, 23, 3751-3769.

33. Huang, J.-C. Carbon black filled conducting polymers and polymer blends. *Advances in Polymer Technology* **2002**, 21, 299-313.

34. Strumpler, R.; Glatz-Reichenbach, Conducting Polymer Composites. *Journal of Electroceramics* **1999**, 3, 329-346.

35. Kim, D.-J.; Kim, H.-J.; Seo, K.-W.; Kim, K.-H.; Kim, T.-W.; Kim, H.-K. Indium-free, highly transparent, flexible Cu_2O/Cu/Cu_2O mesh electrodes for flexible touch screen panels. *Scientific Reports* **2015**, 5, 16838.

36. Maurer, J. H. M.; Gonzalez-Garcia, L.; Reiser, B.; Kanelidis, I.; Kraus, T. Templated self-assembly of ultrathin gold nanowires by nanoimprinting for transparent flexible electronics. *Nano Letters* **2016**, 16, 2921-2925.

37. Zhao, Y.-F.; Zou, W.-J.; Li, H.; Lu, K.; Yan, W.; Wei, Z.-X. Large-area, flexible polymer solar cell based on silver nanowires as transparent electrode by roll-to-roll printing. *Chinese Journal of Polymer Science* **2017**, 35, 261-268.

38. Xia, M.; Cheng, Z.; Han, J.; Zhang, S. Extremely stretchable all-carbon-nanotube transistor on flexible and transparent substrates. *Applied Physics Letters* **2014**, 105, 143504.

39. Lonne, Q.; Endrino, J.; Huang, Z. UV Treatment of Flexible Copper Nanowire Mesh Films for Transparent Conductor Applications. *Nanoscale Research Letters* **2017**, 12, 577.

40. O'Connor, B.; Haughn, C.; An, K.-H.; Pipe, K. P.; Shtein, M. Transparent and conductive electrodes based on unpatterned, thin metal films. *Applied Physics Letters* **2008**, 93, 223304.

41. Fortunato, G.; Pecora, A.; Maiolo, L. Polysilicon thin-film transistors on polymer substrates. *Materials Science in Semiconductor Processing* **2012**, 15, 627-641.

42. Tobjrk, D.; sterbacka, R. Paper Electronics. *Advanced Materials* **2011**, 23, 1935-1961.

43. Hu, L.; Cui, Y. Energy and environmental nanotechnology in conductive paper and textiles. *Energy & Environmental Science* **2012**, 5, 6423-6435.

44. Park, S.; Jayaraman, S. Smart Textiles: Wearable Electronic Systems. *MRS Bulletin* **2011**, 28, 585-591.

45. Salvado, R.; Loss, C.; Goncalves, R.; Pinho, P. Textile Materials for the Design of Wearable Antennas: A Survey. *Sensors* **2012**, 12, 15841.

46. Zeng, W.; Shu, L.; Li, Q.; Chen, S.; Wang, F.; Tao, X.-M. Fiber-Based Wearable Electronics: A Review of Materials, Fabrication, Devices, and Applications. *Advanced Materials* **2014**, 26, 5310-5336.

47. Hu, L.; Pasta, M.; La Mantia, F.; Cui, L.; Jeong, S.; Deshazer, H. D.; Choi, J. W.; Han, S. M.; Cui, Y. Stretchable, Porous, and Conductive Energy Textiles. *Nano Letters* **2010**, 10, 708-714.

48. Campbell, S. A. The Science and Engineering of Microelectronic Fabrication (The Oxford Series in Electrical and Computer Engineering). **2001**.

49. Alf, M. E.; Asatekin, A.; Barr, M. C.; Baxamusa, S. H.; Chelawat, H.; Ozaydin-Ince, G.; Petruczok, C. D.; Sreenivasan, R.; Tenhaeff, W. E.; Trujillo, N. J. Chemical vapor deposition of conformal, functional, and responsive polymer films. *Advanced Materials* **2010**, 22, 1993-2027.

50. Kim, H.; Maeng, W.-J. Applications of atomic layer deposition to nanofabrication and emerging nanodevices. *Thin Solid Films* **2009**, 517, 2563-2580.

51. Knez, M.; Nielsch, K.; Niinisto, L. Synthesis and surface engineering of complex nanostructures by atomic layer deposition. *Advanced Materials* **2007**, 19, 3425-3438.

52. Guedes, A. F. S.; Guedes, V. P.; Tartari, S.; Cunha, I. J. In The application of electrodeposition in thin film transistors for flexible organic electronics, *28th Symposium on Microelectronics Technology and Devices* **2013**, 1-2.

53. Jain, K.; Klosner, M.; Zemel, M.; Raghunandan, S. Flexible electronics and displays: high-resolution, roll-to-roll, projection lithography and photoablation processing technologies for high-throughput production. *Proceedings of the IEEE* **2005**, 93, 1500-1510.

54. Krebs, F. C.; Gevorgyan, S. A.; Alstrup, J. A roll-to-roll process to flexible polymer solar cells: model studies, manufacture and operational stability studies. *Journal of Materials Chemistry* **2009**, 19, 5442-5451.

55. Krebs, F. C. Polymer solar cell modules prepared using roll-to-roll methods: knife-over-edge coating, slot-die coating and screen printing. *Solar Energy Materials and Solar Cells* **2009**, 93, 465-475.

56. Moonen, P. F.; Yakimets, I.; Huskens, J. Fabrication of transistors on flexible substrates: from mass-printing to high-resolution alternative lithography strategies. *Advanced materials* **2012**, 24, 5526-5541.

57. Kukla, R.; Ludwig, R.; Meinel, J. Overview on modern vacuum web coating technology. *Surface and Coatings Technology* **1996**, 86, 753-761.

58. Juang, Z.-Y.; Wu, C.-Y.; Lu, A.-Y.; Su, C.-Y.; Leou, K.-C.; Chen, F.-R.; Tsai, C.-H. Graphene synthesis by chemical vapor deposition and transfer by a roll-to-roll process. *Carbon* **2010**, 48, 3169-3174.

59. Ludwig, R.; Kukla, R.; Josephson, E. Vacuum web coating-state of the art and potential for electronics. *Proceedings of the IEEE* **2005**, 93, 1483-1490.

60. Reinhold, E.; Faber, J. Large area electron beam physical vapor deposition (EB-PVD) and plasma activated electron beam (EB) evaporation-Status and prospects. *Surface and coatings technology* **2011**, 206, 1653-1659.

61. Treutlein, R.; Bergsmann, M.; Stonley, C. J. Reel-to-reel Vacuum Metallization. *Organic Electronics: Materials, Manufacturing and Applications* **2006**, 181-202.

62. Li, L.; Zhang, S.; Yang, Z.; Berthold, E. E. S.; Chen, W. Recent advances of flexible perovskite solar cells. *Journal of Energy Chemistry* **2018**, 27, 673-689.

63. Rakhshani, A. E.; Thomas, S. Cu_2ZnSnS_4 Films Grown on Flexible Substrates by Dip Coating Using a Methanol-Based Solution: Electronic Properties and Devices. *Journal of Electronic Materials* **2015**, 44, 4760-4768.

64. Tait, J. G.; Worfolk, B. J.; Maloney, S. A.; Hauger, T. C.; Elias, A. L.; Buriak, J. M.; Harris, K. D. Spray coated high-conductivity PEDOT: PSS transparent electrodes for stretchable and mechanically-robust organic solar cells. *Solar Energy Materials and Solar Cells* **2013**, 110, 98-106.

65. Choi, D. Y.; Kang, H. W.; Sung, H. J.; Kim, S. S. Annealing-free, flexible silver nanowire-polymer composite electrodes via a continuous two-step spray-coating method. *Nanoscale* **2013**, 5, 977-983.

66. Keum, H.; Chung, H.-J.; Kim, S. Electrical contact at the interface between silicon and transfer-printed gold films by eutectic joining. *ACS applied materials interfaces* **2013**, 5, 6061-6065.

67. Keum, H.; Carlson, A.; Ning, H.; Mihi, A.; Eisenhaure, J. D.; Braun, P. V.; Rogers, J. A.; Kim, S. Silicon micro-masonry using elastomeric stamps for three-dimensional microfabrication. *Journal of Micromechanics and Microengineering* **2012**, 22, 055018.

68. Kim, D.-H.; Ghaffari, R.; Lu, N.; Rogers, J. A. Flexible and stretchable electronics for biointegrated devices. *Annual review of biomedical engineering* **2012**, 14, 113-128.

69. Nam, G. M.; Kwon, M. S. F-doped ZnO by sol-gel spin-coating as a transparent conducting thin film. *Electronic Materials Letters* **2011**, 7, 127-131.

70. Hsu, J. W. P. Soft lithography contacts to organics. *Materials Today* **2005**, 8, 42-54.

71. Street, R. A.; Wong, W.; Ready, S.; Chabinyc, M.; Arias, A.; Limb, S.; Salleo, A.; Lujan, R. Jet printing flexible displays. *Materials Today* **2006**, 9, 32-37.

72. Yin, Z.; Huang, Y.; Bu, N.; Wang, X.; Xiong, Y. Inkjet printing for flexible electronics: Materials, processes and equipments. *Chinese Science Bulletin* **2010**, 55, 3383-3407.

73. Arnold, C. B.; Serra, P.; Pique, A. Laser Direct-Write Techniques for Printing of Complex Materials. *MRS Bulletin* **2011**, 32, 23-31.

74. Kadekar, V.; Fang, W.; Liou, F. Deposition Technologies For Micromanufacturing: A Review. *Journal of Manufacturing Science and Engineering* **2005**, 126, 787-795.

75. Muth, J. T.; Vogt, D. M.; Truby, R. L.; Yigit, M.; Kolesky, D. B.; Wood, R. J.; Lewis, J. A. Embedded 3D Printing of Strain Sensors within Highly Stretchable Elastomers. *Advanced Materials* **2014**, 26, 6307-6312.

76. Ahn, B. Y.; Duoss, E. B.; Motala, M. J.; Guo, X.; Park, S.-I.; Xiong, Y.; Yoon, J.; Nuzzo, R. G.; Rogers, J. A.; Lewis, J. A. Omnidirectional Printing of Flexible, Stretchable, and Spanning Silver Microelectrodes. *Science* **2009**, 323, 1590-1593.

77. Yu, J.; Huang, B.; Qin, X.; Zhang, X.; Wang, Z.; Liu, H. Hydrothermal synthesis and characterization of ZnO films with different nanostructures. *Applied Surface Science* **2011**, 257, 5563-5565.

78. Fujita, M.; Kawamoto, N.; Sasajima, M.; Horikoshi, Y. Molecular beam epitaxy growth of ZnO using initial Zn layer and MgO buffer layer on Si(111) substrates. *Journal of Vacuum Science & Technology B: Microelectronics and Nanometer Structures Processing, Measurement, and Phenomena* **2004**, 22, 1484-1486.

79. Villanueva, Y. Y.; Liu, D.-R.; Cheng, P. T. Pulsed laser deposition of zinc oxide. *Thin Solid Films* **2006**, 501, 366-369.

80. Liu, R.; Vertegel, A. A.; Bohannan, E. W.; Sorenson, T. A.; Switzer, J. A. Epitaxial electrodeposition of zinc oxide nanopillars on single-crystal gold. *Chemistry of Materials* **2001**, 13, 508-512.

81. Limmer, S. J.; Kulp, E. A.; Switzer, J. A. Epitaxial Electrodeposition of ZnO on Au(111) from Alkaline Solution: Exploiting Amphoterism in Zn(II). *Langmuir* **2006**, 22, 10535-10539.

82. Zhou, Y.; Switzer, J. Electrochemical Deposition and Microstructure of Copper (I) Oxide Films. *Scripta Materialia* **1998** 38, 1731-1738.

83. Switzer, J. A.; Kothari, H. M.; Bohannan, E. W. Thermodynamic to Kinetic Transition in Epitaxial Electrodeposition. *The Journal of Physical Chemistry B* **2002**, 106, 4027-4031.

84. Liu, R.; Bohannan, E. W.; Switzer, J. A.; Oba, F.; Ernst, F. Epitaxial electrodeposition of Cu2O films onto InP(001). *Applied Physics Letters* **2003**, 83, 1944-1946.

85. Yazdanparast, S. Parameters controlling microstructures and resistance switching of electrodeposited cuprous oxide thin films. *Applied Surface Science* **2016**, 389, 632-638.

86. Poizot, P.; Hung, C.-J.; Nikiforov, M. P.; Bohannan, E. W.; Switzer, J. A. An electrochemical method for CuO thin film deposition from aqueous solution. *Electrochemical and Solid State Letters* **2003**, 6, C21-C25.

87. Switzer, J. A. Electrochemical architecture of ceramic nanocomposites. *Nanostructured Materials* **1992**, 1, 43-46.

88. Liu, R.; Oba, F.; Bohannan, E. W.; Ernst, F.; Switzer, J. A. Shape Control in Epitaxial Electrodeposition: Cu_2O Nanocubes on InP(001). *Chemistry of Materials* **2003**, 15, 4882-4885.

89. Koza, J. A.; Hull, C. M.; Liu, Y.-C.; Switzer, J. A. Deposition of β-$Co(OH)_2$ Films by Electrochemical Reduction of Tris(ethylenediamine)cobalt(III) in Alkaline Solution. *Chemistry of Materials* **2013**, 25, 1922-1926.

90. Koza, J. A.; He, Z.; Miller, A. S.; Switzer, J. A. Electrodeposition of Crystalline Co_3O_4-A Catalyst for the Oxygen Evolution Reaction. *Chemistry of Materials* **2012**, 24, 3567-3573.

91. Prod'homme, P.; Maroun, F.; Cortes, R.; Allongue, P. Electrochemical growth of ultraflat Au(111) epitaxial buffer layers on H-Si(111). *Applied Physics Letters* **2008**, 93, 171901.

92. Warren, S.; Prod'homme, P.; Maroun, F.; Allongue, P.; Cortes, R.; Ferrero, C.; Lee, T. L.; Cowie, B. C. C.; Walker, C. J.; Ferrer, S.; Zegenhagen, J. Electrochemical Au deposition on stepped Si(111)-H surfaces: 3D versus 2D growth studied by AFM and X-ray diffraction. *Surface Science* **2009**, 603, 1212-1220.

93. Prod'homme, P.; Maroun, F.; Cortes, R.; Allongue, P. Electrochemical growth of ultraflat Au(111) epitaxial buffer layers on H-Si(111). *Applied Physics Letters* **2008**, 93, 171901.

94. Liu, Z.; Xu, J.; Chen, D.; Shen, G. Flexible electronics based on inorganic nanowires. *Chemical Society Reviews* **2015**, 44, 161-192.

95. Xue, J.; Song, J.; Dong, Y.; Xu, L.; Li, J.; Zeng, H. Nanowire-based transparent conductors for flexible electronics and optoelectronics. *Science Bulletin* **2017**, 62, 143-156.

96. Lee, C. H.; Kim, D. R.; Zheng, X. Fabrication of Nanowire Electronics on Nonconventional Substrates by Water-Assisted Transfer Printing Method. *Nano Letters* **2011**, 11, 3435-3439.

97. Shuai, X.; Zhu, P.; Zeng, W.; Hu, Y.; Liang, X.; Zhang, Y.; Sun, R.; Wong, C.-p. Highly Sensitive Flexible Pressure Sensor Based on Silver Nanowires-Embedded Polydimethylsiloxane Electrode with Microarray Structure. *ACS Applied Materials & Interfaces* **2017**, 9, 26314-26324.

98. Chen, B.; Wu, H.; Xin, C.; Dai, D.; Tong, L. Flexible integration of free-standing nanowires into silicon photonics. *Nature Communications* **2017**, 8, 20.

99. McAlpine, M. C.; Friedman, R. S.; Lieber, C. M. High-Performance Nanowire Electronics and Photonics and Nanoscale Patterning on Flexible Plastic Substrates. *Proceedings of the IEEE* **2005**, 93, 1357-1363.

100. Han, N.; Yang, Z.-x.; Wang, F.; Dong, G.; Yip, S.; Liang, X.; Hung, T. F.; Chen, Y.; Ho, J. C. High-Performance GaAs Nanowire Solar Cells for Flexible and Transparent Photovoltaics. *ACS Applied Materials & Interfaces* **2015**, 7, 20454-20459.

101. Maiolo, J. R.; Kayes, B. M.; Filler, M. A.; Putnam, M. C.; Kelzenberg, M. D.; Atwater, H. A.; Lewis, N. S. High Aspect Ratio Silicon Wire Array Photoelectrochemical Cells. *Journal of the American Chemical Society* **2007**, 129, 12346-12347.

102. Jiu, J.; Suganuma, K. Metallic Nanowires and Their Application. *IEEE Transactions on Components, Packaging and Manufacturing Technology* **2016**, 6, 1733-1751.

103. Dasgupta, N. P.; Jianwei, S.; Chong, L.; Sarah, B.; Andrews, S. C.; Jongwoo, L.; Hanwei, G.; Ruoxue, Y.; Peidong, Y. 25th Anniversary Article: Semiconductor Nanowires - Synthesis, Characterization, and Applications. *Advanced Materials* **2014**, 26, 2137-2184.

104. Liu, Y.; Ma, Z.; Zhao, Y.-F.; Meenakshi, S.; Wang, J. Transport properties of topological insulators films and nanowires. *Chinese Physics B* **2013**, 22, 067302.

105. An, X.; Meng, G.; Wei, Q.; Kong, M.; Zhang, L. SiO_2 Nanowires Growing on Hexagonally Arranged Circular Patterns Surrounded by TiO_2 Films. *The Journal of Physical Chemistry B* **2006**, 110, 222-226.

106. Wang, X.; Li, Z.; Shi, J.; Yu, Y. One-Dimensional Titanium Dioxide Nanomaterials: Nanowires, Nanorods, and Nanobelts. *Chemical Reviews* **2014**, 114, 9346-9384.

107. Hobbs, R. G.; Petkov, N.; Holmes, J. D. Semiconductor Nanowire Fabrication by Bottom-Up and Top-Down Paradigms. *Chemistry of Materials* **2012**, 24, 1975-1991.

108. Schnenberger, C.; van der Zande, B. M. I.; Fokkink, L. G. J.; Henny, M.; Schmid, C.; Kruger, M.; Bachtold, A.; Huber, R.; Birk, H.; Staufer, U. Template Synthesis of Nanowires in Porous Polycarbonate Membranes: Electrochemistry and Morphology. *The Journal of Physical Chemistry B* **1997**, 101, 5497-5505.

109. Lee, W.; Park, S.-J. Porous Anodic Aluminum Oxide: Anodization and Templated Synthesis of Functional Nanostructures. *Chemical Reviews* **2014**, 114, 7487-7556.

110. Rathi, S. J.; Smith, D. J.; Drucker, J. Guided VLS Growth of Epitaxial Lateral Si Nanowires. *Nano Letters* **2013**, 13, 3878-3883.

111. Christiansen, S.; Schneider, R.; Scholz, R.; Gosele, U.; Stelzner, T.; Andra, G.; Wendler, E.; Wesch, W. Vapor-liquid-solid growth of silicon nanowires by chemical vapor deposition on implanted templates. *Journal of Applied Physics* **2006**, 100, 084323.

112. Alivisatos, A. P. Semiconductor Clusters, Nanocrystals, and Quantum Dots. *Science* **1996**, 271, 933-937.

113. Yan, Z.; Teng, Q.; Wenjun, Z.; Paul, K. C. Recent Progress in Patterned Silicon Nanowire Arrays: Fabrication, Properties and Applications. *Recent Patents on Nanotechnology* **2011**, 5, 62-70.

114. Liang, L.; Xincun, D.; Guanghai, L. Semimetal Nanowires and their Superlattices in Anodic Alumina Membranes. *Recent Patents on Nanotechnology* **2010**, 4, 181-193.

115. Jo, M. H.; Woo, Y.; Lee, G. H. Method and apparatus for manufacturing a nanowire. *Google Patents* **2016**.

116. Li, Z. P.; Zheng, Y. C. A Review on Germanium Nanowires. *Recent Patents on Nanotechnology* **2012**, 6, 44-59.

117. Chui, C. O.; Ramanathan, S.; Triplett, B. B.; McIntyre, P. C.; Saraswat, K. C. Germanium MOS capacitors incorporating ultrathin high-κ gate dielectric. *IEEE Electron Device Letters* **2002**, 23, 473-475.

118. Maeda, T.; Ikeda, K.; Nakaharai, S.; Tezuka, T.; Sugiyama, N.; Moriyama, Y.; Takagi, S. High mobility Ge-on-insulator p-channel MOSFETs using Pt germanide schottky source/drain. *IEEE Electron Device Letters* **2005**, 26, 102-104.

119. Bojarczuk, N. A.; Copel, M.; Guha, S.; Narayanan, V.; Preisler, E. J.; Ross, F. M.; Shang, H. Epitaxial silicon and germanium on buried insulator heterostructures and devices. *Applied Physics Letters* **2003**, 83, 5443-5445.

120. Morales, A. M.; Lieber, C. M. A Laser Ablation Method for the Synthesis of Crystalline Semiconductor Nanowires. *Science* **1998**, 279, 208-211.

121. Marolop, S.; Koichi, U.; Tetsuo, K.; Ken, U.; Shunri, O. Growth of Narrow and Straight Germanium Nanowires by Vapor-Liquid-Solid Chemical Vapor Deposition. *Japanese Journal of Applied Physics* **2011**, 50, 105002.

122. Araujo, L. S.; Kamimura, H.; Berengue, O. M.; Chiquito, A. J. Electrical and Structural Characterization of Germanium Nanowires. *Physics Procedia* **2012**, 28, 62-66.

123. Hanrath, T.; Korgel, B. A. Supercritical Fluid-Liquid-Solid (SFLS) Synthesis of Si and Ge Nanowires Seeded by Colloidal Metal Nanocrystals. *Advanced Materials* **2003**, 15, 437-440.

124. Hall, J. I.; Koenig, A. E. Electrochemical Properties of Germanium. *Transactions of The Electrochemical Society* **1934**, 65, 215-219.

125. Szekely, G. Electrodeposition of Germanium. *Journal of The Electrochemical Society* **1951**, 98, 318-324.

126. Liang, X.; Jayaraju, N.; Stickney, J. L. Aqueous Ge Atomic Layer Deposition on Au. *ECS Transactions* **2007**, 11, 249-258.

127. Liang, X.; Kim, Y.-G.; Gebergziabiher, D. K.; Stickney, J. L. Aqueous Electrodeposition of Ge Monolayers. *Langmuir* **2010**, 26, 2877-2884.

128. Kalyani, N.; Abdul Faheem, K.; Nasrudin, A. R. Electrodeposited Ge Nanostructures Prepared by Different Non-Aqueous Solutions and their Application in Lithium Ion Battery: A Review. *Recent Patents on Nanotechnology* **2016**, 10, 26-43.

129. DeMuth, J.; Ma, L.; Lancaster, M.; Acharya, S.; Cheek, Q.; Maldonado, S. Eutectic-Bismuth Indium as a Growth Solvent for the Electrochemical Liquid-Liquid-Solid Deposition of Germanium Microwires and Coiled Nanowires. *Crystal Growth & Design* **2018**, 18, 677-685.

130. Ma, L.; Fahrenkrug, E.; Gerber, E.; Crowe, A. J.; Venable, F.; Bartlett, B. M.; Maldonado, S. High-Performance Polycrystalline Ge Microwire Film Anodes for Li Ion Batteries. *ACS Energy Letters* **2017**, 2, 238-243.

131. DeMuth, J.; Fahrenkrug, E.; Maldonado, S. Controlling Nucleation and Crystal Growth of Ge in a Liquid Metal Solvent. *Crystal Growth & Design* **2016**, 16, 7130-7138.

132. Zhang, T.; Fahrenkrug, E.; Maldonado, S. Electrochemical Liquid-Liquid-Solid Deposition of Ge at Hg Microdroplet Ultramicroelectrodes. *Journal of The Electrochemical Society* **2016**, 163, D500-D505.

133. Ma, L.; Gu, J.; Fahrenkrug, E.; Maldonado, S. Electrochemical Liquid-Liquid-Solid Deposition of Crystalline Ge Nanowires as a Function of Ga Nanodroplet Size. *Journal of The Electrochemical Society* **2014**, 161, D3044-D3050.

134. Fahrenkrug, E.; Gu, J.; Jeon, S.; Veneman, P. A.; Goldman, R. S.; Maldonado, S. Room-Temperature Epitaxial Electrodeposition of Single-Crystalline Germanium Nanowires at the Wafer Scale from an Aqueous Solution. *Nano Letters* **2014**, 14, 847-852.

135. Gu, J.; Collins, S. M.; Carim, A. I.; Hao, X.; Bartlett, B. M.; Maldonado, S. Template-Free Preparation of Crystalline Ge Nanowire Film Electrodes via an Electrochemical Liquid-Liquid-Solid Process in Water at Ambient Pressure and Temperature for Energy Storage. *Nano Letters* **2012**, 12, 4617-4623.

136. Ma, L.; Lee, S.; DeMuth, J.; Maldonado, S. Direct electrochemical deposition of crystalline silicon nanowires at T≥60 °C. *RSC Advances* **2016**, 6, 78818-78825.

137. Gaskell, D. R.; Laughlin, D. E.; Morris, A. E. Introduction to the Thermodynamics of Materials, Fifth Edition. Taylor Francis: **2003**.

138. Townsend, H. E. Potential-pH diagrams at elevated temperature for the system Fe-H_2O. *Corrosion Science* **1970**, 10, 343-358.

139. Pourbaix, M. Atlas of electrochemical equilibria in aqueous solutions. National Association of Corrosion Engineers: **1974**.

140. Olesinki, R. W.; Kanani, N.; Abbaschian, G. J. The Ge-In (Germanium-Indium) system. *Bulletin of Alloy Phase Diagrams* **1985**, 6, 536-539.

141. Sutter, E. A.; Sutter, P. W. Size-Dependent Phase Diagram of Nanoscale Alloy Drops Used in Vapor-Liquid-Solid Growth of Semiconductor Nanowires. *ACS Nano* **2010**, 4, 4943-4947.

142. Adhikari, H.; Marshall, A. F.; Goldthorpe, I. A.; Chidsey, C. E. D.; McIntyre, P. C. Metastability of Au-Ge Liquid Nanocatalysts: Ge Vapor-Liquid-Solid Nanowire Growth Far below the Bulk Eutectic Temperature. *ACS Nano* **2007**, 1, 415-422.

143. Schwalbach, E. J.; Voorhees, P. W. Phase Equilibrium and Nucleation in VLS-Grown Nanowires. *Nano Letters* **2008**, 8, 3739-3745.

144. Kodambaka, S.; Tersoff, J.; Reuter, M. C.; Ross, F. M. Germanium Nanowire Growth Below the Eutectic Temperature. *Science* **2007**, 316, 729-732.

145. Yang, P.; Yan, H.; Mao, S.; Russo, R.; Johnson, J.; Saykally, R.; Morris, N.; Pham, J.; He, R.; Choi, H. J. Controlled Growth of ZnO Nanowires and Their Optical Properties. *Advanced Functional Materials* **2002**, 12, 323-331.

146. Govender, K.; Boyle, D. S.; O'Brien, P.; Binks, D.; West, D.; Coleman, D. Room-Temperature Lasing Observed from ZnO Nanocolumns Grown by Aqueous Solution Deposition. *Advanced Materials* **2002**, 14, 1221-1224.

147. Park, W. I.; Yi, G. -C. Electroluminescence in n-ZnO Nanorod Arrays Vertically Grown on p-GaN. *Advanced Materials* **2004**, 16, 87-90.

148. Hassan, J. J.; Mahdi, M. A.; Ramizy, A.; Abu Hassan, H.; Hassan, Z. Fabrication and characterization of ZnO nanorods/p-6H-SiC heterojunction LED by microwave-assisted chemical bath deposition. *Superlattices and Microstructures* **2013**, 53, 31-38.

149. An, S. J.; Yi, G.-C. Near ultraviolet light emitting diode composed of n-GaN/ZnO coaxial nanorod heterostructures on a p-GaN layer. *Applied Physics Letters* **2007**, 91, 123109.

150. Anta, J. A.; Guillen, E.; Tena-Zaera, R. ZnO-Based Dye-Sensitized Solar Cells. *The Journal of Physical Chemistry C* **2012**, 116, 11413-11425.

151. Sarkar, S.; Makhal, A.; Bora, T.; Lakhsman, K.; Singha, A.; Dutta, J.; Pal, S. K. Hematoporphyrin-ZnO Nanohybrids: Twin Applications in Efficient Visible-Light Photocatalysis and Dye-Sensitized Solar Cells. *ACS Applied Materials & Interfaces* **2012**, 4, 7027-7035.

152. Ajuria, J.; Etxebarria, I.; Azaceta, E.; Tena-Zaera, R.; Fernandez-Montcada, N.; Palomares, E.; Pacios, R. Novel ZnO nanostructured electrodes for higher power conversion efficiencies in polymeric solar cells. *Physical Chemistry Chemical Physics* **2011**, 13, 20871-20876.

153. Tena-Zaera, R.; Elias, J.; Levy-Clement, C. ZnO nanowire arrays: Optical scattering and sensitization to solar light. *Applied Physics Letters* **2008**, 93, 233119.

154. Liu, Y.; Li, Y.; Zeng, H. ZnO-Based Transparent Conductive Thin Films: Doping, Performance, and Processing. *Journal of Nanomaterials* **2013**, 2013, 9.

155. Guo, W.; Liu, T.; Huang, L.; Zhang, H.; Zhou, Q.; Zeng, W. HMT assisted hydrothermal synthesis of various ZnO nanostructures: Structure, growth and gas sensor properties. *Physica E: Low-dimensional Systems and Nanostructures* **2011**, 44, 680-685.

156. Kashif, M.; Ali, M. E.; Ali, S. M. U.; Hashim, U. Sol-gel synthesis of Pd doped ZnO nanorods for room temperature hydrogen sensing applications. *Ceramics International* **2013**, 39, 6461-6466.

157. Arya, S. K.; Saha, S.; Ramirez-Vick, J. E.; Gupta, V.; Bhansali, S.; Singh, S. P. Recent advances in ZnO nanostructures and thin films for biosensor applications: Review. *Analytica Chimica Acta* **2012**, 737, 1-21.

158. Ni, Y.; Zhu, J.; Zhang, L.; Hong, J. Hierarchical ZnO micro/nanoarchitectures: hydrothermal preparation, characterization and application in the detection of hydrazine. *CrystEngComm* **2010**, 12, 2213-2218.

159. Zhang, Y.; Mu, J. One-pot synthesis, photoluminescence, and photocatalysis of Ag/ZnO composites. *Journal of Colloid and Interface Science* **2007**, 309, 478-484.

160. Li, X.; Wang, J.; Yang, J.; Lang, J.; Cao, J.; Liu, F.; Fan, H.; Gao, M.; Jiang, Y. Size-controlled fabrication of ZnO micro/nanorod arrays and their photocatalytic performance. *Materials Chemistry and Physics* **2013**, 141, 929-935.

161. Izaki, M.; Omi, T. Transparent zinc oxide films prepared by electrochemical reaction. *Applied Physics Letters* **1996**, 68, 2439-2440.

162. Sophie, P.; Daniel, L. Cathodic electrodeposition from aqueous solution of dense or open-structured zinc oxide films. *Advanced Materials* **1996**, 8, 166-170.

163. Gao, X.-D.; Peng, F.; Li, X.-M.; Yu, W.-D.; Qiu, J.-J. Growth of highly oriented ZnO films by the two-step electrodeposition technique. *Journal of Materials Science* **2007**, 42, 9638-9644.

164. Pauporte, T.; Lincot, D.; Viana, B.; Pelle, F. Toward laser emission of epitaxial nanorod arrays of ZnO grown by electrodeposition. *Applied Physics Letters* **2006**, 89, 233112.

165. Znaidi, L. Sol-gel-deposited ZnO thin films: A review. *Materials Science and Engineering: B* **2010**, 174, 18-30.

166. Kamaruddin, S. A.; Chan, K.-Y.; Yow, H.-K.; Zainizan Sahdan, M.; Saim, H.; Knipp, D. Zinc oxide films prepared by sol-gel spin coating technique. *Applied Physics A* **2011**, 104, 263-268.

167. Liao, Y.; Zhou, X.; Xie, X.; Yu, Q. The effects of solvents on the highly oriented ZnO films prepared using sol-gel method. *Journal of Materials Science: Materials in Electronics* **2013**, 24, 4427-4432.

168. Ng, Z.-N.; Chan, K.-Y.; Tohsophon, T. Effects of annealing temperature on ZnO and AZO films prepared by sol-gel technique. *Applied Surface Science* **2012**, 258, 9604-9609.

169. Govender, K.; Boyle, D. S.; Kenway, P. B.; O'Brien, P. Understanding the factors that govern the deposition and morphology of thin films of ZnO from aqueous solution. *Journal of Materials Chemistry* **2004**, 14, 2575-2591.

170. Jaejin, S.; Seonghoon, B.; Jonghyuck, L.; Sangwoo, L. Role of OH^- in the low temperature hydrothermal synthesis of ZnO nanorods. *Journal of Chemical Technology Biotechnology* **2008**, 83, 345-350.

171. Smith, F. T. J. Metalorganic chemical vapor deposition of oriented ZnO films over large areas. *Applied Physics Letters* **1983**, 43, 1108-1110.

172. Montenegro, D. N.; Souissi, A.; Martinez-Tomas, C.; Munoz-Sanjose, V.; Sallet, V. Morphology transitions in ZnO nanorods grown by MOCVD. *Journal of Crystal Growth* **2012**, 359, 122-128.

173. Kim, A. Y.; Jang, S.; Lee, D. H.; Yim, S. y.; Byun, D. Effects of temperature on ZnO hybrids grown by metal-organic chemical vapor deposition. *Materials Research Bulletin* **2012**, 47, 2888-2890.

174. Kang, D.; Lee, D.; Choi, K.-S. Electrochemical Synthesis of Highly Oriented, Transparent, and Pinhole-Free ZnO and Al-Doped ZnO Films and Their Use in Heterojunction Solar Cells. *Langmuir* **2016**, 32, 10459-10466.

175. O'Regan, B.; Sklover, V.; Gratzel, M. Electrochemical Deposition of Smooth and Homogeneously Mesoporous ZnO Films from Propylene Carbonate Electrolytes. *Journal of The Electrochemical Society* **2001**, 148, C498-C505.

176. Canava, B.; Lincot, D. Nucleation effects on structural and optical properties of electrodeposited zinc oxide on tin oxide. *Journal of Applied Electrochemistry* **2000**, 30, 711-716.

177. Izaki, M.; Omi, T. Electrolyte Optimization for Cathodic Growth of Zinc Oxide Films. *Journal of The Electrochemical Society* **1996**, 143, L53-L55.

178. Yoshida, T.; Komatsu, D.; Shimokawa, N.; Minoura, H. Mechanism of cathodic electrodeposition of zinc oxide thin films from aqueous zinc nitrate baths. *Thin Solid Films* **2004**, 451-452, 166-169.

179. Bard, A. J.; Faulkner, L. R. Electrochemical Methods: Fundamentals and Applications. *Wiley:* **2000**.

180. Cao, W.; Zheng, Y.; Li, Z.; Wrzesniewski, E.; Hammond, W. T.; Xue, J. Flexible organic solar cells using an oxide/metal/oxide trilayer as transparent electrode. *Organic Electronics* **2012**, 13, 2221-2228.

VITA

Naveen Kumar Mahenderkar was born and raised in Hyderabad, Telangana, India. He finished high school with emphasis in chemistry. He then went to college at Mahatma Gandhi Institute of Technology, affiliated to Jawaharlal Nehru Technological University in Hyderabad. He obtained his bachelor of technology degree in Metallurgical and Materials Engineering in 2012. During his undergraduate studies, he obtained industrial and R&D training as an intern at national labs for various metallurgical processes such as steel making, super alloys and carbon nanotube polymer composites. He also conducted research on ultra-high cycle fatigue properties of austenitic stainless steels under Prof. Hans-Jürgen Christ at the University of Siegen in Siegen, Germany. His undergraduate thesis was to study the fracture toughness of carbon nanotube and carbon fiber reinforced polymer matrix composites for aerospace applications under the guidance of Dr. N. Eswara Prasad at Regional Center for Military Airworthiness (Materials), Hyderabad. In 2012, he was accepted in the Materials Science and Engineering department at Missouri University of Science Technology in Rolla, Missouri. He joined Prof. Jay A. Switzer's lab as a PhD student in August of 2012 working on electrodeposition of semiconductor nanostructures and epitaxial thin films for flexible electronics. During his PhD, he did a summer internship at TE Connectivity in 2015 working on the R&D of silver-palladium alloys for industrial electroplating of automotive connectors. He was awarded graduate student gold award for his work on single-crystal substrates for flexible electronics at the 2017 Fall MRS Meeting in Boston, Massachusetts. His work on flexible single-crystal Au foil was published in *Science* journal and was also highlighted on the U.S. Department of Energy website and the MRS bulletin. He received his PhD in Materials Science and Engineering from Missouri University of Science and Technology in July, 2018.